Photoinduced Dichroism in Amorphous As_2Se_3 Thin Film

A Thesis Submitted to the

College of Graduate Studies and Research

in Partial Fulfillment of the Requirements for the

Degree of Master of Science

in the Department of Electrical Engineering

University of Saskatchewan

Saskatoon

By

Daniel DeForrest

PERMISSION TO USE

In presenting this thesis in partial fulfillment of the requirements for a Postgraduate degree from the University of Saskatchewan. The author has agreed that the Library of the University of Saskatchewan, may make this thesis freely available for inspection. Moreover, the author has agreed that permission for copying of this thesis in any manner, in whole or in part, for scholarly purposes may be granted by the professors who supervised the thesis work recorded herein, or in their absence, by the Head of the Department or the Dean of the College of Engineering in which this thesis work was done. It is understood that due recognition will be given to the author of this thesis and to the University of Saskatchewan in any use of the material in this thesis. Copying or publication or any other use of this thesis or parts thereof for financial gain without approval by the University of Saskatchewan and the author's written permission is prohibited.

Requests for permission to copy or make any other use of the material in this thesis is whole or in part should be addressed to:

Head of the Department of Electrical Engineering
57 Campus Drive
University of Saskatchewan
Saskatoon, Canada S7N 5A9

ABSTRACT

The dichroism in amorphous As_2Se_3 induced by a polarized beam of near band-gap light ($\lambda = 632.8$ nm) was measured in films that ranged in thickness from 0.25 μm to 1.93 μm. Most noncrystalline materials are initially isotropic and homogeneous. When amorphous As_2Se_3 (a chalcogenide glass) absorbs an intense pump-beam of polarized light, the absorption coefficient for light polarized in the same direction as the pump-beam is less than for the perpendicular polarization, i.e. the sample becomes anisotropic (dichroic). The induced dichroism is reversible by rotating the polarization of the pump light by 90°. Induced dichroism is potentially useful in various photonic devices including optical switches, optical memory, and photowritable polarizers.

Several aspects of photoinduced anisotropy in a-As_2Se_3 have been analyzed: (i) rate of photoinduced anisotropy buildup as a function of inducing beam intensity and sample thickness, (ii) the kinetics of the photoinduced anisotropy buildup in terms of a stretched exponential curve, (iii) the stretched exponent, β, as a function of inducing beam intensity and sample thickness, (iv) reversibility of the photoinduced anisotropy, (v) saturation level of photoinduced anisotropy as a function of inducing beam intensity and sample thickness.

The anisotropy buildup kinetics has been found to follow a stretched exponential behavior and that there exists an inverse relationship between the pump intensity and the time constant, τ. The $\tau(I)$ vs intensity (I) relationship more closely follows a logistic dose response curve than a simple straight line or power law relationship. There exists a direct relationship between the time contact τ and the sample thickness, where a longer anisotropy buildup time is required as the sample thickness increases. The stretched exponent, β, was found to be approximately 0.6 and has a slight dependence on the inducing light intensity. The correlation of the stretching exponent, β, to sample thickness, L, was found to have a weak inverse relationship, that is β tends to decrease as the sample thickness increases.

The findings in this work demonstrate that the anisotropy orientation could be changed indefinitely since it was found that even after 100 orientation changes the

anisotropy saturation had no measurable fatiguing. The anisotropy saturation level was found to be independent of the inducing beam intensity and linearly proportional to the sample thickness.

I hear and I forget. I see and I remember. I do and I understand!

Source Unknown

ACKNOWLEDGEMENTS

I would first like to thank my wife Marianne and my two children Katia and Dailen. Their support (and patience while I monopolized the home computer) was very much appreciated. Kiril Koughia deserves a big "thank you" for the stimulating and very helpful conversations regarding my many, many questions. A big thank you also goes out to Angie Ortlepp of the Physics Department for the use of several pieces of equipment. If it was not for her generosity this project would not have been possible. To Matthew Kowalyshen I extend my gratitude for the help with measuring and analysis of data for the thickness dependent results. This helped immensely for determining effects and trends. I would like to thank Dr. Kunio Takaya for giving me the opportunity to earn a little extra money during this study by allowing me to teach at the undergraduate level. The experience will always be greatly appreciated. For the financial support during this endeavor I would like to express my deep gratitude to my Supervisor Dr. Safa Kasap, NSERC, the University of Saskatchewan and TRLabs. Finally, and certainly not least, I would like to thank my Supervisor Dr. Safa Kasap and Co-Supervisor Dr. Robert Johanson for their guidance, patience and encouragement throughout the course of this work.

Table of Contents

List of Figures

List of Tables

Glossary of Symbols

a ..... Interatomic separation

α ..... Absorption coefficient

$\alpha_{\perp,//}$ ..... Absorption (perpendicular or parallel)

A_{sat} ..... Anisotropy saturation

β ..... Stretched exponent

c ..... Speed of light $\approx 2.9979 \times 10^{8}$ m s^{-1}

δ ..... Penetration depth

ΔE ..... Activation energy

E ..... Energy

$E(a)$ ..... Potential energy

E_0 ..... Minimum potential energy

E_A ..... Attractive energy

E_c ..... Conduction band edge

E_F ..... Fermi energy

E_g ..... Bandgap

E_o ..... Optical gap

E_{ph} ..... Photon energy ($E_{ph} = h\nu$)

E_R ..... Repulsive energy

E_v ..... Valence band edge

e ..... Electric charge

Γ ..... Linear dichroism

H ..... Enthalpy

h ..... Planck's constant $\approx 6.626 \times 10^{-34}$ J s

I ..... Intensity

I_{Ph} ..... Photonic current

k_B ..... Boltzmann constant $\approx 1.3807 \times 10^{23}$ J K^{-1}

L ..... Length

n ..... Carrier density

N ..... Anisotropic microvolumes

P_{op} ..... Optical power

r ..... Correlation coefficient

R ..... Reflectance

$r_{\perp,//}$ ..... Reflection coefficient (perpendicular or parallel)

R ..... Responsivity

S ..... State of disorder

σ_{DC} ..... D.C. conductivity

λ ..... Wavelength

τ ..... Time constant

$t_{\perp,//}$ ..... Transmission coefficient (perpendicular or parallel)

T ..... Transmittance

T ..... Temperature

T_g ..... Glass transition temperature

T_m ..... Melting temperature

U ..... Hubbard correlation energy

U_{eff} ..... Effective Hubbard energy

μ ..... Drift mobility (average velocity per unit electric field)

v ..... Frequency i.e. $v = \frac{\lambda}{c}$

ψ ..... Bonding

ψ^* ..... Antibonding

Glossary of Abbreviations

As_2Se_3..... Arsenic triselenide

As_2S_3 ..... Arsenic trisulfide

a-Se..... Amorphous Selenium

CB ..... Conduction Band

CFO..... Cohen, Fritzsche and Ovshinski

DB ..... Dangling Bond

DOS..... Density of States

ESR ..... Electron Spin Resonance

EXAFS .... Extended X-ray Absorption Fine Structure

FWHM .... Full Width Half Maximum

HeNe ..... Helium Neon Laser

IRO..... Intermediate-Range Order (also called MRO)

IVAP ..... Intimate Valence Alternation Pair

LED..... Light Emitting Diode

LIA ..... Lock-In Amplifier

LP ..... Lone Pair

LPF..... Low Pass Filter

LRO..... Long Range Order

MRO..... Medium-Range Order (also called IRO)

PA..... Photoinduced Anisotropy

PB..... Photobleaching

PBi..... Photoinduced Birefringence

PD..... Photodarkening

PDi ..... Photoinduced Dichroism

RPM ..... Rotations per Minute

SRO..... Short-Range Order

VAP..... Valence Alternation Pair

VB ..... Valence Band

Chapter 1

Introduction

1.1 Background

Prior to the 1950's it was believed that amorphous materials could not be semiconductors. This changed in 1955, when Nina A. Goryunova and Boris T. Kolomiets at A. F. Ioffe Physico-Technical Institute in Leningrad (now St. Petersburg) found that one of their amorphous compositions exhibited the typical semiconductor behavior of conductivity [1]. Since that time amorphous materials have been studied extensively for a wide range of applications. Among the various amorphous materials studied, it is the chalcogenide glasses that display certain properties which makes them unique. An entire xerographic industry came to be built on the photoconductive properties of selenium [2]. As well, amorphous selenium has been used as the material of choice for an x-ray photoconductor. This has made the realization of a digital flat panel x-ray image detector possible when combined with an active matrix array [3].

More recently the optical properties of chalcogenide glasses have seen a large amount of research devoted to them. There are several reasons for this. Among them are the increasing demands of higher data transmission rates on telecommunication networks, mainly due to increased internet use. Because the large bandwidth offered by optical fibers far exceeds any other available medium it has long been the choice to handle the global information network. Ideally, the whole system should be photonic but there are still many hurdles to overcome in order to make a totally photonic system a reality. Firstly optoelectronic and photonic devices that can handle the large potential bandwidth need to be developed. Secondly these devices need to be cost effective so that they are accessible to the masses. Therefore cheap materials and low cost fabrication are important. Couple this with higher levels of integration and the

realization of optical chips is possible. The attainment of chip scale optoelectronic and photonic devices is a sector that has seen heavy research as of late. The field of integrated optics, sometimes referred to as microphotonics [4], is targeted towards the integration of photonic devices with CMOS electronics. Typically silicon-on-insulator (SOI) wafers are being used [5]. Research in this area has also been motivated by the computing industry for obvious reasons. Several characteristics make chalcogenide glasses ideal for these integrated devices.

- Typically chalcogenide glasses have lower glass transition and melting temperatures. Thus, glass fabrication is relatively inexpensive with various methods available: vacuum vapor deposition, sputtering and pulsed laser deposition just to mention a few. These are distinct advantages in the fabrication of optical devices.

- Chalcogenide glasses have weak bond strengths and high atomic masses, which results in low phonon energies ($\approx 300\ cm^{-1}$) [6]. This results in a glass that is highly transparent in the mid to far infrared spectrum. Having the transparency window for selenide glasses ranging from 0.8 to 15 μm [5], makes these glasses extremely desirable for optical transmission systems.

- As well, the weak bonding arrangement along with a long Urbach absorption tail [7] leads to some unique photosensitivity changes. A chalcogenide glass sample that is exposed to near bandgap or sub-bandgap laser light results in various photoinduced phenomena to occur, both reversible and irreversible. These changes include optical, chemical, physical and structural properties of the sample [8].

- Chalcogenide glasses also have high refractive indices, in the range of 2-3 which, lead to good light confinement in waveguides made from these glasses [5]. This is a key requirement of glass based microphotonics slab waveguides and optical fibers.

- One of the photoinduced phenomena results in a large change to the refractive index, which is referred to as photodarkening or photobleaching. This is useful in the designing of waveguides [9] and gratings [10]. Furthermore, this also appears to change the material etch characteristics making them useful as inorganic photoresists [11].

- Another unique optical effect of chalcogenide glass is the reversible photoinduced anisotropy (dichroism) [12]. When a chalcogenide sample is irradiated with a strong polarized light source, the absorption coefficient for light polarized in the same direction as the inducing beam is less than for the perpendicular polarization. Induced dichroism is potentially useful in various photonic devices [13] including optical switches, optical memories, polarization plates with optically changeable polarization angles and beam splitters where the amount of deviation between the light rays can be varied.

- Coupled with their weak bonding arrangement, high refractive index and low transmission loss for mid and far infrared wavelengths. Chalcogenide glasses also provide both large stimulated emission cross sections and low non-radiative transition rates, which make them attractive as host materials for rare-earth elements. This offers the potential of a highly efficient optical gain device with broadband optical pumping, possibly by way of LED's.

- Chalcogenide glasses are also one of the most promising non-linear optical media [14]. These glasses have shown higher non-linear indices than oxide glasses and almost two orders of magnitude larger than silica glass with similar response time [15]. Applications of this property include all-optical switching.

- Chalcogenide glasses can be photodoped with metals (typically silver). A metal film is first deposited on the chalcogenide glass and then irradiated with bandgap light. The result is diffusion of the metal into the

chalcogenide glass. Interestingly if linearly polarized light is used for the dissolution then the sample will develop a strong dichroism with an orientation opposite that of silver free chalcogenide glass [16].

Further unique properties of these materials for applications outside of optical fiber communications or microphotonics include;

- Reversible amorphous to crystalline phase change. By controlling the thermal cycling of tellurium based chalcogenide materials through laser absorption and/or current flow the chalcogenide alloy can be changed between an amorphous state to a crystalline or vise versa [16]. This is the basic component that has made the rewritable CD/DVD possible.

- Along with the photoinduced optical anisotropy, certain chalcogenide alloys have also demonstrated photoconductivity that is dependent on the anisotropic state [17]. To this end, the amount of current flow in a nanoampermeter connected to the sample could be controlled by the polarization direction of the inducing laser.

- Another unique characteristic of some chalcogenide alloys is a reversible optomechanical effect. This effect is related to the reversible photoinduced anisotropy in that the nanocontration and dilatation of a chalcogenide film is induced with polarized light [18]. To date the only materials that have the accuracy of nanometer scale precision are piezoelectric and electrostrictive positioning devices both of which use electric fields for positioning. Chalcogenide could offer a nanometer scale positioning device that can operate in electrostatic sensitive areas.

However, providing components in optically integrated form has proven to be very challenging [19]. Some of the key problematic issues involving chalcogenide alloys are;

- Incompatible thermal characteristics with some substrates [9, 20].

- Lack of chemical and mechanical durability [9].
- Rate and degree of change between modes [13]. i.e. the amount of dichroic change between two orthogonal states is very low since a 5% change is regarded as giant anisotropy [21].
- Toxicity of some elements (Sulfur and Tellurium in particular).

Despite these drawbacks the numerous unique characteristics of chalcogenide alloys make them very promising materials for optoelectronic and photonic devices.

Photoinduced anisotropy is perhaps the most fascinating of all the photoinduced phenomena, both from an application as well as a scientific viewpoint. Ever since the discovery by Zhandov et al. [12] over 25 years ago that the polarization direction of a strong inducing light beam incident on an initially isotropic chalcogenide sample changed it to anisotropic there has been a great deal of research devoted to this phenomena. In that time there has been plenty of speculation about the underlying microscopic mechanisms involved in this macroscopic property. Viewpoints are wide and varied as there is still no common agreement on how the macroscopic anisotropy is related to the microscopic changes. This is largely due to the fact that the microscopic mechanisms cannot be directly controlled by an experiment. Test setups measure the intensity of orthogonal polarizations and as a result only record the macroscopic anisotropy buildup as a function of time.

1.2 Research Motivation and Objectives

The main drive or purpose of this research study is to find materials which provide higher performance optical and optoelectronic devices with greater levels of integration (optical IC's). This would greatly benefit optical networks and pave the way to an optical computer. Much the same way as the monolithic integration of transistors has made the desktop computer a reality.

Amorphous chalcogenide alloys have many unique properties that make them attractive for use as photonic devices. The high refractive indices (typically n = 2 to 3)

lead to good light confinement making them excellent candidates for slab waveguides and optical fibers. Photoinduced effects generate many distinctive optical and structural changes. For example, intense light can cause an expansion in volume or change the index of refraction. This is known as photodarkening or photobleaching a scalar effect and is useful in the designing of waveguides and gratings. This also changes the material etch characteristics making them useful as inorganic photoresists. When the inducing light source is polarized it can produce the anisotropic effects of dichroism and birefringence. These are vectoral effects in that they can only be induced by polarized light. This distinctive property is potentially useful in various photonic devices. Such as optical switches, optical memories, polarization plates with optically changeable polarization angles and beam splitters where the amount of deviation between the light rays can be optically varied. These changes persist and are stable under exposure to weaker light.

The research in this thesis deals with the photoinduced anisotropy of As_2Se_3 as induced by a linearly polarized Helium Neon laser light source. Several aspects of this vectoral phenomenon are observed:

1. Fitting the photoinduced anisotropy buildup to a stretched exponential curve
2. Reversibility of the photoinduced anisotropy
3. Rate of photoinduced anisotropy buildup as a function of inducing beam intensity and sample thickness
4. The stretched exponent, β, as a function of inducing beam intensity and sample thickness
5. Saturation level of photoinduced anisotropy as a function of inducing beam intensity and sample thickness

1.3 Thesis Layout

In this thesis the second chapter delivers a basic introduction to amorphous semiconductors and chalcogenide glasses. The chapter starts out by first explaining the structure of amorphous materials and how they differ from their crystalline counterparts. This is followed by a brief explanation of some common optical and electrical properties. The chapter is ended with a discussion on valence alternate pairs VAPs and intimate valence alternate pairs IVAPs.

In Chapter 3 an overview of the photoinduced effects in chalcogenide glasses is presented. The differences between vectoral and scalar, as well as reversible and irreversible effects, is explained. This is followed by a discussion on photoinduced anisotropy namely photoinduced dichroism and refractive index change. The final section in this chapter describes some existing models used to explain the photoinduced anisotropy phenomena.

Chapter 4 presents the methods used for preparing the thin films and substrates. The experimental apparatus is described as a whole and then divided up into its minor components and explained in detail.

Experimental aspects is the subject of Chapter 5. This is where it is revealed how the photoinduced anisotropy can be derived from measured quantities. The experimental procedures followed for measuring the photoinduced anisotropy and photodarkening are explained. The mathematics of the experimental setup are also presented along with the solution for determining the amount of anisotropy from my measured results.

Chapter 6 starts out by describing how the data was analyzed. This is followed by the presentation of the experimental data for the measurements of photoinduced linear dichroism as a function of time and sample thickness, along with a discussion of the results.

This thesis is ended with Chapter 7 where some general conclusions of this work are presented. Then a few recommendations for future work are given.

Chapter 2

Amorphous Semiconductors

2.1 Introduction

This chapter introduces what amorphous semiconductors are and how they differ from their crystalline counterparts. The structural properties, glass transition temperature, state of disorder, electrical and optical properties of semiconductors are presented first. This is followed by the chalcogenide section, where a discussion on valence alternate pairs (VAPs) and intimate valence alternate pairs (IVAPs) ends the chapter.

2.2 Amorphous Semiconductors

The word amorphous is derived from the Greek language, α = not and μορφως = shape, meaning without definite shape or unclassifiable [22]. Amorphous semiconductors have become important because of their significance in various applications. For hydrogenated amorphous silicon, (a-Si:H) there are solar cells, thin film transistors, image scanners, electrophotography, optical recording and gas sensors. Whereas applications for amorphous chalcogenide materials include electrophotography, photolithography, Bragg gratings, optical waveguides, x-ray imaging, all optical switching and optical memories (CD-RW and DVD-RW) [16, 22, 23] just to name a few.

2.2.1 Structural Properties

When conditions of temperature and pressure are given, materials take on one of three states, gas, liquid, or solid. In thermal equilibrium, 'solid' means the crystalline state, while liquids and gases can be described as thermodynamically stable or

metastable forms. For a solid in the crystalline state the characteristic structure has a well defined symmetry or periodicity in which the exact orientation and number of neighbors can be determined from one atom to the next as the simplistic two-dimensional representation of a crystal shows in Figure 2-1 (a). This is known as long-range order, LRO.

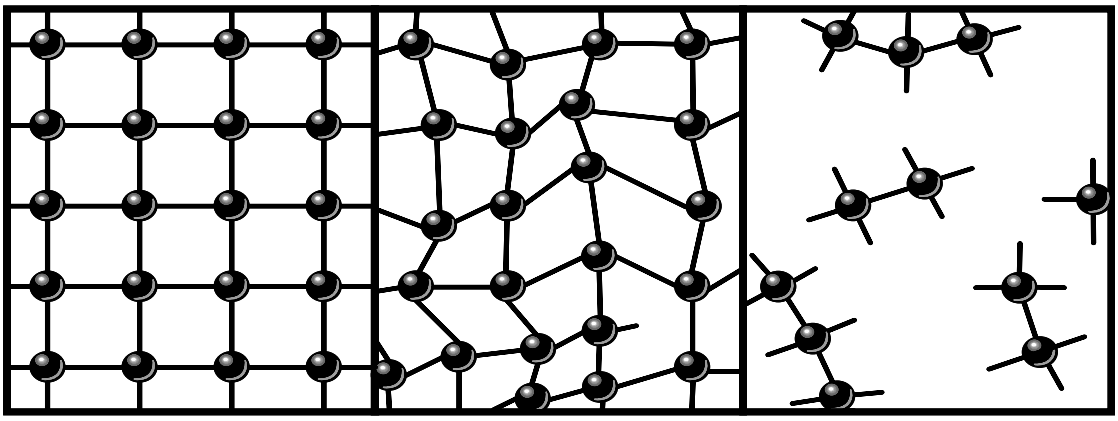

Figure 2-1: Simple two-dimensional illustration of three material states.

In the liquid state the atoms have sufficient energy to frequently bend, twist, make and break bonds, causing a disordered bond geometry that is not periodic as shown in Figure 2-1 (c). For a glass or amorphous structure the organization of each atom is well defined because each atom must fulfill its chemical bonding requirements, but the entire arrangement lacks long-range order. Consequently, an amorphous material does not have the periodicity of the crystalline counterpart but is made up of a continuous random network, CRN, of atoms as depicted in Figure 2-1 (b). This does not mean that an amorphous structure is completely random. For short range order, SRO, where distances range from 2 to 5 Å, there is very little difference between the crystalline and amorphous semiconductors.

Amorphous semiconductors, like crystalline solids, can be classified into several categories depending on their characteristic properties. By first considering, the type of

chemical bonding involved for the cohesive energy of the material. The amorphous solid can be divided into five major classes: (1) ionic, (2) covalent, (3) metallic, (4) Van der Waals, and (5) hydrogen-bonding. The elements of interest here namely the pnictide, group V, Arsenic (As), and the chalcogenide, group VI, Selenium (Se) fall under category 2, covalently bonded glasses. The pnictide and chalcogenide groups follow the octet theory, [22] also known as the '8-N' rule of Mott [24], where the number of bonds per atom (coordination number), N_{Bond} is

$$N_{Bond} = 8 - \text{group number} \qquad \text{Coordination number (2.1)}$$

This results in a coordination number of 3 for pnictide and 2 for chalcogenide. From this we expect positional disorder, Figure 2-2 (a), and for multi-component glasses such as As_2Se_3, will have compositional disorder as well, Figure 2-2 (b).

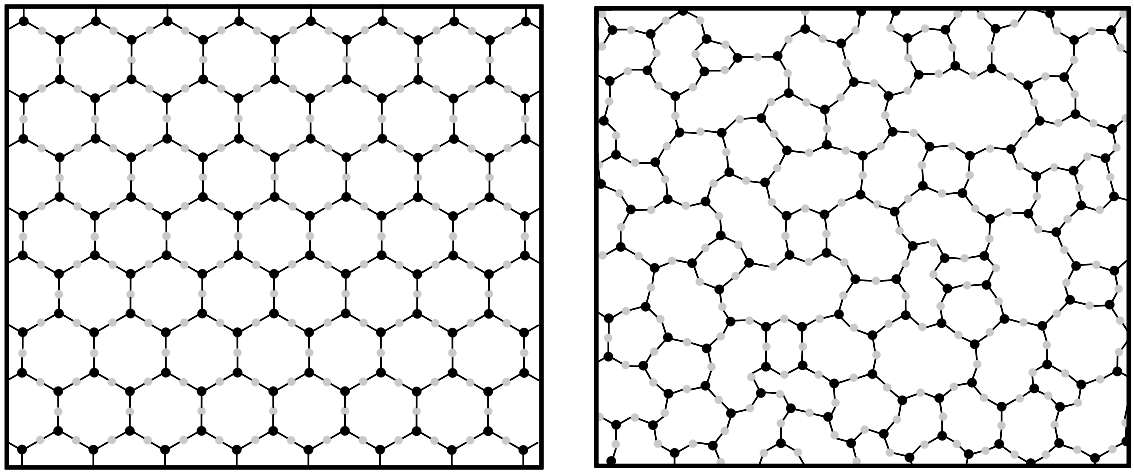

(a) (b)

Figure 2-2: Two-dimensional diagrams of the bonding arrangement for an A_2Se_3 in crystalline form (a) and amorphous or glass form (b).

Whenever two atoms are brought together a bond will form provided the overall energy of the combined atoms is lower than the single atom. This is shown by the potential energy diagram in Figure 2-3. Here the potential energy of the atoms (E_a) is shown as a function of the interatomic spacing (a). There are two separate energies acting on these atoms an attractive energy (E_A) and a repulsive energy (E_R) to produce

the net energy (E). As the two atoms are brought together from infinity, the lowering energy corresponds to the attractive interaction of the electrons to the protons. When the atoms get too close the repulsive energy arising from the electron – electron and the proton – proton repulsions dominate causing an increase in the potential energy. The minimum potential energy (E_0) corresponds to the equilibrium state of the attractive and repulsive energies and is referred to as the *bond energy*. The interatomic separation (a_0) at this equilibrium state is nominally referred to as the *bond length*. In solids held together by covalent bonds the outer electrons of the two adjacent atoms become spread out over both of them.

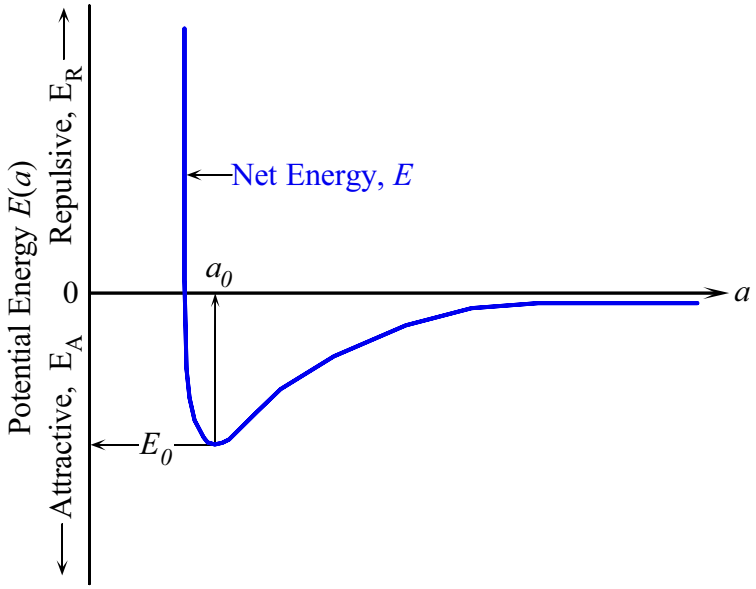

Figure 2-3: Potential energy, $E(a)$, versus interatomic spacing, a.

A major result of the quantum theory is that only a discrete number of states is possible for the electrons in any given atom. These states are grouped into shells where the energy of the electrons lie within a small range of values. Electrons in the outermost shell, known as the *valence electrons*, are responsible for bonding between atoms. For the elements discussed here there are exactly eight possible electron states. Two are located in a lower energy s state and six in a higher energy or p state. The electrons in the s state have only one possible value of orbital angular momentum whereas the p

states have three. As well all electrons can only have one of two possible spin values, spin up or spin down. One of the most important theorems in quantum physics is the *Pauli exclusion principle*, which prevents any two electrons in the same atom from occupying the same state. The number of electrons that a given atom possesses determines the element, but it is the Pauli exclusion principle which accounts for the diverse chemical properties of the elements.

As previously stated two atoms will combine and form a bond, provided the total energy of the bonded atoms is lower than the separate atoms. Whenever any two atoms are close enough for their outer electrons to interact a shift in their energy states will result. This results in a reduction in energy of some states, known as *bonding* states (ψ), and an equal number of states to increase in energy, called *antibonding* states (ψ^*). Bonding states are always filled by pairs of electrons with opposite spins and the antibonding states are empty. When the bonding states are filled the solid is referred to as being maximally bound.

A chalcogen element has six electrons in the outermost shell, s^2p^4, which is schematically shown in Figure 2-4 (a). The two paired s-electrons are located closer to the atom and therefore have a deep-energy state, which subsequently do not form any bonds. Two of the p-electrons form covalent bonds (coordination number is 2) and the remaining two paired p-electrons are known as a *lone pair*. Referring to Figure 2-4 (b) we see that the lone pair electrons are at a higher energy level than that of the covalent electrons. Also indicated on this figure are the bonding, ψ and antibonding, ψ^* states.

So far the interaction of only two atoms has been looked at, but a solid consists of at least 10^{24} atoms. This results in an enormous number of states in a small energy range and consequently can be treated as a continuous distribution in energy over a given range. This application of the quantum mechanical theory to solids leads to the band theory. Where the electron energy states related with the individual atoms combine in such a way to form almost continuous regions of energies in which states exists, *bands*, and are sometimes separated by regions where no states are possible, *gaps*. The highest band of filled energy states is referred to as the *valence band* (VB)

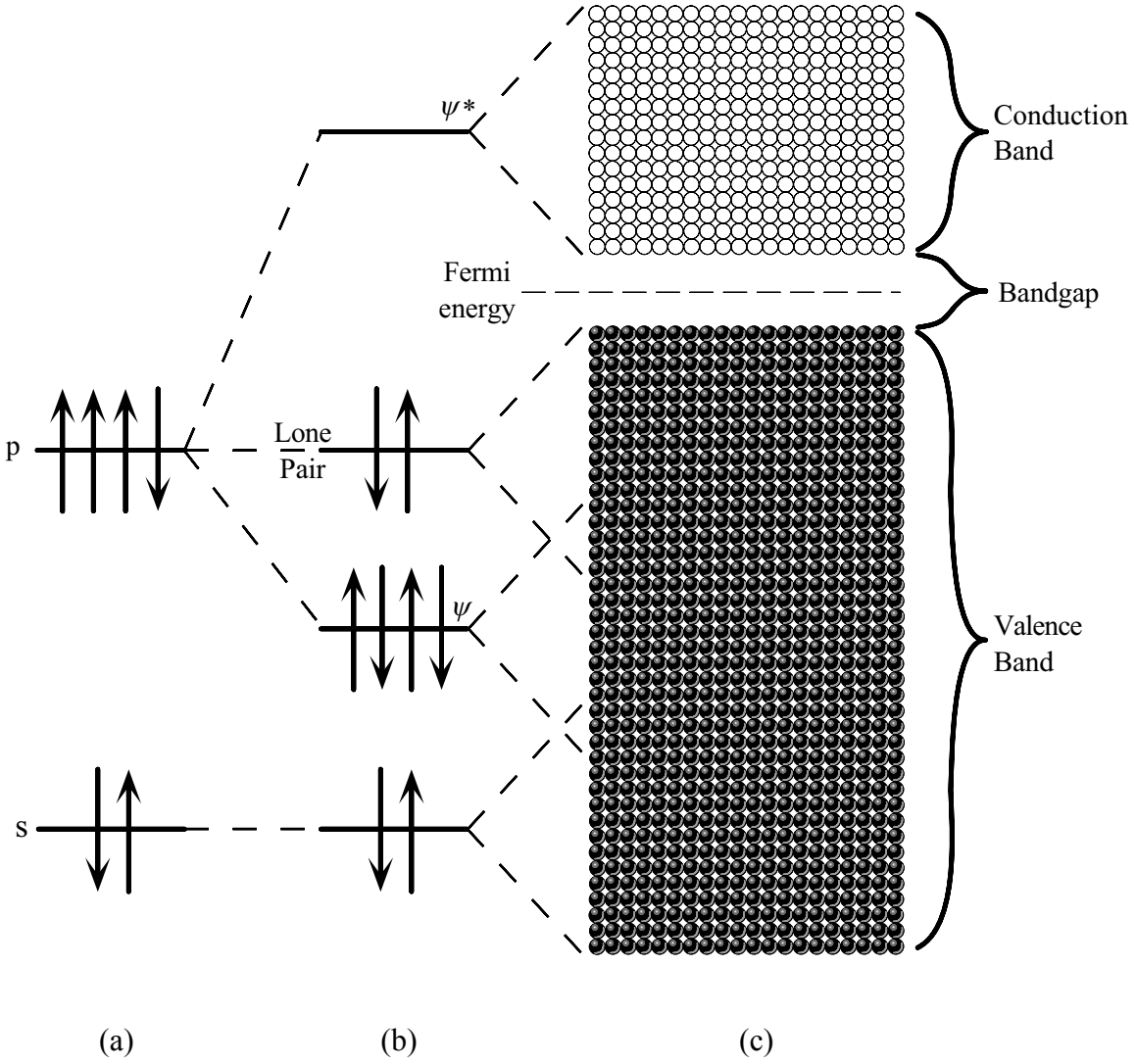

Figure 2-4: Schematic representation showing the covalent bonding of chalcogenide atoms to form a solid with energy bands. (a) Valence shell electron configuration of an isolated chalcogenide atom. (b) Two chalcogenide atoms combine to form two covalent bonds between the four p-state electrons, which leads to the bonding, ψ, and antibonding, ψ^*, states. The two other p-state electrons remain as a lone pair. (c) Bonding interaction of several atoms broaden the atomic levels into bands.

and the lowest empty band is the *conduction band* (CB), see Figure 2-4 (c). The difference in energy from the top of the valence band to the bottom of the conduction band is called the *forbidden gap* or *bandgap* (E_g). Figure 2-4 (c) also shows that for the chalcogenides the valence band is formed by an overlap of the bands from the s-electron states, the p bonding (ψ) states and the two lone pair, p-electrons. It is also clear from this that the top of the valence band consists of the two lone pair, p-electrons.

The probability of finding an electron in a state with energy E is given by the Fermi-Dirac function.

$$f(E) = \frac{1}{1 + e^{\left(\frac{E - E_F}{k_B T}\right)}} \tag{2.2}$$

where E_F is a material constant called the *Fermi energy*, k_B is the Boltzmann constant and T is the temperature in Kelvins. Above absolute zero $E = E_F$ which gives $f(E) = \frac{1}{2}$. This is referred to as the *Fermi level*. Electrons in a solid fill the allowed states up to the Fermi level in accordance with the Pauli exclusion principle.

Solids where the Fermi level lies in the middle of a band are metals and materials where it lies in a gap are insulators. Semiconductors are merely insulators where the bandgap is in the order of a few electron volts (i.e. the gap is relatively small).

The band theory was first derived for the crystalline structure. This is because the long range periodicity of the atomic bonding arrangement made possible a number of important simplifications in the application of quantum mechanics to solids. These bands describe the number of electron states per unit energy per electron at energy E, through a function called the density of states, $g(E)$. This is a significant theory for material science, because it can be used to explain the electrical and optical properties of materials. The density of states diagram for a crystalline semiconductor is illustrated in Figure 2-5 (a). In a crystalline solid the long range order of the atomic structure has two important consequences; (1) The conduction and valence bands have definite edges where the density of states sharply decrease to zero. (2) All the states in the bands

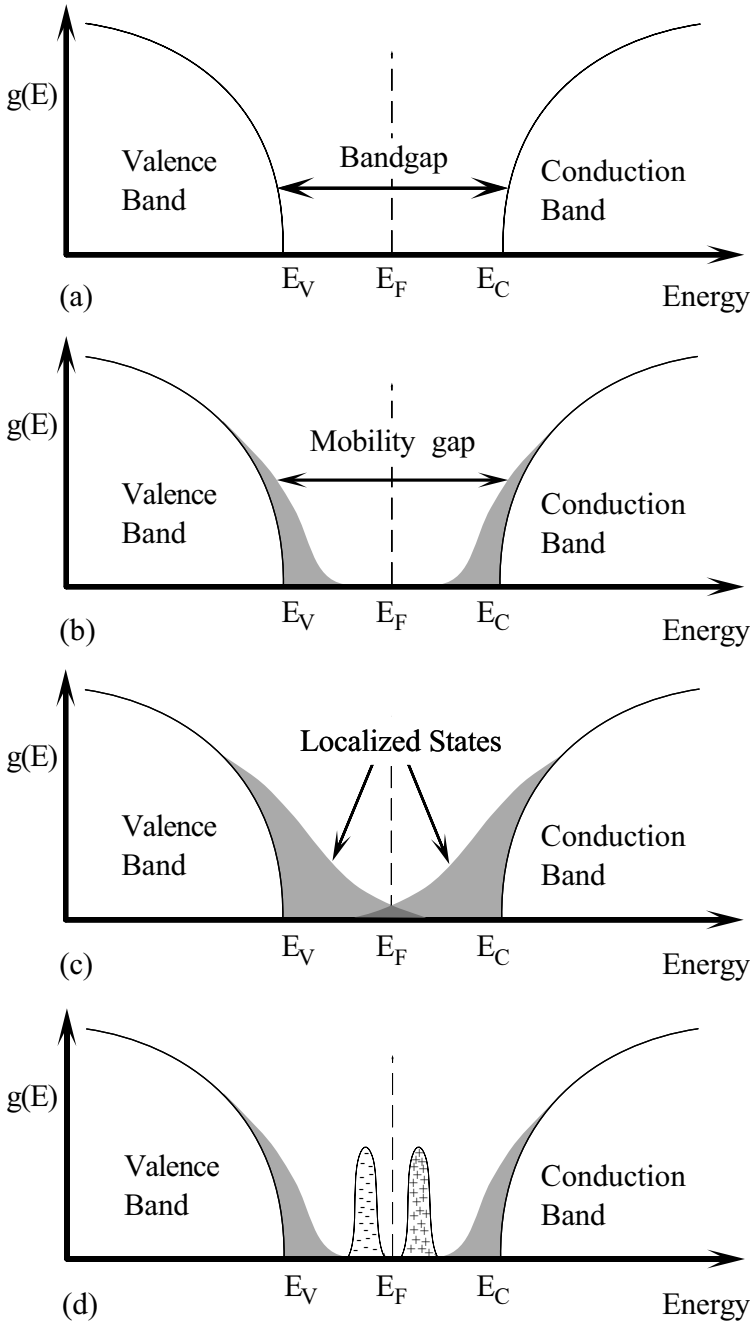

Figure 2-5: Parabolic Density of States (DOS) models for semiconductors. (a) Classic crystalline case showing the well defined edges for the two extended state bands separated by a bandgap. (b) Mott's initial proposed DOS model for amorphous semiconductors showing the smearing out of the band edges caused by local variations in the lattice parameters. (c) Cohen, Fritzsche and Ovshinski (CFO) model showing the localized states extending across the forbidden gap. (d) Marshal – Owen DOS model containing deep donors below acceptors.

extend throughout the solid. Since amorphous materials lack the long range order of their crystalline counterparts, it was long believed that they could not be semiconductors. So imagine the surprise of Goryunova and Kolomiets in 1955 when they discovered that one of their amorphous compositions demonstrated the typical semiconductor behavior of conductivity [1]. Since that time it has become clear that it is not the periodicity but the chemical bonding that distinguishes the properties of a solid.

Anderson [28] was the first to quantitatively show that the effects of disorder on the Schrödinger equation resulted in a localization of some of the states in the band. Basically this means that unlike a crystal an electron in an amorphous material is not free to move through the whole lattice, but is localized in space. Anderson further postulated that these localized states are a result of the degree of disorder in the lattice and not any particular imperfection. Moreover, the magnitude and energy spread of these localized states are proportional to amount of disorder in the atomic structure.

Mott [24] was the first to note that the sharp band edges of crystalline materials was due to the long-range order and that in amorphous materials these sharp edges should disappear. Mott stated that this was due to the changes in the Bloch wave functions at the conduction and valence band edges, E_C and E_V respectively. This produces extended *tails*, which enter the forbidden gap region. This is shown in the energy diagram of Figure 2-5 (b). This model has been proposed to apply to alloy glasses, which contain compositional as well as positional disorder (i.e. pnictide and chalcogenide glasses). Furthermore, if these tails from the conduction and valence bands overlap then they lead to a model that somewhat resembles a metal.

These tail states have a major effect on carrier conduction within an amorphous semiconductor. Carriers in a crystalline structure travel in the conduction or valence band through electronic energy states that extend throughout the entire crystal. Mott argued that from a certain energy on, the electronic states in an amorphous material become extended, which lead to transition energies in the conduction and valence bands that produce a jump in the mobility. These transition energies are called *mobility edges* and are equivalent to band edges of crystalline materials. As well this change in the

mobility of charge carriers led to the idea of a *mobility gap* in amorphous materials, which is also similar to the bandgap of crystalline solids. Mott's postulation of the mobility gap clearly explains how it is possible for amorphous materials to behave as semiconductors.

The model put forth by Cohen, Fritzche and Ovshinsky, known as the CFO model [29], Figure 2-5 (c), is basically an extension of Mott's model. Cohen, Fritzche and Ovshinsky surmised that Mott underestimated the amount of disorder in an amorphous solid. Four principles were used to come to this conclusion: (1) The band tails of amorphous materials depend on the degree of the divergence from perfect periodicity. (2) There are sharp mobility edges that separate the extended states from the localized states in each band. (3) The localized band tails extend across the gap region, which results in an overlap at the Fermi level. This last statement might seem to suggest that there is metallic conduction, but one should realized that the widened tail states are still highly localized in space, as in Mott's model. (4) Amorphous materials are not bound by the strict constraints of long range order found in their crystalline counter parts. As a result each atom can be expected to fulfill its proper valence requirements locally. This removes any distinct structure in the density of localized states in the gap region. It is this last point that results in a contention with the CFO model, as it does not show a structure in the gap region due to defects in the amorphous lattice. This led to the DOS model proposed by Marshall and Owen [30] depicted in Figure 2-5 (d). They noted that defects such as dangling bonds, vacancies, interstitials, impurities, etc. are present in all crystalline or amorphous solids. Such defects lead to additional localized states within the mobility gap of the material. These defects lead to localized energy states in the form of electron and hole traps within the gap region of the material, in addition to the disorder induced tail states. It was previously assumed that the disorder induced states would cover up these defect states, but Marshall and Owen proposed that there would be significant mid gap states caused by these defects. They concluded that the hole traps are acceptor-like, lying about 0.43 eV above the valence band [31]. The position of the Fermi level is determined by the donor-like and acceptor-like trap bands in the mobility gap. They also surmised that the concentration of donor and acceptor traps self-adjust to ensure that the Fermi level remains near the center of

the mobility gap. This has significant consequences for predicting the electronic properties of the material, because even small concentrations of these mid gap states can make the doping of the semiconductor with donors or acceptors ineffectual.

2.2.2 Glass Transition Temperature

The term glassy or non-crystalline material has been used synonymously with the term amorphous material [23]. But, it is essential to recognize that amorphous semiconductors are metastable thin solid film materials, [23] whereas a glass is a viscous liquid, essentially that of a frozen liquid or supercooled liquid [22]. This is best demonstrated by the Volume-Temperature relationship, as shown in Figure 2-6. If a liquid is slowly cooled from a temperature T, it solidifies at a temperature T_m (melting temperature) to form a crystalline structure with long range order, (Path a → b → c → d). From this it is observed that a crystal solid is formed by a discontinuous solidification in which a solid appears and grows in the liquid. Hence, the bonds have time to align themselves into proper orientation and a crystal with a long range atomic

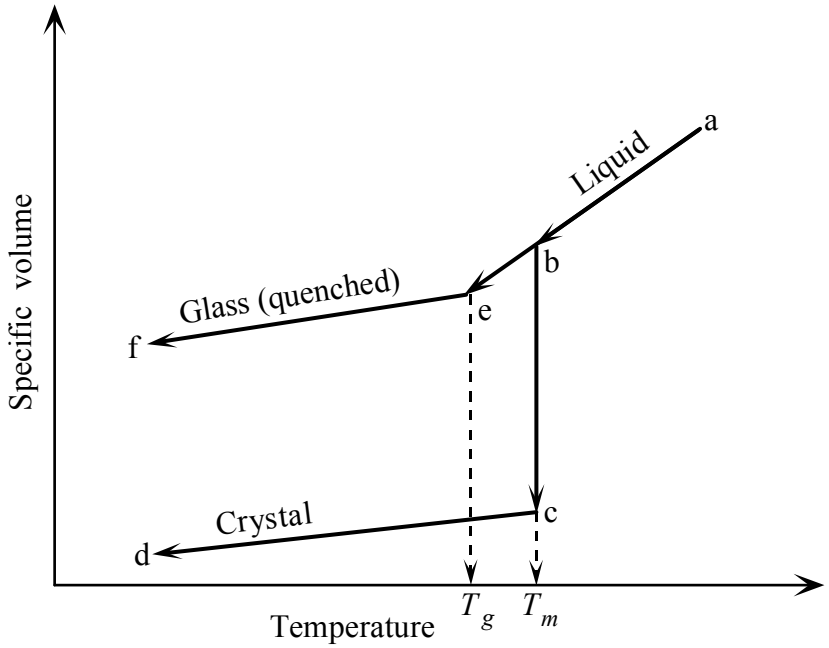

Figure 2-6: Specific volume versus temperature for glass and crystalline material states.

network is formed. This is a first-order phase transition and is the result of an exothermic reaction (heat is released). On the other hand, if a solid is heated, endothermic reaction (heat is absorbed), it melts at a temperature T_m and enters the liquid phase. This melting temperature T_m is a material specific property and depends on the atomic bonding.

To obtain a glass, or amorphous material, the liquid is quickly cooled or quenched. The Volume –Temperature path follows a → e → f where point e represents the glass transition temperature T_g, when the viscosity of the liquid is approximately $10^{13} – 10^{14}$ poise [23]. An arbitrary viscosity value of 10^{15} poise is commonly taken to characterize a glass [23]. By rapidly quenching the liquid, the atomic motions become so sluggish that the atoms do not have time to align for proper bonding. This cooling rate is measured relative to the crystallization rate and is dependent on atomic diffusion of the material being quenched. The result is that of a 'frozen liquid' that is the bonding geometry resembles that of a liquid in solid form as shown in Figure 2-2 (b).

2.2.3 State of Disorder

If we represent the condition of a system by its free energy, $E_{(Free)}$, then this can be related to the enthalpy H, internal energy of the system, and the temperature T by;

$$E_{(Free)} = H - TS \tag{2.3}$$

where S is the condition or state of disorder. The gas, liquid or crystal state corresponds to a minimum point in thermodynamic free energy, as represented in Figure 2-7. Plot 1 corresponds to Figure 2-1 (c) when the material is in its liquid phase, $T > T_m$, the melting temperature. Plot 2 is the free energy state when the temperature T is equal to the melting temperature T_m. If the liquid is allowed to slowly cool (path a → b → c → d on Figure 2-6), then we can follow the points labeled 'crystal' on the thermodynamic diagram from plot 2 to 4 and the resulting crystal structure has long range order as shown in Figure 2-2 (a).

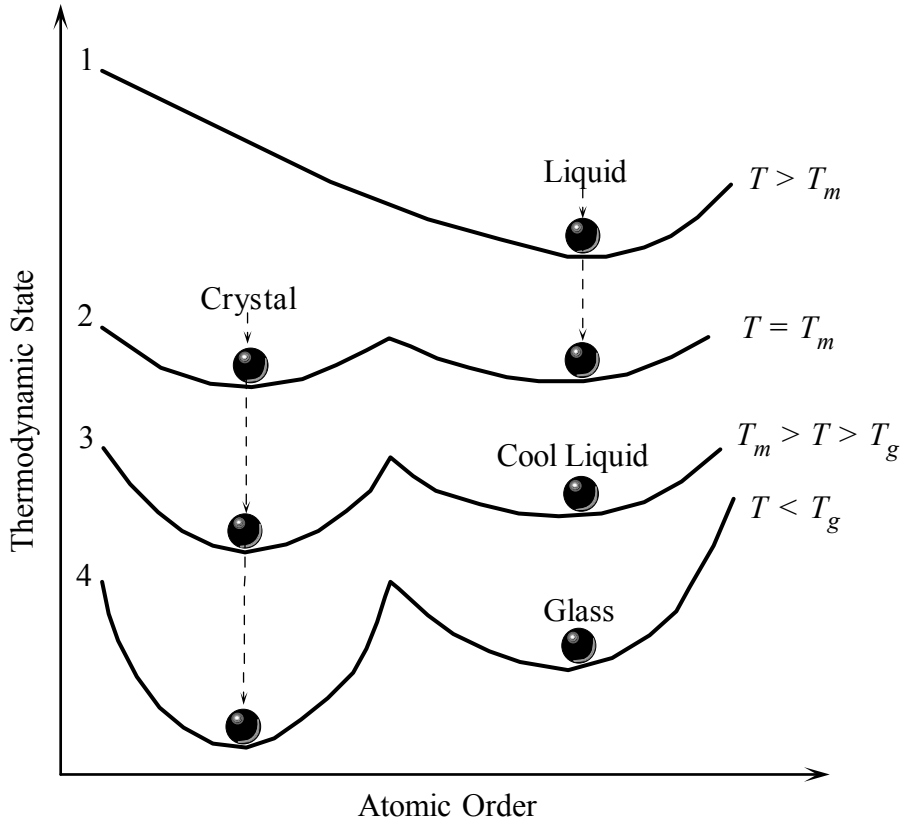

Figure 2-7: Changes in the thermodynamic state (free energy) of a material versus atomic order at various temperatures.

If the liquid is cool, as indicated in plot 3 of Figure 2-7 then the atomic bonding must overcome a greater energy barrier for proper crystal bonding, but as previously stated the atomic motion has become sluggish and therefore do not posses the necessary kinetic energy to overcome this barrier. Hence, the state of the solid is a 'frozen liquid', which maintains the disordered structure, see Figure 2-2 (b). This results in a displacement from the free energy minimum point when the liquid is frozen at T_g, as shown in Figure 2-7, plot 4. Consequently, an amorphous solid is thermodynamically in a non-equilibrium state

2.2.4 Electrical Properties

Solids where the Fermi level lies in the middle of a band are metals and materials where it lies in a gap are insulators. Semiconductors are merely insulators

where the bandgap is in the order of a few electron volts or less (i.e. the gap is relatively small). By this definition amorphous chalcogenide solids are semiconductors as they typically have a bandgap of 1 - 2.5 eV. Even though oxygen is a Group VI element (i.e. a chalcogenide), the bandgap of oxide glasses is in the order of 10 eV and as a result are considered insulators.

Metals freely conduct electricity because electrons are in a partially filled band and can easily gain energy from an applied electric field and drift. The bandgap of a semiconductor restricts this free electron movement and as a result these materials have a higher resistance. Conduction in a crystalline semiconductor is mainly due to charge carriers (electrons in the conduction band and holes in the valence band), moving in the extended states. For simplicity if we assume that one carrier sign dominates in this extended state transport then the conductivity, σ, is given by

$$\sigma = ne\mu \tag{2.4}$$

where n is the carrier density, e is the electric charge and μ is the drift mobility (average velocity per unit electric field). Free electrons and holes are able to drift in the extended states under the bias of an applied electric field. The free electron hole pairs are created by thermal vibrations of the crystal lattice. This behavior is also found in many semiconducting chalcogenide glasses such as the composition used in our research, As_2Se_3 [25]. This means that the conductivity is dependent on temperature. For this type of system, where the current is carried by excited electrons, the D.C. conductivity, σ_{DC}, as a function of temperature can be described as

$$\sigma_{DC}(T) = \sigma_{\min} e^{\frac{-\Delta E}{k_B T}} \tag{2.5}$$

where $\sigma_{\min}$ is a material constant typically in the range of 10^2 to 10^4 Ω^{-1} cm^{-1}, k_B is the Boltzmann constant, T is the temperature in Kelvins and ΔE is the activation energy $(\Delta E = E_C - E_F)$. Since E_F is near the middle of the bandgap for most amorphous

semiconductors then the activation energy is typically taken as

$$\Delta E \approx \tfrac{1}{2} E_g \tag{2.6}$$

where E_g is the difference in energy from the valence band, E_V, to the conduction band, E_C, ($E_g = E_C - E_V$).

The drift mobility of charge carriers in crystalline semiconductors are limited by the mean time between scattering events, such as impurities, defects and lattice vibrations. An energy level diagram in real space is depicted in Figure 2-8. An electron that has been excited to the conduction band, A, above the mobility edge, E_C, will drift to the right under an applied left pointing electric field. Scattering events irregularly impede the charge carrier motion within the extended states. In an amorphous material the localized states severely hamper a charged carrier's mobility. It was shown in Section 2.2.1 that the localized states create band tails that extend into the gap region and these act as trapping centers. A trapping center is indicated at point B on Figure 2-8. Here the excited electron, A, is trapped and later released by the localized state. The time between trapping and release events depends on how deep (distance from the

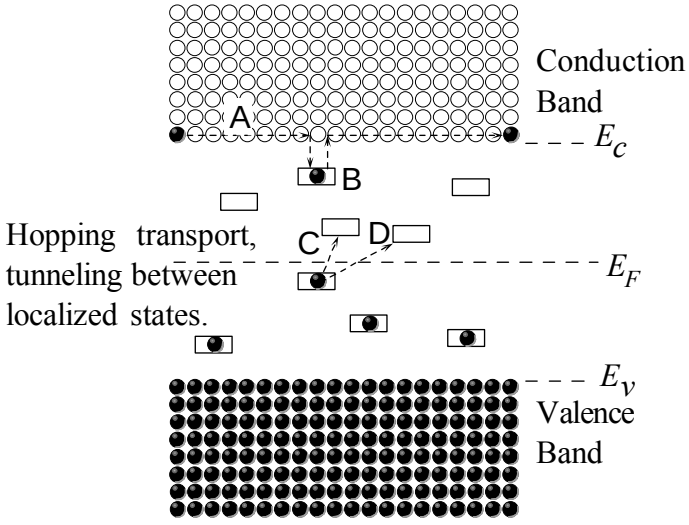

Figure 2-8: Energy level diagram for electronic conduction mechanisms in an amorphous semiconductor.

mobility edge) the localized state is within the gap region. Consequently, the deeper the trap, the longer the release time.

An interesting phenomena that arises as a specific consequence of strong disorder is called *hopping* [32]. The term hopping is an abbreviation for the phonon assisted quantum mechanical tunneling of an electron from one localized state to another. Figure 2-8 depicts two such possible tunneling processes, labeled C and D. It is believed that the dominant mechanism for electrical conductivity in a chalcogenide glass is the hopping transport [33].

Conduction within semiconductors can also be altered by external stimuli such as light and/or x-ray photons. If the photons possess enough energy they will excite electrons from the valence band to the conduction band and as a result this changes the conductivity of the material. This phenomena is known as photoconductivity and many current semiconductor devices exploit this property.

2.2.5 Optical Properties

The previous section stated that the conductivity of a semiconductor can be changed by the external stimulation of photons, provided these photons possess sufficient energy. The energy of a photon is given as

$$E_{ph} = h\nu \tag{2.7}$$

where h is Planck's constant and ν is the frequency of the photon (i.e. $\nu = \frac{\lambda}{c}$). If the photon energy, $h\nu$, is greater than or equal to the bandgap energy, $E_g = E_c - E_v$ of the semiconductor, then an electron can be stimulated from the top of the valence band, E_v to the bottom of the conduction band, E_c, and the photon is absorbed as shown in Figure 2-9. If the photon energy is much greater than E_g, then the electron is excited to a level higher in the conduction band above E_c. The excess energy of the electron, $h\nu - E_c$, in this state is lost due to lattice vibrations (phonons), see Figure 2-9. Now if the photon energy is less than E_g, then the photon is not absorbed. For these wavelengths the semiconductor is transparent. This is true only if no states lie within the bandgap. Here

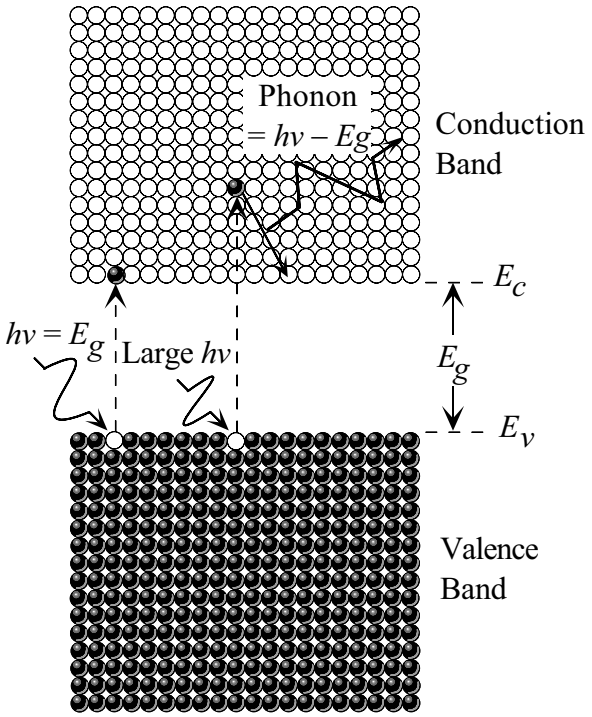

Figure 2-9: Photon absorption generating electron hole pairs.

is the difference between a crystalline semiconductor and the amorphous semiconductor. As the band models show in Figure 2-5 for the crystalline semiconductor (a) the band edges are sharp and well defined. Whereas the band edges for the amorphous semiconductor (b), (c) and (d) have tails that extend into the bandgap. As discussed in Section 2.2.1 these tails are present because an amorphous material has localized states within the bandgap. The result is that photons possessing energies less than the bandgap can create electron hole pairs in the amorphous semiconductor.

A photon has to be absorbed in order to stimulate an electron from the valence band to the conduction band. Unfortunately, there are only so many photons that possess the proper energy per unit volume for this stimulation process. As well absorption is dependent on the material thickness. So if we consider a beam of photons with an intensity of I_o is incident on a semiconductor as illustrated in Figure 2-10. Then at a distance x into the semiconductor the intensity is $I(L)$ and δI is the change in intensity due to absorption after the beam passes through a small elemental volume of

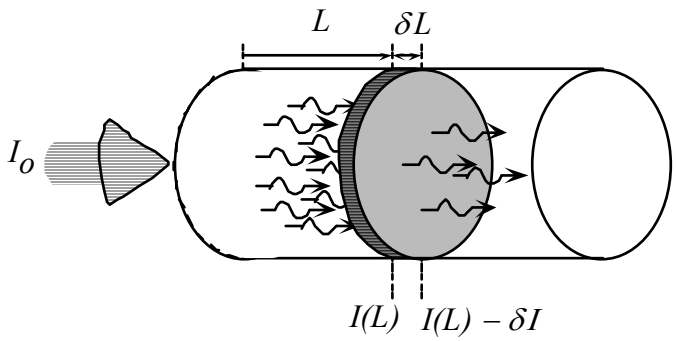

Figure 2-10: Absorption of photons within a small elemental volume of width δL.

thickness δL from L. Therefore, δI is dependent on the number of photons entering this volume, $I(L)$, and the volume thickness δL. So

$$\delta I = -\alpha I \delta L \tag{2.8}$$

where α is a proportionality constant called the *absorption coefficient* and is a material property defined as

$$\alpha = -\frac{\delta I}{I \delta L} \tag{2.9}$$

with units of length^{-1} (m^{-1}). Integrating equation (2.9) with constant wavelength yields the *Beer-Lambert law*

$$I(L) = I_o e^{-\alpha L} \tag{2.10}$$

which indicates that the transmitted intensity decreases exponentially as the beam passes through the material. The distance over which 63% of the photons are absorbed is called the *penetration depth*, δ, which is defined as,

$$\delta = \frac{1}{\alpha} \tag{2.11}$$

As previously stated the difference in optical properties of crystalline and amorphous semiconductors arises from the localized states which are present in the

forbidden region of amorphous materials. This makes it possible for a more versatile range of excitation and relaxation processes to occur. A typical response curve showing the optical absorption, α, dependence on the photon energy, *hv*, is plotted in Figure 2-11. The response is sectioned into three different regions. Each region represents the different states responsible for optical absorption. Region 3 deals with interband absorption (valence to conduction band) where photon energies correspond to the bandgap energy. Typical absorption coefficients lie in the range of $10^4 < \alpha < 10^6$ cm^{-1}. It is normally assumed that the density of states in this region can be expressed in a power law form with $g_v(-E) \propto E^p$ and $g_c(E) \propto (E - E_g)^s$. Then the photon energy dependence of the absorption is

$$(\alpha hv)^x = C(hv - E_g) \tag{2.12}$$

where $1/x = p+s+1$ and C is a proportionality constant. If the density of states for both

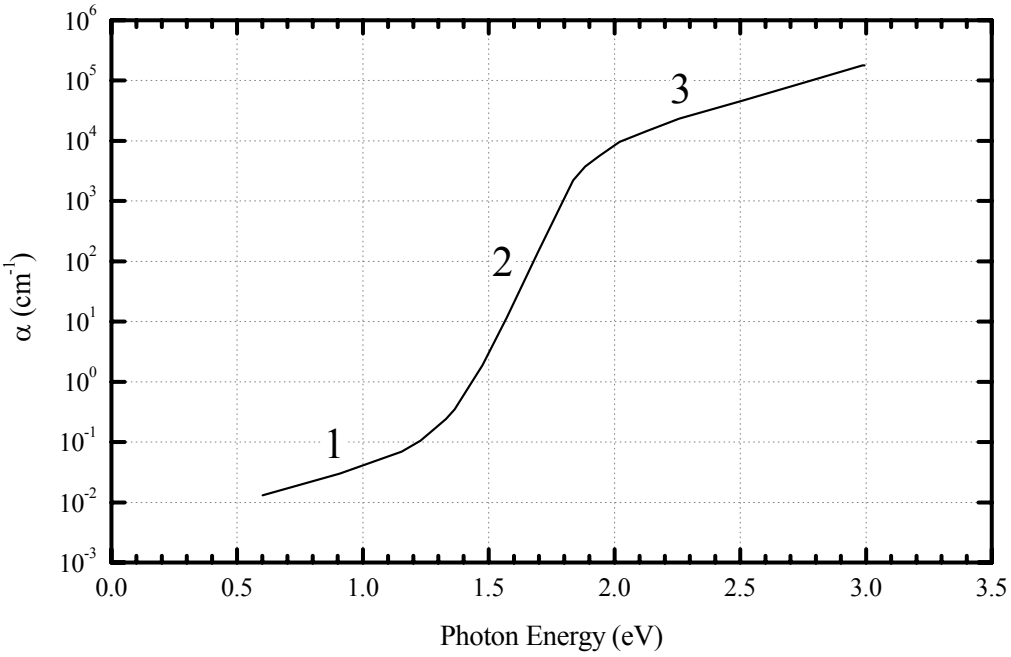

Figure 2-11: Typical logarithmic absorption versus photon energy curve for an amorphous semiconductor (Data extracted from [21]). Region 1 is the absorption tail, 2 the Urbach edge and 3 the power law region.

conduction and valence states are parabolic then one gets p = s = 1/2 and the photon energy dependence of absorption becomes

$$(\alpha h\nu)^{\frac{1}{2}} = C\left(h\nu - E_g\right)$$

This form of the absorption is observed experimentally for many amorphous semiconductors, and some examples are shown in Figure 2-12. This is typically known as a Tauc plot. Notice that a majority of the absorption plots linearly for $(\alpha h\nu)^{\frac{1}{2}}$ as a function of $\left(h\nu - E_g\right)$. Also if this straight line is extended to the photon energy axis we obtain the bandgap, E_g, for the compound. As a result the bandgap is also known as the optical gap, E_o, or the Tauc bandgap.

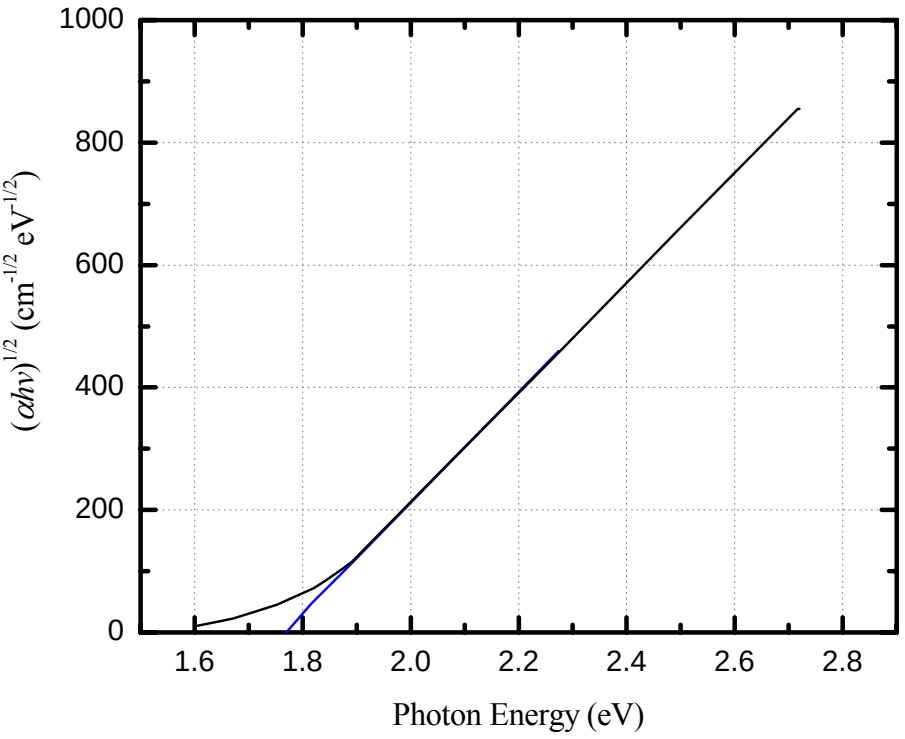

Figure 2-12: As_2Se_3 optical absorption edge whose functional dependence on photon energy is given by $(\alpha h\nu)^x = C(h\nu - E_g)$. The intercept indicates the optical gap, E_o (Data extracted from [7]).

There are some compounds that do not exhibit any simple power law relationship with the absorption edges. As a result it is not possible to obtain the optical gap energy from a Tauc plot. An alternative method is to take the photon energy at which the absorption coefficient reaches 10^4 cm^{-1}. The optical gap is then conventionally denoted as E_{04}.

Region 2 of Figure 2-11 is known as the *Urbach edge* region. Here it has been experimentally found for most amorphous semiconductors that the absorption decreases with photon energy less quickly than the power law predicts. This is a result of the transitions between tail states in the valence and conduction bands, see Figure 2-5 (b), which causes a tailing of the absorption edge into the bandgap. Absorption in the Urbach edge region is more accurately found to obey an exponential dependence on photon energy

$$\alpha \propto Ce^{-K(E_o - h\nu)} \tag{2.13}$$

where C is a proportionality constant and K is a temperature dependent constant, (typical values at room temperature are in the range of 10 – 25 eV^{-1}). Typical absorption coefficients for this region have a range of 1 – 10^3 cm^{-1}. The exponential relationship is schematically shown for As_2Se_3 in Figure 2-13. This characteristic is so widespread among amorphous semiconductors that it appears to be a general feature. Similar behavior has also been observed in crystalline alkali halide solids. The problem is that the Urbach phenomenon is not well understood, even in the crystalline materials. So the level of understanding for this occurrence in amorphous compounds is even more tenuous.

Region 1 of Figure 2-11 is called the absorption tail or shoulder and typically has absorption coefficients less than 1 cm^{-1}. Transitions between defect states in the middle of the energy gap and extended states in the valence and conduction bands are responsible for this region. Therefore the photon energy required to excite these transitions is much smaller than the bandgap energy and usually involves wavelengths in the far infrared spectrum. It can be said that the absorption coefficient value in this tail is a measure of the density of defect states present in the material.

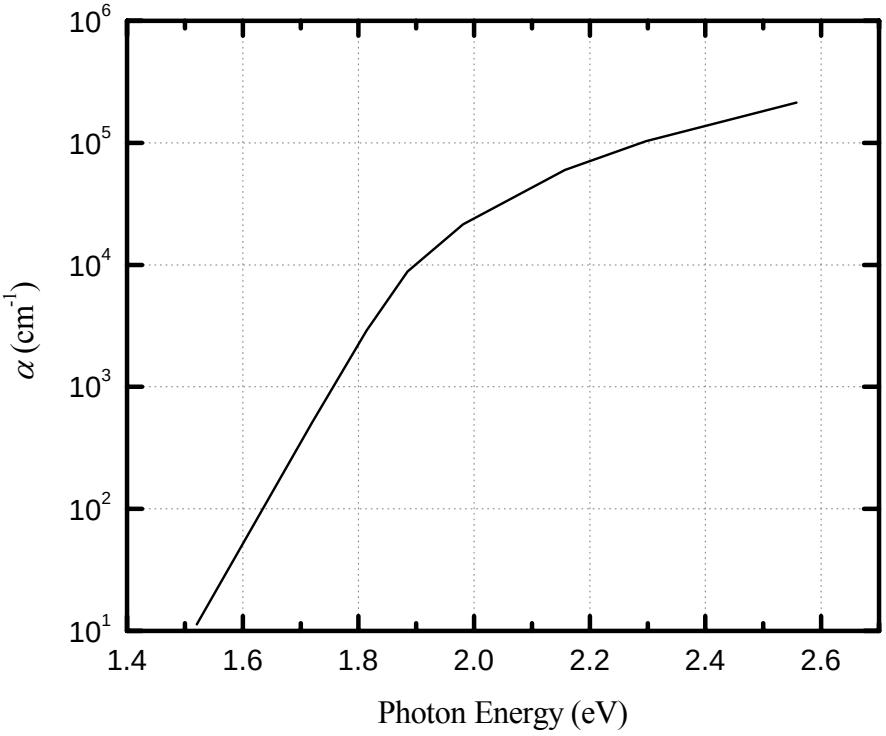

Figure 2-13: Optical absorption edges showing an exponential behavior for amorphous As_2Se_3 at room temperature. (Data extracted from [7]).

2.3 VAPs and IVAPs

In 1972 Kastner [34] pointed out that the chemical bonding of chalcogenide atoms is fundamentally different from the structure of all other amorphous semiconductors due to the two outer lone pair electrons that do not participate in the bonding structure. This along with the lack of a measurable density of unpaired spins is possibly the most extraordinary feature of the amorphous chalcogenide material. Mott [7] states that a major puzzle in the understanding of chalcogenide glasses has been the absence of electron spin resonance along with evidence that the Fermi energy is pinned and the finite density of states. He goes on to say that one way out would be to assume that the density of states is in fact zero. The problem is that the Fermi energy is determined by deep donors lying below the acceptors near the middle of the bandgap, refer to Figure 2-5 (d). Another more plausible explanation of the experimental results

was proposed by Anderson [35]. He postulated that the spin pairing of electrons at the defect states would be energetically favorable over unpaired spins. As a result the lowest energy state would have no unpaired spins. Anderson goes on to suggest that this is due to a *polaron effect,* which involves an electron−phonon interaction that will polarize its surroundings into a lower energy configuration. Street and Mott [36] used Andersons concept for a different version of the model. Here they used the notation D^0 for an unpaired electron or dangling bond, DB, where the superscript indicates the charge state. The dangling bond defect could have two other states: (1) an under coordinated atom that is a negatively charged defect, D^-, i.e. the dangling bond has an added electron. (2) an over coordinated atom that is a positively charged defect, D^+, i.e. the dangling bond has an electron removed. These defects are related in that the following reaction is assumed to take place.

$$2D^0 \rightarrow D^+ + D^-$$

The configuration coordinate diagram depicted in Figure 2-14 shows that this reaction is exothermic. That is the total energy of electrons plus lattice (a polaron) that is associated with the two charged defects, D^+ and D^- is lower than the two neutral defects, D^0.

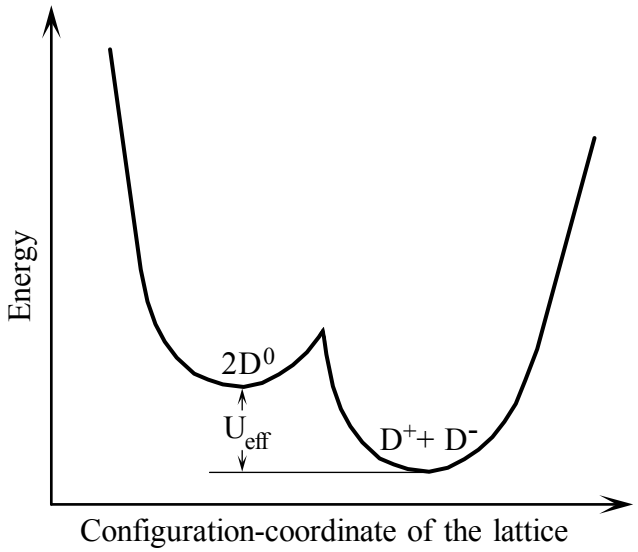

Figure 2-14: Configuration-coordinate diagram for the formation of a D^+D^- pair through the exchange of an electron between two D^0 centers.

Kastner, Alder and Fritzsche [38] used chemical bond arguments to provide a better understanding of this process. They used the notation of C_1^0 for D^0, C_1^- for D^- and C_3^+ for D^+, where C stands for a chalcogen atom, the subscript indicate the coordination number and the superscript the charge. Therefore the normally two fold coordinated selenium atom would be written as C_2^0.

The reaction that takes place consists of two stages; (1) an electron from a dangling bond, C_1^0 defect is removed and the now C_1^+ defect interacts with the lone pair of a neighboring chalcogen, C_2^0 resulting in a three fold coordinated chalcogen, C_3^+. This is similar to the proper bonding configuration of a pnictide atom and results in a lower energy state. (2) the excess electron can move to any of the three nearest neighboring atoms. Then the bond between that atom and the three fold coordinated atom breaks, resulting in a singly bonded chalcogen atom with an extra electron, C_1^-. The formation of $C_1^- C_3^+$ (or Street and Mott's model $D^- D^+$) pair was termed by Kastner, Adler and Fritzsche as a *valence alternation pair*, VAP, and is illustrated in Figure 2-15 (a). If the C_1^- and C_3^+ defects are directly connected then the term *intimate valence alternation pair*, IVAP, is used, which is shown in Figure 2-15 (b). Both of these reactions on their simplest level can be viewed as a type of bond switching.

Existence of negative correlation energy and valence alternation in amorphous selenium from experimental evidence was reported by Kolobov et al. in 1997 [39]. In this paper they combined results from optically induced electron spin resonance, ESR, and extended x-ray absorption fine structure, EXAFS, measurements. The experiments were carried out *in situ* under identical conditions and provide clear evidence for the existence of these two phenomena.

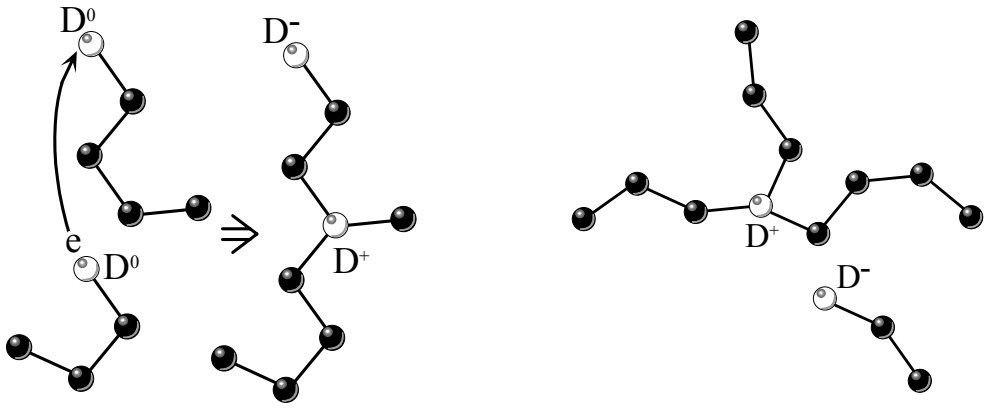

(a) (b)

Figure 2-15: Formation of three fold coordinated D^+ and singly coordinated D^- defect centers from two D^0 centers at the ends of a Se chain, valence alternate pair (a) and intimate valence alternate pair (b).

2.5 Summary

A brief overview of the differences between amorphous and crystal semiconductor was presented in this chapter. In particular how the freedom and flexibility of an amorphous structure could lend itself to a more richer variety of induced effects. The tradeoff is a very complex structure that is not easily described with mathematics.

Chapter 3

Photoinduced Changes in Chalcogenide Thin Films

3.1 Introduction

Photoinduced effects include changes of composition, phase, electronic and atomic structure [16, 40]. This is accomplished by exposing the material to light where the photon energy is comparable to that of the bandgap. The absorbed photon then generates an electron hole pair. If the charges separate then they can give rise to photoconductivity or they can recombine. Recombination can occur either radiatively resulting in photoluminescence or nonradiatively. In theory, nonradiative recombination of photoexcited electron hole pairs could structurally and optically change the material to a state different than the unilluminated one. Typically these changes are metastable where it can take months before the induced effects disappear completely.

With crystals the constraints that are imposed on the positions that atoms may occupy by the rigid structural periodicity severely restricts the options available to any stimulated electron hole pairs. Amorphous semiconductors and insulators on the other hand can exhibit a wide variety of photoinduced effects due to the atomic structural disorder which can cause localization of electron and hole states in the forbidden gap [24]. The lack of lattice rigidity creates a structure with more freedom and flexibility to enhance photoinduced metastable changes as a result of stimulated electron hole creation events. This along with the low coordination number and lone pair electrons at the top of the valence band makes it easier to deform the lattice and allow bond switching or extra bond formations to occur. These are reasons why photostructural changes are unique to amorphous chalcogenides and not observed in their crystalline counter parts or amorphous pnictides.

Photoinduced changes can be classified according to whether the effect is transient or metastable. Transient photoinduced effects include photoconductivity, photoluminescence, and light induced Electron Spin Resonance, ESR. These effects typically die off milliseconds after they are induced whereas metastable induced effects can persist for months and sometimes years before they completely disappear. The metastable effects can be further subdivided into reversible and irreversible groups. The last category is vectoral and scalar effects. The first two sections of this chapter deal with explaining the differences between reversible, irreversible, scalar and vectoral effects. This is followed by an explanation of photoinduced refractive index change and photoinduced anisotropy. The chapter is then ended by presenting some existing models that try to explain these effects.

3.2 Reversible and Irreversible

An effect is considered reversible, if the initial state of the sample prior to irradiation can be restored at temperatures below the glass transition temperature, T_g [21]. Irreversible effects are seen in as-deposited samples typically as an absorption edge shift. Figure 3-1 illustrates the reversible and irreversible absorption edge shift for an As_2S_3 sample. Upon irradiation of bandgap light the as-deposited state, solid line, shifts toward lower photon energies (longer wavelengths), dotted line. After annealing the sample at a temperature close to the glass transition temperature the absorption edge shifts back to a higher photon energy (shorter wavelength), dashed line, but does not fully recover to the as-deposited state. Subsequent exposure/annealing cycles can be repeated several times (indicated by points 2, 3, 4, 5, 6 and 7 of Figure 3-1) without losing the reproducibility of the process. The difference between solid line and dashed line is the irreversible effect and is a result of the annealing process. During the irradiation or annealing process it is believed that the 'wrong' homopolar bonds (As–As and S-S) are broken and form more energetically favorable heteropolar bonds. The result is a more chemically ordered glass network.

Photoinduced anisotropy is a totally reversible effect as it depends only on the polarization orientation of the inducing light source. Buildup of linearly photoinduced

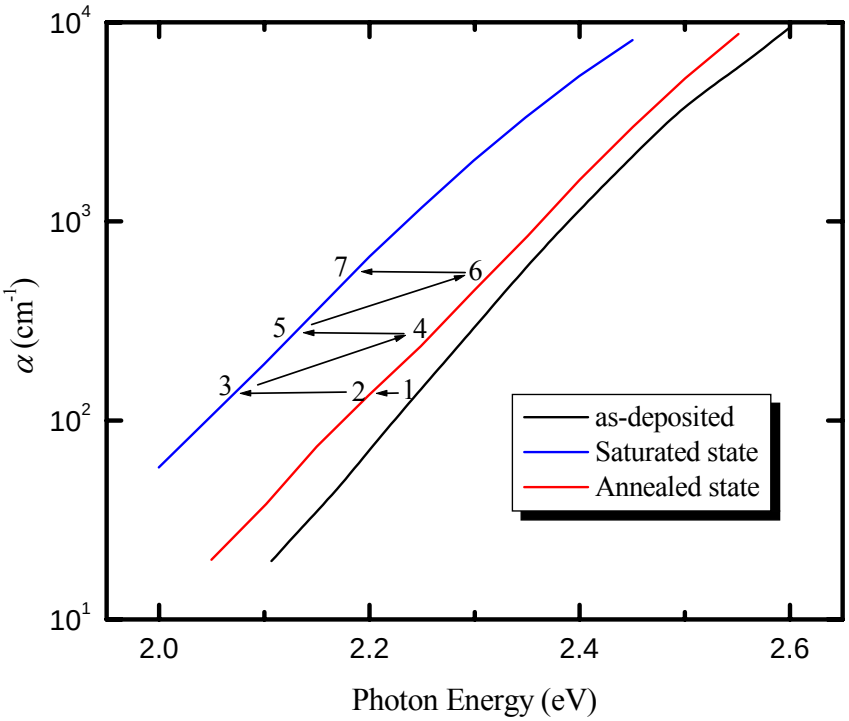

Figure 3-1: Reversible photodarkening in an amorphous As_2S_3 film. Solid line is the as-deposited state, dotted line is the saturated photodarkened state and the dashed line is the annealed state (Data extracted from [41]).

dichroism can be erased by circularly polarized or unpolarized light [42] as well as thermal annealing, often relaxing at room temperature [12]. Consequently, photoinduced anisotropy is a totally reversible effect. Further details will be explained in the following sections.

3.3 Photoinduced Effects

Basically a photoinduced effect that relies on the polarization direction of the inducing light is referred to as a vectoral effect. Scalar effects therefore have no polarization orientation dependence. Often both vectoral and scalar effects occur simultaneously from the same inducing source for many chalcogenide compounds [12, 43], but experimental data show them to display completely different in characteristics [42]. These characteristics include kinetics, temperature and spectral excitation dependency [42, 44, 45]. Lyubin and Tikhomirov [42] showed that the buildup and

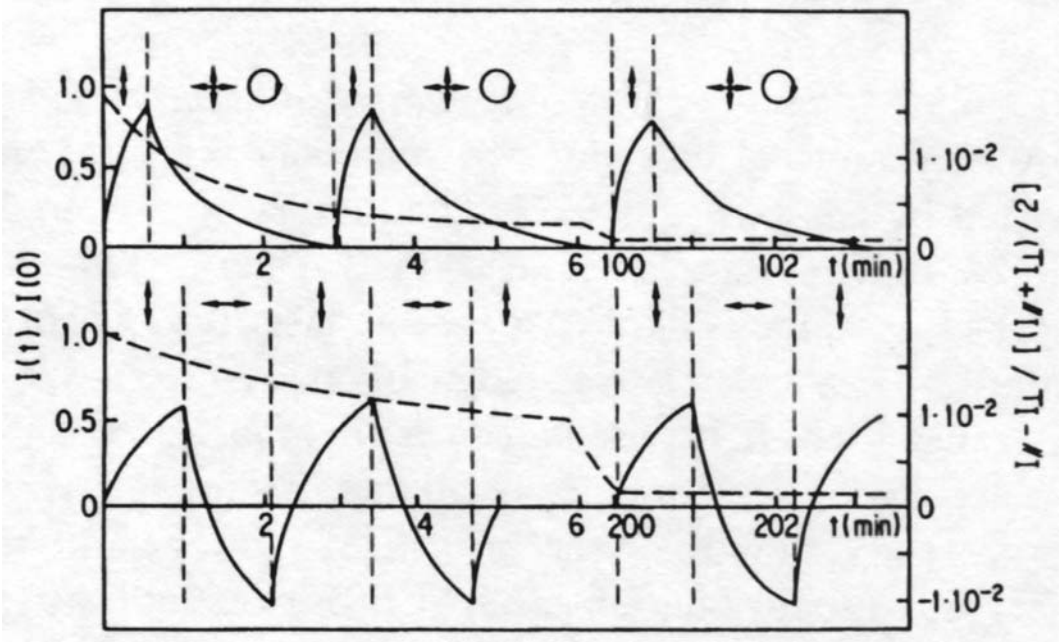

Figure 3-2: Relative transmissions of photoinduced scalar and vectoral effects in an amorphous $As_{50}Se_{50}$ film. Solid lines indicate the kinetics of buildup and erasure (top) and reorientation (bottom) of photoinduced dichroism. Dashed lines are the photodarkening kinetics. Arrows indicate the light polarization (From [42]).

destruction of photoinduced dichroism (a vectoral effect) was completely independent from the photodarkening (a scalar effect) mechanisms. This is very effectively demonstrated in Figure 3-2, where the simultaneous measurements of the buildup and destruction or reorientation of photoinduced dichroism along with photodarkening are displayed. For complete disappearance of a scalar effect the sample should be annealed at approximately 180 °C. Whereas vectoral effects can be erased at a much lower temperature, typically 100 °C, but frequently they relax even at room temperature [43]. The spectral dependency vary in that vectoral effects are more efficiently induced by irradiation of sub-bandgap photon energies that lie on the absorption edge and less so from higher energy photons. In contrast, scalar effects are more efficiently induced by photons with bandgap energies and less so by lower energy photons [44, 45]. Finally, the most compelling fact indicating differences between scalar and vectoral effects was the discovery of large photoinduced dichroism in some chalcogenide compounds that do

not exhibit a scalar effect [42, 43].

3.3.1 Photoinduced Scalar Effects

The photoinduced scalar effects discussed in this section include Photodarkening, PD, Photobleaching, PB, and Photorefraction. The optical darkening of a material upon illumination is referred to as Photodarkening. The earliest observation of this effect was made by Berkes et al. [46]. They observed that a dark area appeared on a 1 μm film of As_2Se_3 when exposed to a focused microscope light. Figure 3-3 is a picture of an As_2Se_3 thin film sample showing three photodarkened spots. This effect is caused by a reduction in the optical gap of the material and is seen as a red shift (toward lower photon energies or longer wavelengths) of the absorption edge, Figure 3-4.

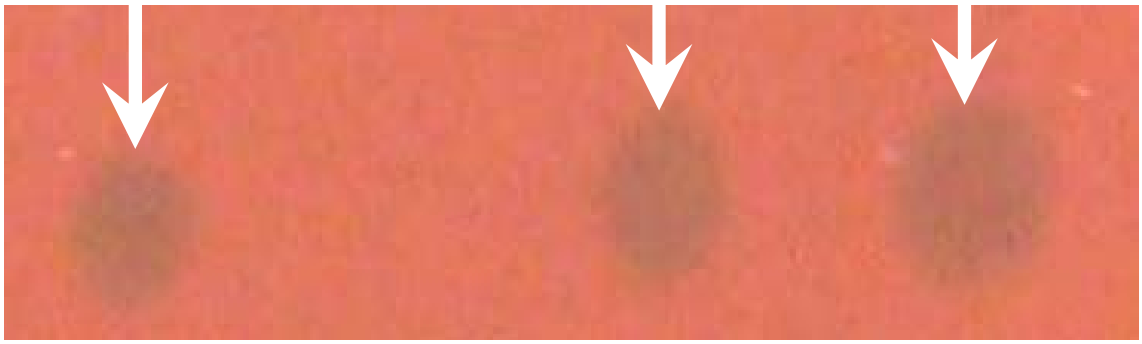

Figure 3-3: As_2Se_3 thin film sample arrows indicate photodarkened spots.

Photobleaching is the opposite of photodarkening in that the material will optically lighten upon illumination. This is due to an increase in the optical gap of the material and is seen as a blue shift of the absorption edge, toward higher photon energies or shorter wavelengths.

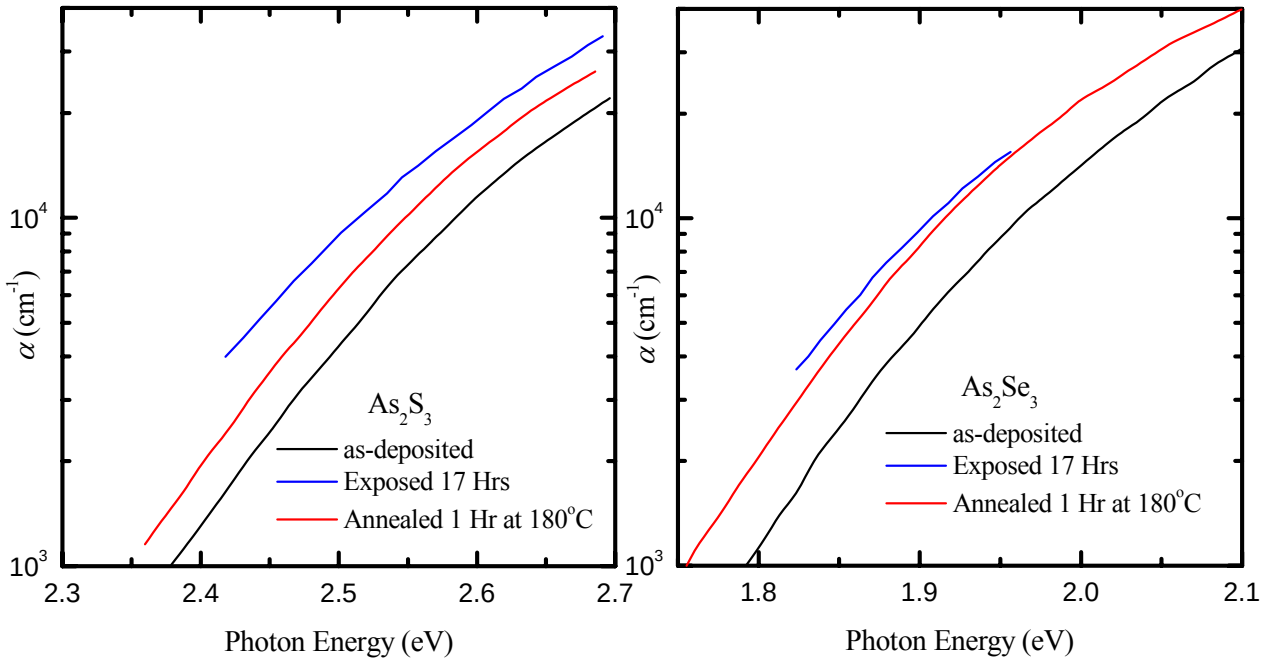

Figure 3-4: Effect of illumination and annealing on the optical absorption edge of evaporated amorphous As_2S_3 and As_2Se_3 thin films (Data extracted from [8]).

An increase or decrease in the absorption coefficient appears to depend on the material composition and/or preparation conditions. Typically photobleaching is found in Ge chalcogenide compounds [47] but has also been seen in obliquely deposited As_2S_3 films [21]. Whether the material is photodarkened or bleached a change in the refractive index also results. This refractive index change upon illumination is referred to as photorefraction.

The temperature dependence of the photodarkening effect has been studied by Tanaka [48] for several chalcogenide glasses. Tanaka showed two points: (1) that no photodarkening can be induced if the sample is at the glass transition temperature, T_g. This is because at the glass transition temperature the rate of inducing the photodarkening is equal to the annealing rate, (2) that an inverse relationship between temperature and the amount of shift in the absorption edge upon photostimulation exists. As the sample temperature, T_i, is decreased, the magnitude of shift in the absorption edge increases. This is clearly shown for several chalcogenide compounds in Figure 3-5.

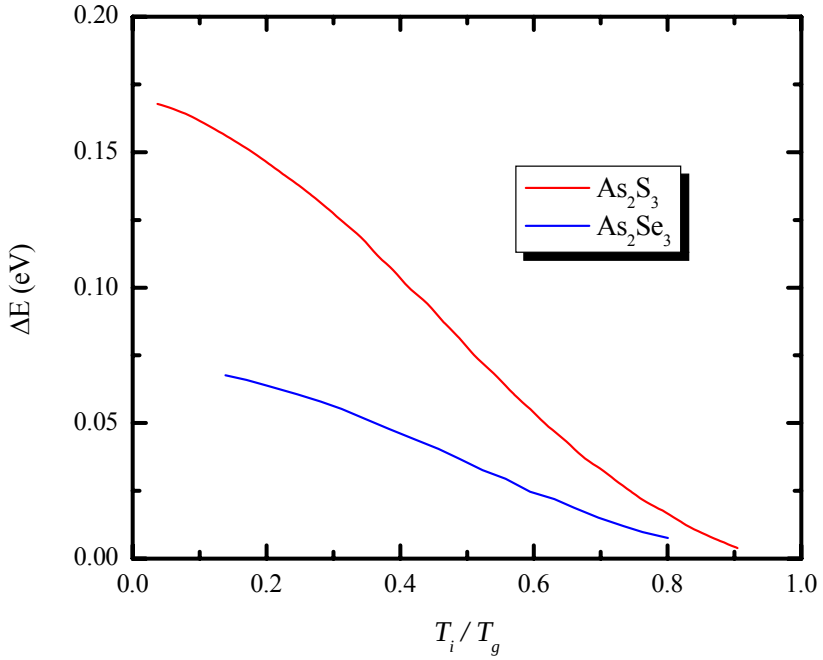

Figure 3-5: Temperature dependence of the photodarkening for As_2S_3 and As_2Se_3 glasses. The magnitudes, ΔE, of photodarkening versus of the ratio of illumination temperature, T_i to the glass transition temperature, T_g (Data extracted from [48]).

Tanaka also found that the absorption edge shift is not parallel at low temperatures, as shown in Figure 3-6. The black line is the spectral response of the absorption edge for an annealed As_2S_3 film at a temperature of 14 K. The blue line shows the spectral response of the absorption edge after photodarkening for this same sample and temperature to saturation. This extra shift in the absorption edge can be annealed out, red line, in two ways: (1) by warming the sample to room temperature, (2) by irradiating the sample with sub-bandgap light, $h\nu < E_g$. This indicates that there are at least two mechanisms responsible for photodarkening. The low temperature part, below room temperature, of photodarkening is probably due to the photoinduced creation of charged defects [40]. The above room temperature part could be caused by bond breaking and/or switching.

One of the most important characteristics of photodarkening is that only amorphous materials and not crystals display this effect. Although structural disorder is obviously not enough as photodarkening is only observed in amorphous materials that

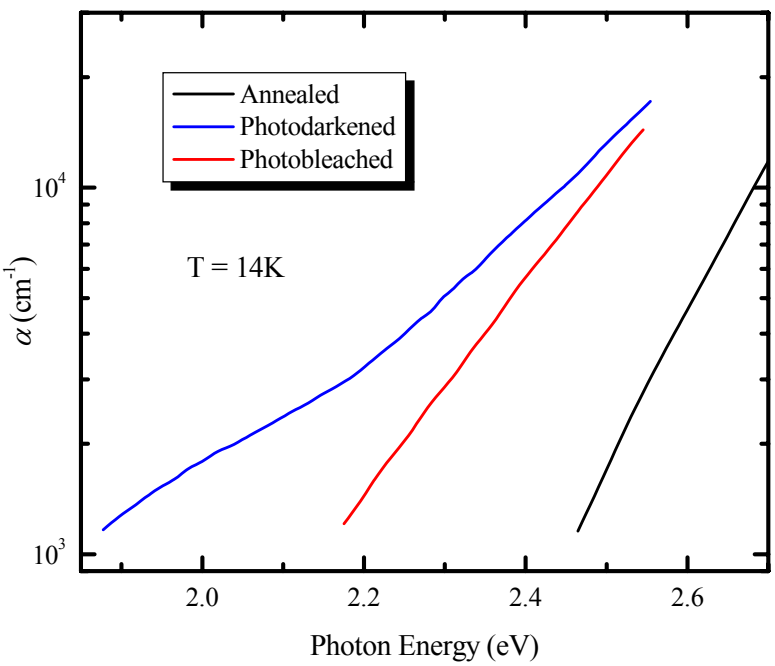

Figure 3-6: Absorption edge spectral response at 14 K for an amorphous As_2S_3 film. Black line is for the well annealed condition. Blue line is the photodarkened state induced by bandgap light. Red line is the photobleached state from the blue line, induced by sub-bandgap light ($h\nu < E_g$) (Data extracted from [40]).

contain chalcogenide elements. This fact suggests that the lone pair electrons of the chalcogenide atoms may have an essential role in the photoinduced effects. Further evidence to substantiate this proposition comes from Kolobov et al [49]. They used X-ray Photoemission Spectroscopy, XPS, measurements on a film of amorphous AsSe. A shift towards lower energies by 0.2 eV in the valence band was observed between annealed and photodarkened states, see Figure 3-7. As discussed in Section 2.2.1 the top of the valence band is mostly formed by lone pair electrons for the chalcogenide elements. Furthermore, this valence band edge shift is the same magnitude as the decrease in the optical gap, which confirms that it is the changes in the valence band and not the conduction band that is responsible for the photodarkening effect.

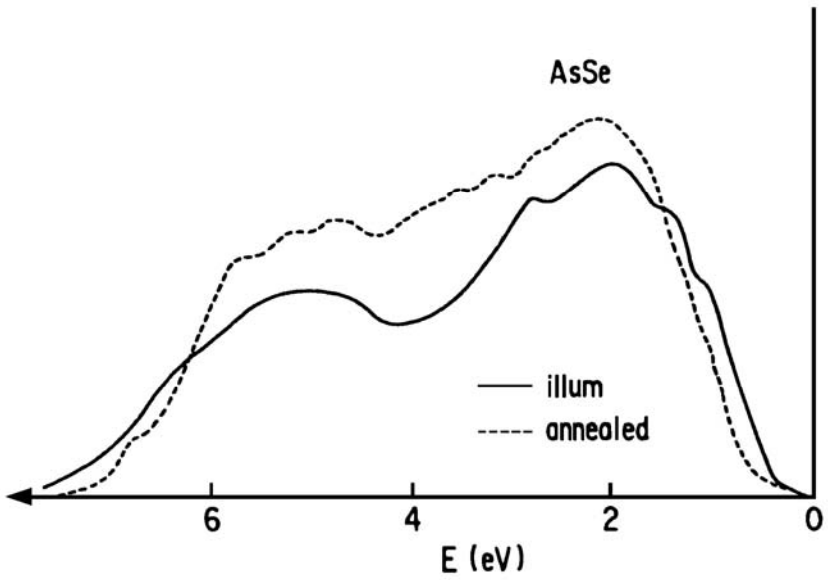

Figure 3-7: Reversible change in the density of states for the valence band of an amorphous As_2Se_3 film (From [40]).

3.3.2 Photoinduced Vectoral Effects

Photoinduced vectoral effects include changes due to the influence of polarization. These effects consist of any anisotropic property. A material is considered anisotropic if it exhibits different properties along different axes of propagation, such as dichroism and birefringence. Dichroism refers to the selective absorption for one of two orthogonal linearly polarized states of a light beam. There is a specific direction within these materials known as the optic or transmission axis. The electric field component of an incident light wave that is parallel to the transmission axis will pass through with relatively little attenuation, whereas light with polarizations in all other directions will be heavily attenuated, as depicted in Figure 3-8. A familiar example of a dichroic material is a polaroid film. Birefringence refers to the refractive index of the material. In that the refractive index that a propagating ray experiences is dependent on the state of polarization and the direction of the propagating beam. A consequence of birefringence is that any unpolarized light entering such a material is broken into two different rays with different polarizations and different propagating velocities. The result is a phase difference between two orthogonal polarizations as illustrated in Figure 3-9 (a). The exception is if the beam is along the optic axis. Such a situation results in

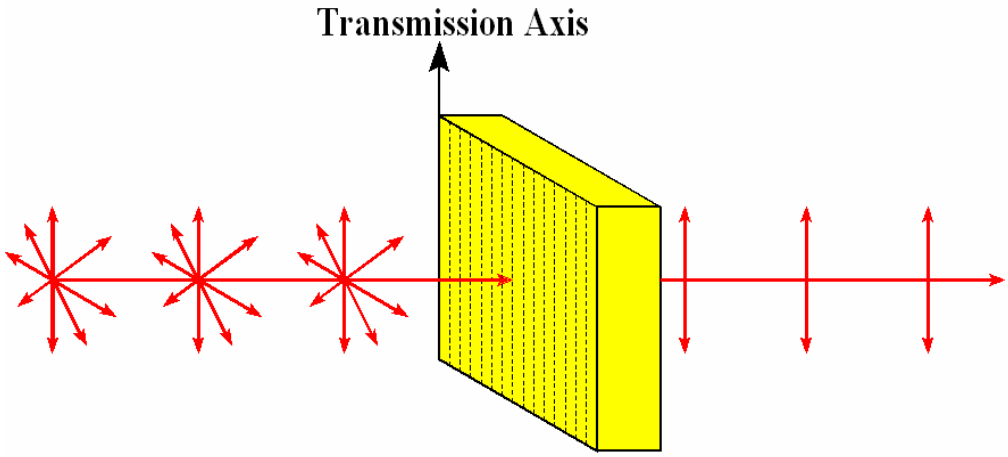

Figure 3-8: Dichroic material showing the absorption of light that is not polarized parallel to the transmission axis.

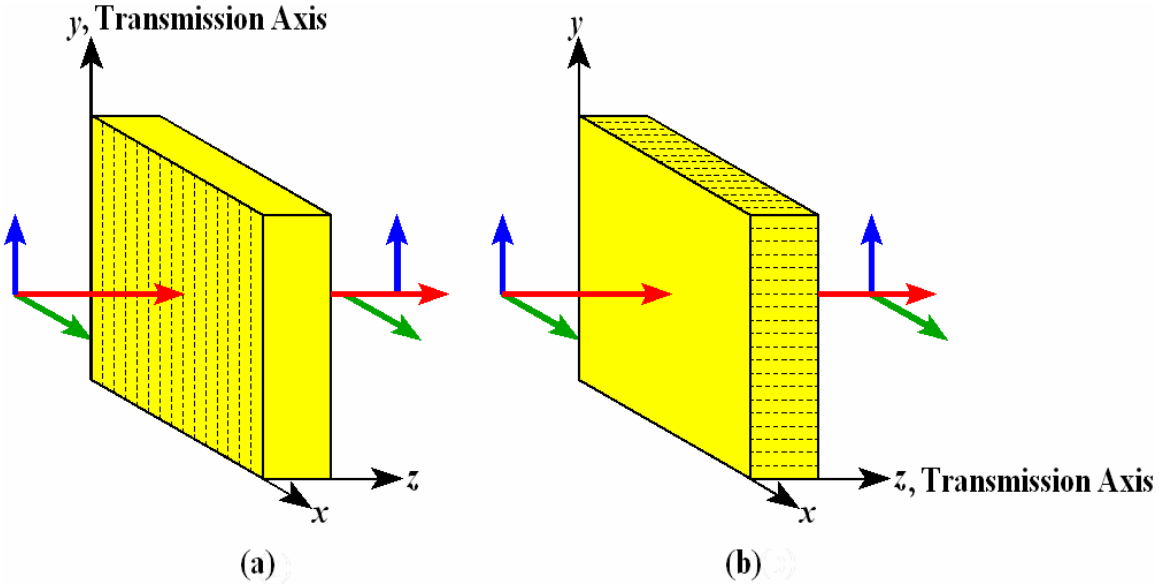

Figure 3-9: Birefringent material showing the propagation velocity difference (a) between two orthogonal waves and (b) no phase difference resulting for a ray along the transmission axis.

no phase change and the emerging beam is unchanged, Figure 3-9 (b). A good example of a birefringent material is a calcite crystal ($CaCO_3$).

Chalcogenide glasses are unique in that unlike most glasses which are isotropic (velocity of propagation within the material is the same regardless of direction) and homogenous. They start out isotropic but can be changed to anisotropic by an inducing light source, photoinduced anisotropy. One of the resulting effects is that a reversible dichroism can be induced in these materials, termed photoinduced dichroism, PDi. Another effect is photoinduced birefringence, PBi, and is correlated to photoinduced dichroism, In that when one is induced the other is also produced, much the same way that the scalar effects of photodarkening and photorefraction are related as explained in the previous section. Hence, photoinduced dichroism and birefringence are simultaneously induced. These effects are totally reversible in that the dichroism can be induced and subsequently annihilated and reoriented in the orthogonal direction as shown on the bottom of Figure 3-2. Such reorientation can be performed several hundred times without any sign of fatiguing [51].

Both dichroism and birefringence anisotropies can be induced by either linearly or circularly polarized light. In the case of circular anisotropies it is generally referred to as photoinduced gyrotropy [52]. It should also be noted that Fritzsche [53] predicted through his theoretical work that photoinduced anisotropy should be possible from an unpolarized beam through the sample. This theory was later tested and validated by Tikhomirov and Elliott [54]. However, in this case the anisotropy is between the direction of the inducing beam and perpendicular to the beam. Here the polarization of a perpendicular probe beam that is parallel to the direction of the inducing beam will experience greater absorption. The induced anisotropy is explained to occur not by dichroism of absorption but due to dichroism of scattering.

3.4 Existing Models

Since the discovery of photoinduced anisotropies by Zhandov et al. [12] over 25 years ago, there has been extensive research into understanding the structural elements responsible for these changes. To date there has been no clear consensus between the

different research groups on the microscopic mechanisms responsible for this phenomenon. This section introduces some of the more common models that have been presented to explain this effect.

To date all the models use microscopic mechanisms occurring at the atomic level to describe the measured macroscopic effect. The main problem for the lack of consensus between the different research groups is due to the fact that there is no method to directly measure these microscopic events. Most groups agree to the following basic description of the mechanism behind the photoinduced anisotropy phenomena. An inducing photon generates an electron hole pair that recombine non-radiatively. The local distortion of the lattice from the absorption of the phonon energy is dependent on the polarization of the inducing photon, along with some asymmetric structural units. This results in a change to the local bonding giving rise to a local anisotropy. The flexible lattice inherent to amorphous chalcogenides permits the local anisotropy to spread through the network resulting in the macroscopic photoinduced anisotropy effect.

The asymmetry of these local structural elements will have to be sensitive to the electric field of the inducing light polarization. Absorption would also be dependent on the parallel orientation of the photon polarization and the local elements optical axis. The local structural elements that most models use are intimate valence alternation pairs, IVAPs. As previously discussed in Section 2.3, these charged defects exist naturally in chalcogenide glasses. The idea of IVAPs being responsible for the photoinduced anisotropy mechanisms was first proposed in 1990 by Lyubin and Tikhomirov [55]. The idea was developed into a model based on a pnictogen, (eg. As) and chalcogen, (eg. Se) system by Elliot and Tikhomirov [56]. As shown in Figure 3-10 the model consists of a pyramidal structure formed by a pnictogen and three chalcogenide atoms that contain an IVAP. They proposed geminate recombination where an electron is expelled from a C_1^- (or a hole from C_3^+) and is trapped by a C_3^+ (or C_1^- respectively) of the same IVAP. This results in a transformation of the IVAP from $C_3^+C_1^-$ into $C_1^-C_3^+$. This progression is consistent with intensity dependence data that suggests typically a single

photon process is involved. Elliot and Tikhomirov suggest this to be a two step process; Where a single photon creates a singly and threefold coordinated neutral centers, $C_1^- C_3^+ + h\nu = C_1^0 C_3^0$. In the second step the neutral centers thermally decay back to the stable charged centers $C_1^- C_3^+$, Figure 3-10 (a) or $C_3^+ C_1^-$ (b). This results in a macroscopic change in the glass structure where the inducing light polarization is perpendicular to the IVAP lone pair orientation. This model also accounts for photoinduced gyrotropy (circular polarization) since mirror images of the pyramidal structures have opposite magnetic dipole moments for optical transitions.

To explain the temperature effects of photoinduced anisotropy Tikhomirov, Adriaenssens and Elliott [57] developed a similar model that was also based on VAPs. This model is shown in Figure 3-11 and uses the bonding structure of an elemental

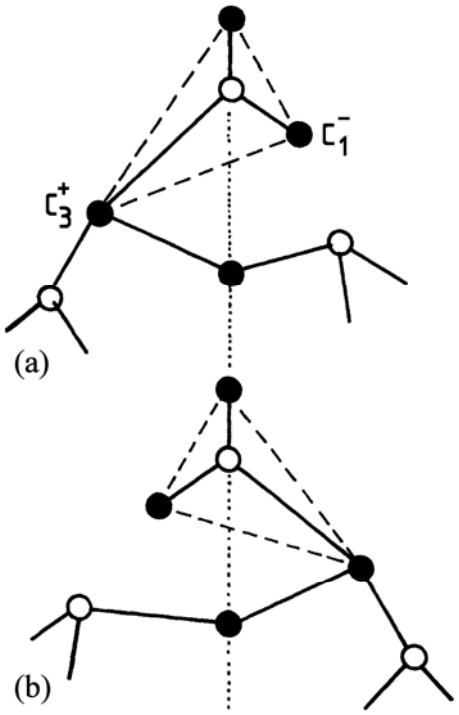

Figure 3-10: Schematic illustration of the model proposed to be responsible for photoinduced anisotropy in a pnictogen-chalcogenide system. (a) before excitation and (b) after. The open circles denote pnictogen atoms and the solid circles the chalcogen atoms. Note that they exaggerated the extension of the C_3^+ bond for clarity (From [56]).

chalcogenide material, but it can be easily extended to a pnictogen-chalcogenide system such as the compound we used (As_2Se_3) by placing an As on the C_2^0 positions. In order to produce a flip in the pyramidal structure an electron is optically excited from the C_1^- atom and subsequently trapped in an antibonding orbital localized around the C_3^+ atom. This is shown as a dotted circle around the C_3^0 atom in Figure 3-11 (b). They go on to say that this produces a flexible transient pyramid state consisting of $C_3^0C_1^0C_2^0C_2^0$ atoms because: (1) the antibonding electron weakens the bonds of the C_3^0 atom, (2) the C_1^0 atom has only one (weakened) bond and no electrostatic forces like in the $C_3^+C_1^-$ case, and (3) a void should exist near to the C_1^- atom before excitation to account for its single fold coordination. From this transient excited state, thermal energy can cause the pyramid to flip resulting in the C_3^0 atom to move to the mirror image position C_{3m}^0 in (b). To maintain the lowest possible energy state the $C_1^0C_{3m}^0$ pair would de-excite to the arrangement shown in (c). To account for low temperatures the C_3^0 atom has the possibility to tunnel through the $C_2^0C_1^0C_2^0$ plane, shaded region on Figure 3-11 (b), to the mirror image position C_{3m}^0 and subsequently de-excite to (c). In this case Figure 3-11

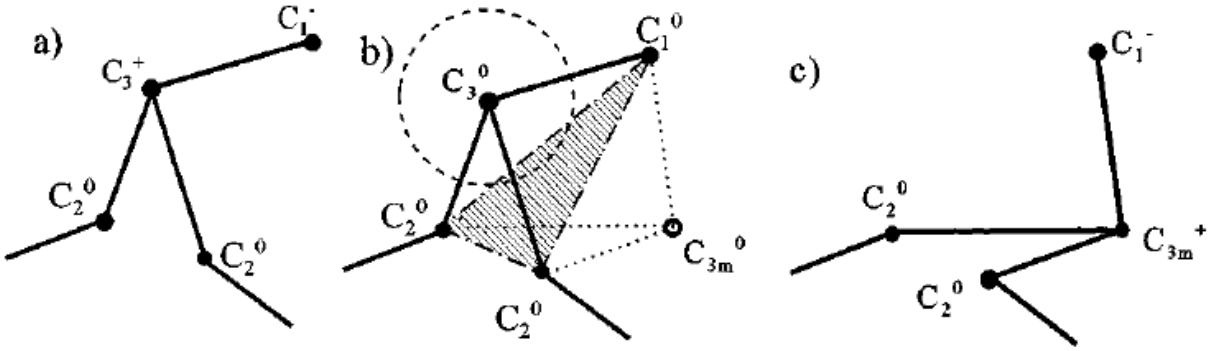

Figure 3-11: Proposed anisotropy model with IVAP centered at C_3^+. (a) Configuration before optical excitation, (b) transient configuration after optical excitation and (c) reoriented metastable IVAP configuration (From [57]).

(c) represents an IVAP bond that is orthogonal to polarization of the inducing light. In doing so this minimizes the energy between the IVAP dipole and the electric field of the inducing beam.

In the model that Fritzsche proposes [53, 58, 59] he uses the concept of anisotropic microvolumes to explain a variety of photoinduced anisotropies in chalcogenide glasses. This model not only accounts for the sign of anisotropy but also predicted that even an unpolarized light beam could cause optical anisotropy in these materials. This prediction was later confirmed experimentally by Tikhomirov and Elliott [54]. It should be noted that the microvolumes Fritzsche uses are still based on IVAPs [53, 58] but he also states that they are not the only anisotropic entities. He notes that all optical transitions, interband, Urbach tail and defect transitions, are polarization dependent. He also stresses that there is no lower threshold of light intensity for producing photoinduced anisotropic effects as the action of the light is cumulative.

Fritzsche grouped the anisotropic microvolumes into three categories v_{ix}, v_{jy} and v_{kz}. The reason behind this was to represent the three directions, x, y and z, that would have the largest cross sectional absorption for the inducing light polarizations. He separately summed the three microvolumes belonging to each category to obtain the average absorption coefficients of each direction.

$$\bar{\alpha}_x \approx \sum_{i=1}^{N_x} \frac{\alpha_{ix} v_{ix}}{V_{\text{tot}}},\ \bar{\alpha}_y \approx \sum_{i=1}^{N_y} \frac{\alpha_{jy} v_{jy}}{V_{\text{tot}}} \text{ and } \bar{\alpha}_z \approx \sum_{i=1}^{N_z} \frac{\alpha_{kz} v_{kz}}{V_{\text{tot}}} \tag{3.1}$$

where N_x is the number of microvolumes of v_{ix} type, α_{ix} is the absorption coefficient for light polarized along the x-axis and V_{tot} is the total volume of the material. Approximately equal symbols are used because he neglects the small contributions for example to $\bar{\alpha}_x$ from absorption in the v_{jy} and v_{kz} microvolumes. Since the glass is initially isotropic this means that

$$\bar{\alpha}_x \approx \bar{\alpha}_y \approx \bar{\alpha}_z \tag{3.2}$$

The smaller the anisotropic microvolumes that are chosen, then the more accurate

equations (3.1) and (3.2) will be. For simplicity Fritzsche chose a volume equal to the bandgap. Keeping with the initially isotropic material demands that

$$N_x = N_y = N_z = \frac{1}{3}N \tag{3.3}$$

where N is the total number of anisotropic microvolumes.

After the absorption of bandgap light the following processes can take place: (a) there is a redistribution with no net change, $\Delta N_x + \Delta N_y + \Delta N_z = 0$, (b) bleaching, $\Delta N < 0$, (c) creation, $\Delta N > 0$, or (d) electron and hole diffusion.

If we assume a light wave traveling in the *y* direction, linearly polarization along the *z*-axis as illustrated in Figure 3-12 (a). Then an absorption process will take place in the *vkz* element. There are two possible outcomes from a local structural change due to recombination can take place. Either the anisotropy of the microvolume will change or it will be left intact. The former is the only interesting one of the two and results in a loss of that particular absorption element for the *z* polarization. Now either bleaching took place or the anisotropy was altered so that only *x* and *y* polarization are absorbed. This latter instance leads to a redistribution of the microvolumes such that $-\Delta N_z = \Delta N_x + \Delta N_y$. The collective effect of these redistribution events results in a reduced absorption for light polarized parallel to the inducing light polarization and an equally increased absorption of the two orthogonal directions, $-\Delta\alpha_z = \Delta\alpha_x + \Delta\alpha_y$. The dielectric tensor is then an ellipsoid of revolution with the optical axis in the *z* direction. The resulting absorption coefficients are $\alpha_z < \alpha_x = \alpha_y$ and refractive indices $n_z < n_x = n_y$ as shown in Figure 3-12 (a).

The prediction of unpolarized light producing optical anisotropy is illustrated in Figure 3-12 (b). An unpolarized inducing light source traveling in the *y* direction yields absorption only in the microvolumes corresponding to *x* and *z* polarizations. The outcome of the redistribution is then a decrease in absorption for *x* and *z* polarizations and an increase for the *y* polarization. The dielectric tensor in this case is an ellipsoid of

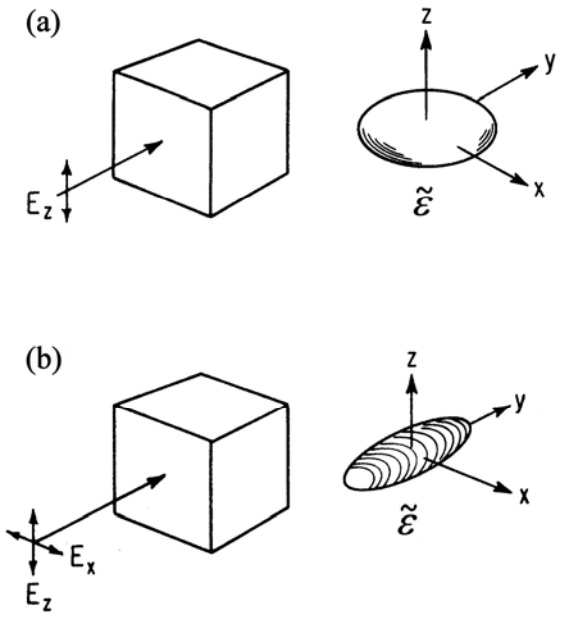

Figure 3-12: Schematic illustration of Fritzsche model for photoinduced anisotropy in chalcogenide glasses. Shows the dielectric tensor $\tilde{\varepsilon}$ after irradiation (a) to linearly polarized light and (b) to unpolarized light (From [59]).

revolution with the axis in the direction of propagation. i.e. The *y* direction for the example in Figure 3-12 (b), where the absorption coefficients become $\alpha_z = \alpha_x < \alpha_y$ and the refractive indices $n_z = n_x < n_y$. This was later experimentally confirmed by Tikhomirov and Elliott [54]. Their results showed that the glass appeared isotropic for light traveling along the propagation path (*y* axis for Figure 3-12 (b)) of the inducing beam, but the anisotropy was observed with polarized light propagating in either of the orthogonal directions (*x* or *z* axis for Figure 3-12 (b)).

3.5 Summary

This chapter presented aspects of metastable photoinduced changes that can occur in chalcogenide glasses. In particular the distinction between what a reversible and irreversible effect is, as well as scalar and vectoral differences were discussed. An introduction to the scalar effects of photodarkening, photobleaching and photorefraction as well as the vectoral effects of photoinduced dichroism and birefringence were talked about. The chapter ended with a discussion on existing models that are used to explain these effects.

Chapter 4

Experimental Apparatus and Procedure

4.1 Introduction

A complete description of the equipment used in the measurement of photoinduced dichroism will be presented in this chapter. First a detailed preparation procedure of the As_2Se_3 thin film samples is explained. Then a general description of the anisotropy measurement system is introduced. This is followed by a detailed description of the various components of the experimental apparatus.

4.2 Substrate Preparation

Corning 7059 glass was the substrate used for depositing thin films of As_2Se_3. Preparation of the substrate involves a cleaning procedure, which removes any unwanted particles and impurities that maybe on the glass surface.

The beaker and rack, which holds the substrates, are cleaned and rinsed in an ultrasonic cleaner using extran MN-1 powder detergent dissolved in deionized water. The glass slides are then placed in the rack inside the beaker washed/rinsed for 4 cycles in the ultrasonic cleaning bath using the extran MN-1 powder detergent in deionized water. After removing the substrates from the bath, the slides were blown dry with high purity filtered air. Complete drying is achieved by baking the substrates overnight in an oven at 105 °C.

It has been determined that 4 wash and rinse cycles produce optimum cleaning results. Any more and the benefits do not have a significant improvement, any less and the substrate resistance decreases, indicating there are impurities present.

4.2.1 Vacuum Deposition System

The source material used for depositing the thin films were high purity, near-stoichiometric composition of amorphous arsenic tri-selenide, As_2Se_3, pellets. These pellets were electronic grade liquid quenched vitreous As_2Se_3, 36.6 wt. % arsenic or 37.8 at. %, obtained from Noranda Advanced Materials, Saint Leuvent, Quebec, Canada. The sample composition was lightly As deficient from stoichiometry. The

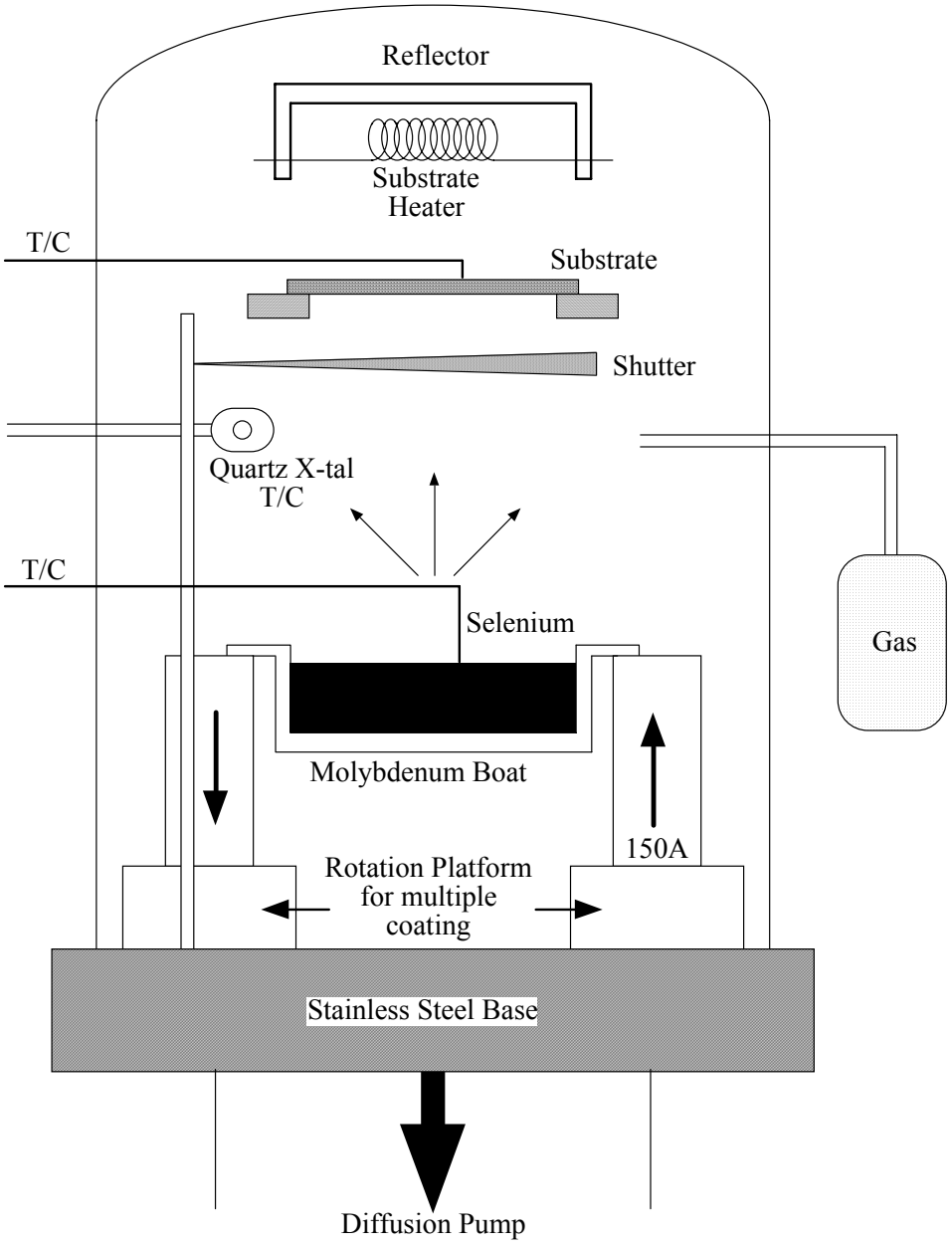

Figure 4-1: Schematic diagram of the vacuum deposition system.

supplier used optical emission spectroscopy to verify the chemical content, composition and purity of the amorphous pellets.

The amorphous thin films were fabricated using a conventional vacuum deposition system. As_2Se_3 pellets were evaporated from a heated boat in an NRC 3117 thermal vacuum deposition system, illustrated in Figure 4-1. A mechanical vacuum pump was first used to evacuate the chamber followed by a diffusion pump to achieve a high vacuum of $\approx 10^{-6}$ Torr. The As_2Se_3 pellets were contained in a molybdenum boat and melted by passing a large ac current, e.g. 100 amperes, through the boat. The boat temperature during evaporation was approximately 360 °C, which resulted in a deposition rate of 28 nm/minute. The glass substrate was maintained at "room temperature", about 24 °C. Thermocouples were used to monitor both the boat and substrate temperatures. Once the material in the boat was totally evaporated the boat current and diffusion pump were switched off. Then the system slowly cooled under vacuum for about 1 hour at which time the mechanical pump was switched off and the films allowed to relax.

4.3 Anisotropy Measurement Apparatus

A schematic diagram of the experimental setup used for the photoinduced dichroism measurements is shown in Figure 4-2 where the anisotropy was induced using a linearly polarized HeNe laser (operating at 632.8 nm). This inducing laser beam was expanded from an initial waist beam of 1.1 mm (FWHM) to approximately 3.4 mm by way of an ordinary convex lens to ensure that the entire probe spot area was being irradiated. A variable neutral density filter was employed to facilitate a means to adjust the pump beam intensity level. Monitoring of the pump intensity was achieved by using a simple glass microscope slide as a partial reflector. The reflected sample of the pump beam was measured using the pump power photodetector connected to the AUX #2 A/D converter in the lock-in amplifier. The ratio of reflected (sampled) to inline inducing intensity was measured to be 37%. The inducing laser beam then passed through a calibrated polarizer that could be adjusted between two orthogonal directions. The unpolarized probe source consisted of an array of red LEDs (666 nm) shining through a

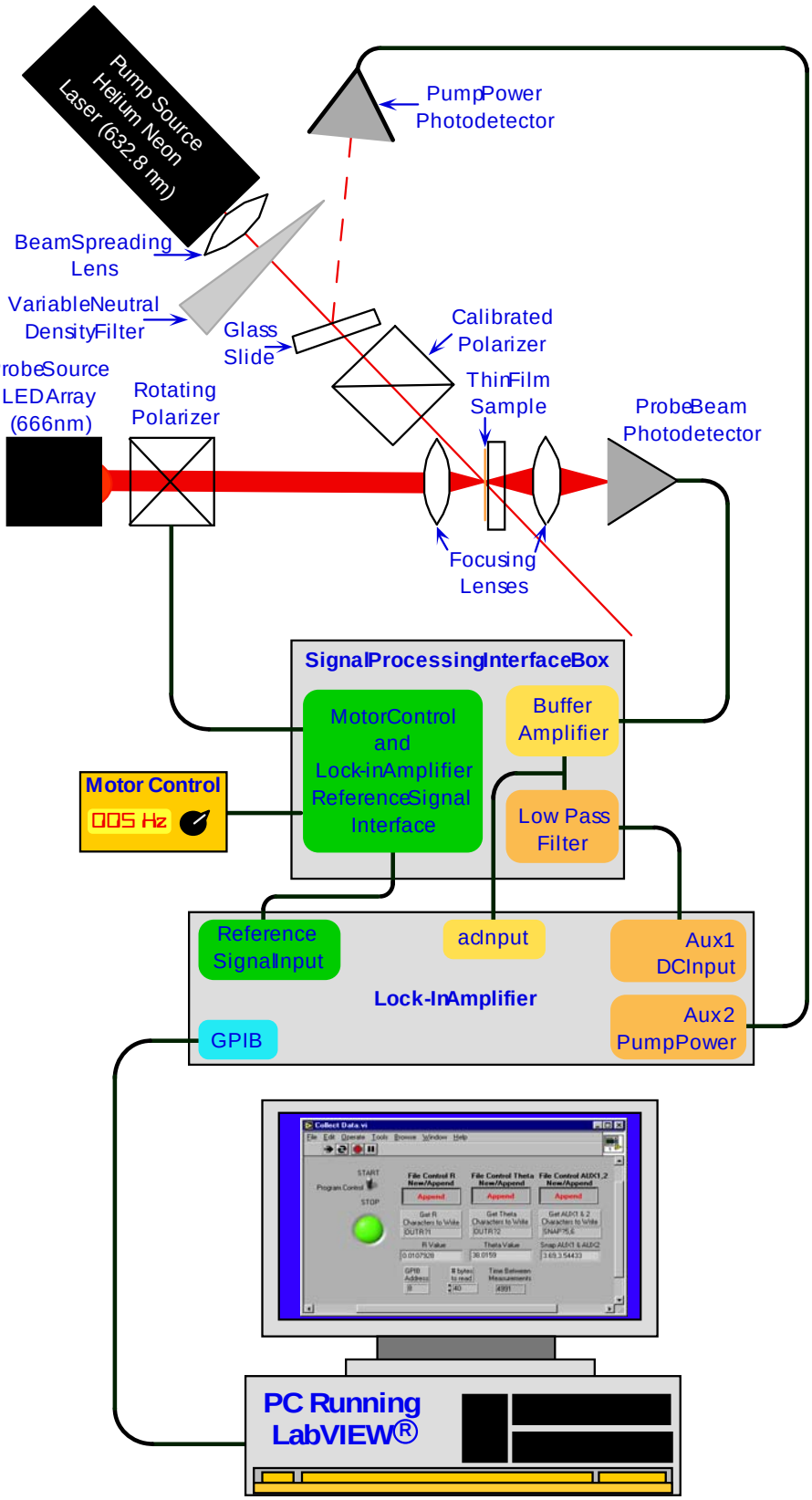

Figure 4-2: Schematic diagram of the experimental apparatus.

piece of frosted glass. The probe beam passed through a polarizer, which was rotating at about 5 Hz and then focused to a spot size of approximately 1.70 mm in diameter onto the sample. In essence, the probe beam incident on the sample was a linearly polarized light beam with the polarization direction rotating at 5 Hz, which is called the fundamental frequency, *f*. The transmitted probe light was then focused onto a photodiode detector. The resulting electrical signal had 2 destinations: (a) to the lock-in amplifier via a buffer amplifier in the signal processor interface box to measure the 2nd harmonic, 2*f* portion of the signal. (b) through a low pass filter in the signal processor interface box to the AUX #1 A/D converter in the lock-in amplifier to measure the average or DC portion of the signal. The reference signal at frequency *f* for the lock-in amplifier was supplied by an optical sensor on the rotating analyzer. A computer running a LabVIEW® program recorded the lock-in amplifier readings every 5 seconds via a GPIB connection.

4.3.1 Probe Light Source

The ideal probe light for this apparatus is a completely unpolarized source, as any source polarization would have to be extracted from the measurements of the photoinduced dichroism of the sample. Producing a completely unpolarized source proved to be very difficult as we tried several sources; halogen lamp, incandescent bulb with a straight tungsten filament powered from a DC source, different types of light emitting diodes (LEDs) and even producing circularly polarized light from a linearly

(a) (b)

Figure 4-3: a) Probe light in housing with frosted glass in place. b) Probe light LED array.

polarized laser through a ¼ wave plate, all of which had varying degrees of polarization. The best probe source we found was produced by an array of nineteen red LEDs ($\lambda \cong 666$ nm) shinning through frosted glass, see Figure 4-3. This produced a light source with only approximately 0.95 % polarization.

The emission line shape of the LED array was measured with an Oriel Instruments, Cornerstone 130™ motorized 1/8m monochromator, model number 74000 and model number 70348 InGaAs cooled detector head with transimpedance amplifier. The results of this measurement are plotted in Figure 4-4 and as the chart indicates the central wavelength, λ, is approximately 666 nm.

The intensity of the probe source incident on the sample was determined by measuring the photocurrent (I_{Ph}) with a Hamamatsu S1336-8BK photodiode placed at the sample location. From the data sheets, the responsivity (R) of the photodiode was found to be about 354.6 mA/W at the wavelength of interest. Using the previously determined central wavelength of the LED array, the power of the probe source incident

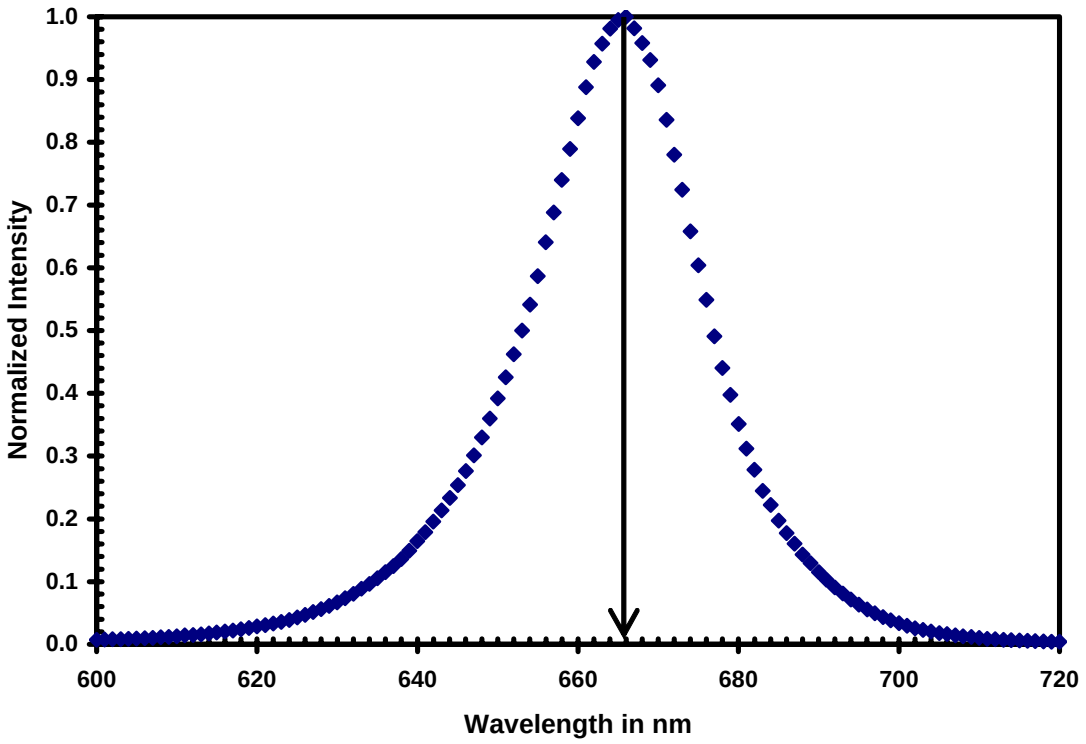

Figure 4-4: LED array (probe source) emission spectrum showing the central wavelength, λ.

on the sample could be determined as follows

$$P_{op} = \frac{I_{Ph}}{R} = \frac{14.61\mu A}{354.6\,^{mA}/_{W}} = 41.201\ \mu W \tag{4.1}$$

The probe source made a circular spot on the sample with a diameter of approximately 1.70 mm. Therefore the area was

$$A = \frac{\pi d^2}{4} = \frac{\pi 1.70^2 mm}{4} \cong 2.27 mm^2 \tag{4.2}$$

This yields a probe source intensity of

$$I = \frac{P_{op}}{A} = \frac{41.201\mu W}{2.27 mm^2} \cong 18.2\ \mu W\ mm^{-2} \tag{4.3}$$

The above was the intensity of the probe beam at the sample surface. To determine the intensity in the sample we had to find the transmittance, T, and since the probe beam was normal to the sample [50]

$$T = 1 - \left(\frac{n_2 - n_1}{n_2 + n_1} \right)^2 \tag{4.4}$$

where n_1 and n_2 in our case are the refractive indices of air and As_2Se_3 respectively. The refractive index of As_2Se_3 at this wavelength was determined from [61] by using

$$n^2_{(\lambda)} = 7.8605 \times 10^{-13} \lambda^{-2} + 7.1308 \tag{4.5}$$

which gives

$$n_{(666nm)} = \sqrt{\frac{7.8605 \times 10^{-13}}{\left(666 \times 10^{-9} m\right)^2} + 7.1308} \cong 2.984$$

Using equation (4.4), the percentage of probe beam intensity transmitted into the sample was

$$T = 1 - \left(\frac{2.984 - 1}{2.984 + 1} \right)^2 \cong 75.2\%$$

Therefore the intensity of probe beam available for the sample to alter was

$$I_T = T\,I = 75.2\% \times 24.6\ \mu W\ mm^{-2} \cong 13.6\ \mu W\ mm^{-2}$$

As the following section will show this was more than 5 times less than the lowest inducing light intensity used. The probe beam therefore had no measurable effect on the sample.

4.3.2 Inducing Light Source

The inducing light source used in the experiment was a 30 mW (maximum) linearly polarized Helium Neon (HeNe) laser model number 31-2082-000, manufactured by Coherent Inc. There are three criteria for the inducing or excitation light source:

(a) The excitation intensity must be of sufficient intensity that it can photoinduce the material within a reasonable time frame.

(b)The excitation intensity should be strong enough that the probe beam has negligible effects on the material. The lowest intensity used as an inducing light source in this experiment was 76 $\mu W/mm^2$. At this intensity a photoinduced measurement cycle lasted for 2 hours and as the previous section showed this level of source intensity was more than 5 times greater than the probe beam intensity.

(c)The excitation wavelength, λ, must be such that the pump-beam can be sufficiently absorbed by the material. This means that the source used must be within

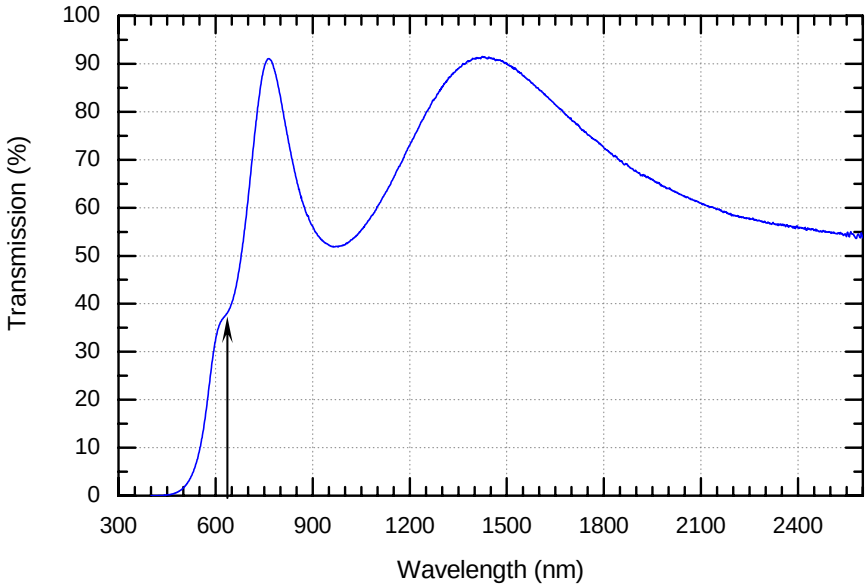

Figure 4-5: Spectral Response of an As_2Se_3 thin film sample, 0.25 µm thick.

the absorption edge of the material. The wavelength of the HeNe laser is 632.8 nm and, as the spectral response of the As_2Se_3 0.25 μm sample shows in Figure 4-5 this is on the absorption edge and therefore an ideal wavelength for the inducing source.

The intensity of the HeNe laser was determined by first mapping the beam profile for both the vertical as well as the horizontal polarization states. This was accomplished by mounting a photodiode (Hamamatsu S1223 Si PIN photodiode) behind a 25 μm pinhole that was in turn mounted in an *x*–*y* micrometer positioner and placed normal to the HeNe laser's beam path. Measurements were recorded in both the *x* and *y* directions through the maximum at increments of 0.05 mm. This data was used to fit the beam to a Gaussian profile, Figure 4-6 using a curve fitting program in MatLab, see 'Gaussian_Fit.m' program in Appendix A. The MatLab Gaussian fit program determined that σ = 0.550 mm for the vertical polarization and σ = 0.535 mm for the horizontal polarization of the inducing Helium Neon laser beam.

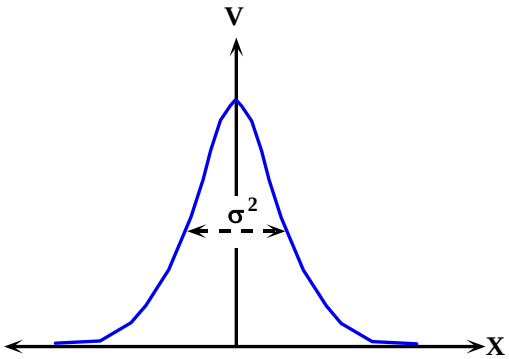

Figure 4-6: Gaussian profile

$$V = V_o \int e^{\frac{-x^2}{2\sigma^2}} dx \tag{4.6}$$

The beam profile is measured in 2 dimensions, horizontal and vertical (*x* and *y*).

$$I = I_o e^{\frac{-\left(x^2+y^2\right)}{2\sigma^2}} \tag{4.7}$$

In order to determine the power (P_{op}) the intensity must be integrated from -∞ to ∞ for both the *x* and *y* coordinates.

$$P_{op} = I_o \int_{-\infty}^{\infty}\int_{-\infty}^{\infty} e^{\frac{-\left(x^2+y^2\right)}{2\sigma^2}} dxdy \tag{4.8}$$

Equation (4.8) can be simplified by changing the Cartesian coordinates to polar coordinates.

$$P_{op} = I_o \int_0^{\infty} \int_0^{2\pi} e^{\frac{-\rho^2}{2\sigma^2}} \rho d\rho d\theta \tag{4.9}$$

Substituting $\xi = \rho^2$ and therefore $d\xi = 2\rho d\rho$ gives

$$P_{op} = I_o \int_0^{\infty} \int_0^{2\pi} e^{\frac{-\xi}{2\sigma^2}} \frac{d\xi}{2} d\theta \tag{4.10}$$

Performing the above integration yields

$$I_o \left(\frac{2\sigma^2 e^{\frac{-\xi}{2\sigma^2}}}{2} \right) 2\pi \Bigg|_{\substack{\xi = \infty \Rightarrow 0 \\ \xi = 0 \Rightarrow I_o 2\pi\sigma^2 = P_{op}}} \tag{4.11}$$

Hence, the intensity can be found from

$$I_o = \frac{P_{op}}{2\pi\sigma^2} \tag{4.12}$$

From equation (4.12) the intensity of the inducing beam at the surface of the sample can be determined but we need to find the intensity that is transmitted into the sample and is therefore available for affecting a change. Since the inducing beam is not normal to the sample surface but rather at an angle somewhat complicates the mathematics. The angle of incidence was measured to be approximately 32.4°. This angle was determined by triangulation as shown in Figure 4-7. All three sides of the triangle were measured as a self check of the measurement accuracy.

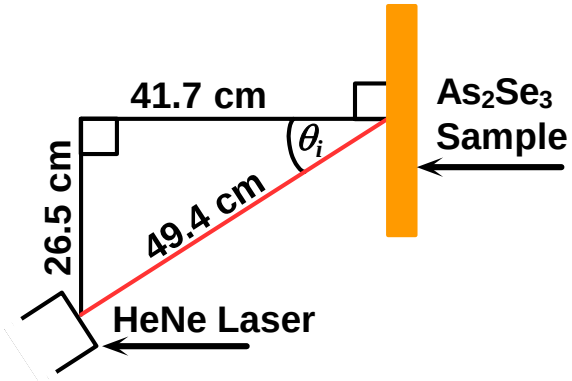

Measurement check

$$\sqrt{26.5^2 + 41.7^2}\,\text{cm} = 49.41\ \text{cm}$$

$$\theta_i = \sin^{-1}\left(\frac{26.5\text{cm}}{49.4\text{cm}}\right) \cong 32.4°$$

Figure 4-7: Determination of the pump beam's angle of incidence with sample.

The transmittance, T, is dependent on the refractive index, which in turn is a function of wavelength, λ. The refractive index of As_2Se_3 at a wavelength of 632.8 nm can be determined from [61]

$$n^2_{(\lambda)} = 7.8605\times10^{-13}\lambda^{-2} + 7.1308 \tag{4.13}$$

$$n_{(632.8\text{nm})} = \sqrt{\frac{7.8605\times10^{-13}}{\left(632.8\times10^{-9}\,\text{m}\right)^2} + 7.1308} \cong 3.016$$

To determine the reflectance, R, or transmittance, T, one must refer to Fresnel's equations [50] for the reflection and transmission coefficients that relate the transmitted and reflected amplitudes of an electromagnetic wave traveling from one medium, of refractive index n_1, into another medium with refractive index n_2. These coefficients also depend on the electric field direction (polarization orientation). Referring to Figure 4-8 where an incident light wave traveling from a less dense medium n_1 to a medium of

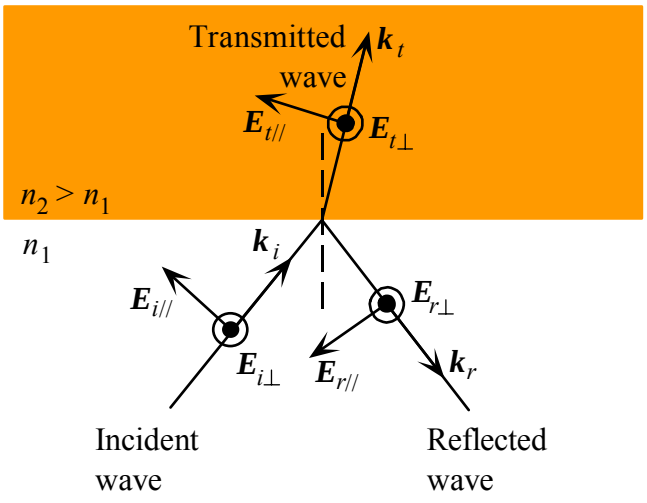

Figure 4-8: Light wave traveling from a less dense medium into a more dense medium ($n_1 < n_2$). Modified diagram from "Optoelectronics and Photonics Principles and Practices," S.O. Kasap, Prentice Hall, 2001, Figure 1.11.

greater density n_2 is depicted. Note that the plane of incidence for this light wave is the plane of the paper but perpendicular to the boundary of the two media. The electric field direction of the two polarization states (horizontal, $\boldsymbol{E}_{//}$, and vertical, $\boldsymbol{E}_{\perp}$) are orthogonal to the direction of propagation as well as each other.

Because we have the polarization states orientated parallel (horizontal polarization) and perpendicular (vertical polarization) to the plane of incidence means that the reflectance and transmittance will be different for the two states. For the two polarization states the reflection coefficients are [50]

$$r_{//} = \frac{\sqrt{n^2 - \sin^2(\theta_i)} - n^2 \cos(\theta_i)}{\sqrt{n^2 - \sin^2(\theta_i)} + n^2 \cos(\theta_i)} \tag{4.14}$$

and

$$r_{\perp} = \frac{\cos(\theta_i) - \sqrt{n^2 - \sin^2(\theta_i)}}{\cos(\theta_i) + \sqrt{n^2 - \sin^2(\theta_i)}} \tag{4.15}$$

where $n = \frac{n_2}{n_1}$.

The reflectances (R_{HP} and R_{VP}) are defined as

$$R_{HP} = |r_{//}|^2 \tag{4.16}$$

and

$$R_{VP} = |r_{\perp}|^2 \tag{4.17}$$

Since the transmittance and reflectance must sum to unity then

$$T_{HP} = 1 - R_{HP} = 1 - |r_{//}|^2 = 1 - \left| \frac{\sqrt{n^2 - \sin^2(\theta_i)} - n^2 \cos(\theta_i)}{\sqrt{n^2 - \sin^2(\theta_i)} + n^2 \cos(\theta_i)} \right|^2 \tag{4.18}$$

and

$$T_{VP} = 1 - R_{VP} = 1 - |r_{\perp}|^2 = 1 - \left| \frac{\cos(\theta_i) - \sqrt{n^2 - \sin^2(\theta_i)}}{\cos(\theta_i) - \sqrt{n^2 + \sin^2(\theta_i)}} \right|^2 \tag{4.19}$$

where T_{HP} and T_{VP} are the transmittance for horizontal and vertical polarizations respectively. Substituting $n_1 = 1$ (refractive index for air) and the previously determined values for $n_2 = n_{(632.8\ nm)} = 3.016$ (refractive index for As_2Se_3 at a wavelength of 632.8 nm) and the angle of incidence $\theta_i = 32.4°$ yields the following transmittances

$$T_{HP} = 1 - \left| \frac{\sqrt{3.016^2 - \sin^2(32.4°)} - 3.016^2 \cos(32.4°)}{\sqrt{3.016^2 - \sin^2(32.4°)} + 3.016^2 \cos(32.4°)} \right|^2 = 80.42\%$$

and

$$T_{VP} = 1 - \left| \frac{\cos(32.4°) - \sqrt{3.016^2 - \sin^2(32.4°)}}{\cos(32.4°) + \sqrt{3.016^2 - \sin^2(32.4°)}} \right|^2 = 68.97\%$$

These results indicate that there is a significant difference for the transmitted pump intensity between the vertical and horizontal polarization states. This helps for the comparison of photoinduced effects verses intensity but also means that we have had to double the number of cycles measured in order to obtain a decent set of accurate parameters from a small statistical sample number. Typically we measured 12 anisotropy buildup cycles, 6 with a vertically polarized pump beam and 6 where the pump beam was horizontally polarized.

4.3.3 Rotating Analyzer

The rotating analyzer was constructed in the machine shop because a unit that rotated fast enough, e.g. 300 rotations per minute, RPM, was not commercially available. Pictures of the rotating analyzer are shown in Figure 4-9. The analyzer housing was rotated by means of an O-ring belt driven by a DC motor, made by Escap, model number D21.213E.B2X2. Speed control for the DC motor was provided by an Oriel chopper controller via the signal processing interface box. Rotational feedback to the chopper controller as well as a reference pulse for the lock-in amplifier was provided by an Omron EE-SF5 reflective phototransistor and a piece of silver tape on the rotating cylindrical housing.

This rotating analyzer can rotate from 60 RPM to 600 RPM. The lower limit is determined by the chopper controller as the display precision is in whole numbers. i.e. 1 Hz is the lowest frequency displayed. The upper limit is restricted by the O-ring belt drive as it starts to slip on the motor pulley causing the lock-in amplifier to loose the phase lock with the reference signal at rotations greater than 600 RPM.

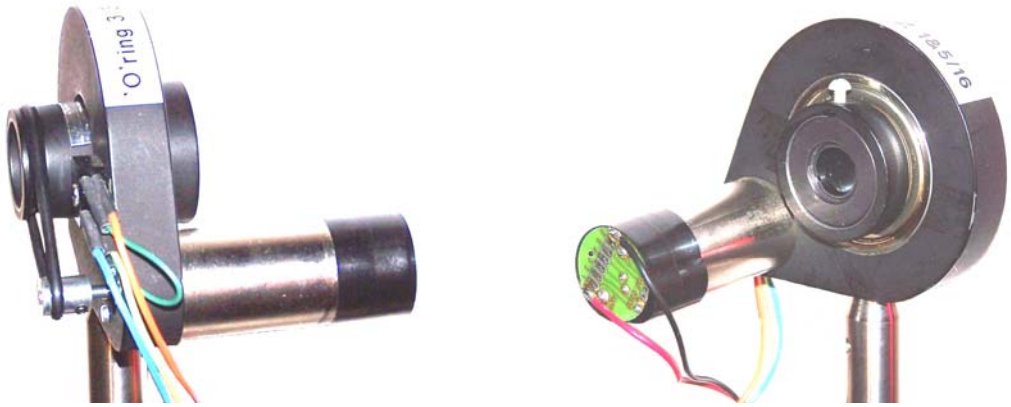

(a) (b)

Figure 4-9: Rotating analyzer showing O-ring belt drive along with phototransistor for reference signal pulse (a) and polarizer mount (b).

4.3.4 Photodetector

There were two different detectors used in the present experimental set-up, one for measuring the probe beam and the other for monitoring the inducing light power level. The probe beam detector was a silicon photodiode with a borosilicate glass window and an effective area of 33 mm^2, Hamamatsu number S1336-8BK. The pump-beam power level monitoring detector was a silicon PIN photodiode with a borosilicate glass window and an effective area of 6.6 mm^2, Hamamatsu number S1223-01. Both detectors are housed in a small die cast aluminum case that has been spray painted black to reduce reflections. As shown in Figure 4-10 the photodiodes are reversed biased with a DC supply and the photo current, I_{Ph}, is measured by way of V_{out} across the selectable sensing resistor. Table 4.1 lists the measured sensing resistor values used for each detector. The resistors were measured using a GenRad Digibridge, model number 1657-9700, which has an accuracy of 0.2%.

Since the measurements that we are interested in deal with measuring a changing polarization state it was necessary to check that the photodiodes were isotropic and therefore not inducing some polarization to the measured signal. To check this we simply measured and recorded the probe beam magnitude and phase, then rotated the detectors 90° and compared the resulting magnitude and phase with the previously

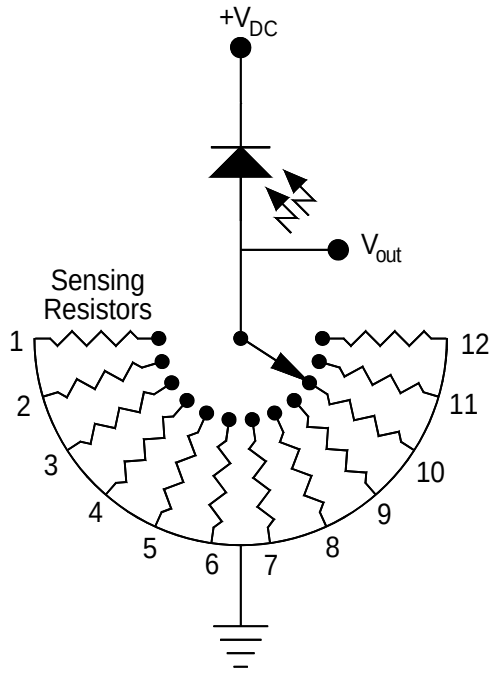

Figure 4-10: Schematic diagram of photo detector circuit.

Table 4- 1: Measured sensing resistor values for the photo detectors.

Sensing Resistor Number	Detector S1336-8BK Sensing Resistor Value	Detector S1223 Sensing Resistor Value
1	1003 Ω	1001 Ω
2	1999 Ω	1998 Ω
3	5010 Ω	5000 Ω
4	9980 Ω	9950 Ω
5	19980 Ω	19980 Ω
6	49800 Ω	49900 Ω
7	99900 Ω	99900 Ω
8	199900 Ω	201000 Ω
9	498000 Ω	502000 Ω
10	999000 Ω	998000 Ω
11	1993000 Ω	2130000 Ω
12	4990000 Ω	4490000 Ω

recorded orthogonal readings. The result was no discernable difference in both magnitude and phase measurements between the two orthogonal positions, indicating that the photodetectors did not introduce any measurable amount of polarization to the readings. Also a major part of our results deal with measuring the effects of intensity on

anisotropy and therefore it was necessary to ensure the linearity of the photodiodes. To measure this we simply varied the intensity of the light beam using a set of neutral density filters, which varied from 50% transmission to 0.1 % transmission. To measure this we first used an unfiltered beam to set the sensing resistor for a maximum voltage reading at V_{out} and then introduced the filters and measured the resulting voltage, from which the photocurrent was calculated. As we can see from the results for the Hamamatsu S1226-01 photodiode, shown in Figure 4-11, the photodiodes are linear over our measurement range.

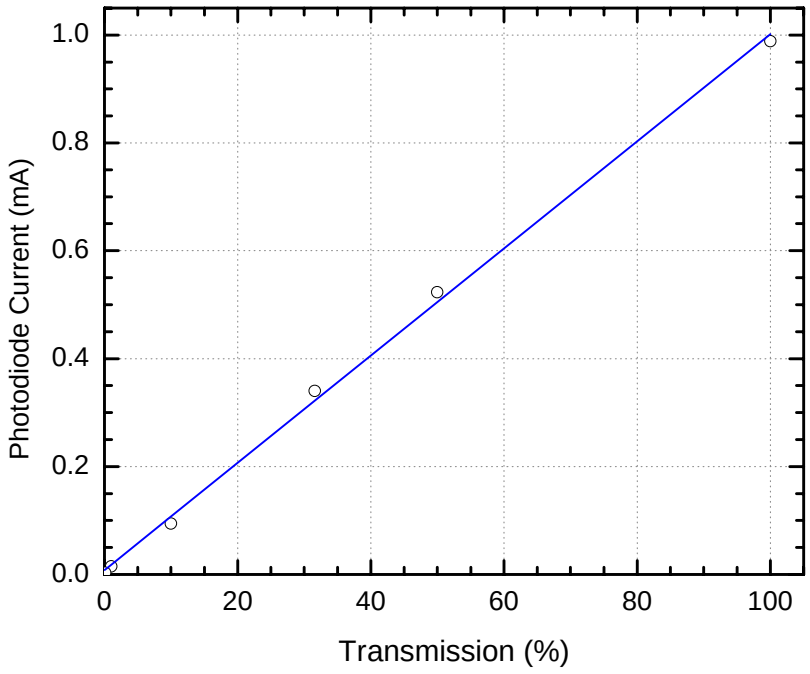

Figure 4-11: Graph showing the linearity measurement of the Hamamatsu S1226-01 photodiode.

4.3.5 Signal Processing Interface Box

This box was constructed to provide a means for signal routing and some minor signal processing. The box has two basic sections, one side processes the signal from the probe detector and the other side interfaces the rotating polarizer motor with the chopper control and processes the reference signal pulse.

The schematic diagram for processing the probe detector signal is shown in Figure 4-12. Because it was desirable to have a low probe intensity, the sensing resistor was required to have a high impedance. In order to make sure that the measurement equipment did not inadvertently load the detector, a buffer amplifier, U1, was used. The output of the buffer amplifier was fed to the lock-in amplifier ac input and the low pass filter, LPF, U2.

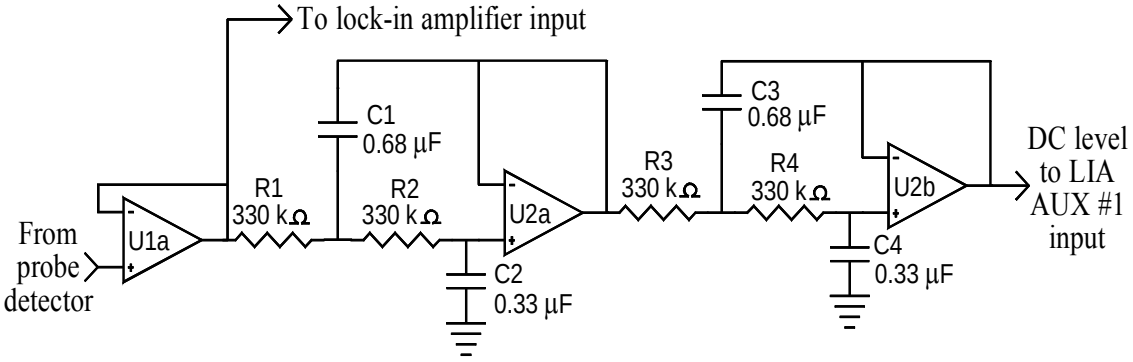

Figure 4-12: Schematic diagram of the probe detector signal processing circuit.

A Sallen-Key topology LPF circuit with unity gain was designed to strip off the ac signal so that the DC level could be measured separately. The ac portion of the probe signal was much less than the DC level, typically greater than 40 dB lower. Hence a fourth order LPF with a cutoff frequency at 1 Hz attenuated the ac signal to be greater than 70 dB less than the DC level (see frequency response shown in Figure 4-14). This was a sufficient difference to ensure the DC level measurement was not being affected by the varying ac signal.

The rotating polarizer controller circuit is basically a simple means to change from the Oriel chopper control connector to the connector used for the rotating analyzer. Processing the reference signal was also very minor as can be seen in Figure 4-13. A Schmitt trigger was incorporated in the reference signal line to guarantee a clean pulse edge. This signal was also split to provide a reference pulse for the lock-in amplifier as well as a frequency signal for the chopper controller.

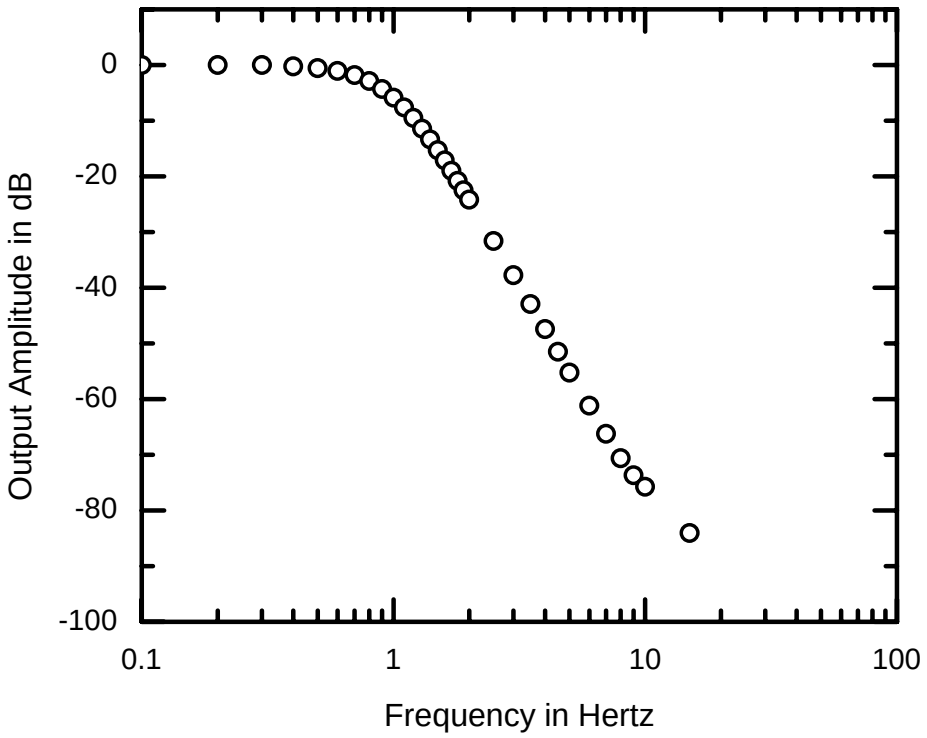

Figure 4-14: Frequency response of the unity gain low pass filter.

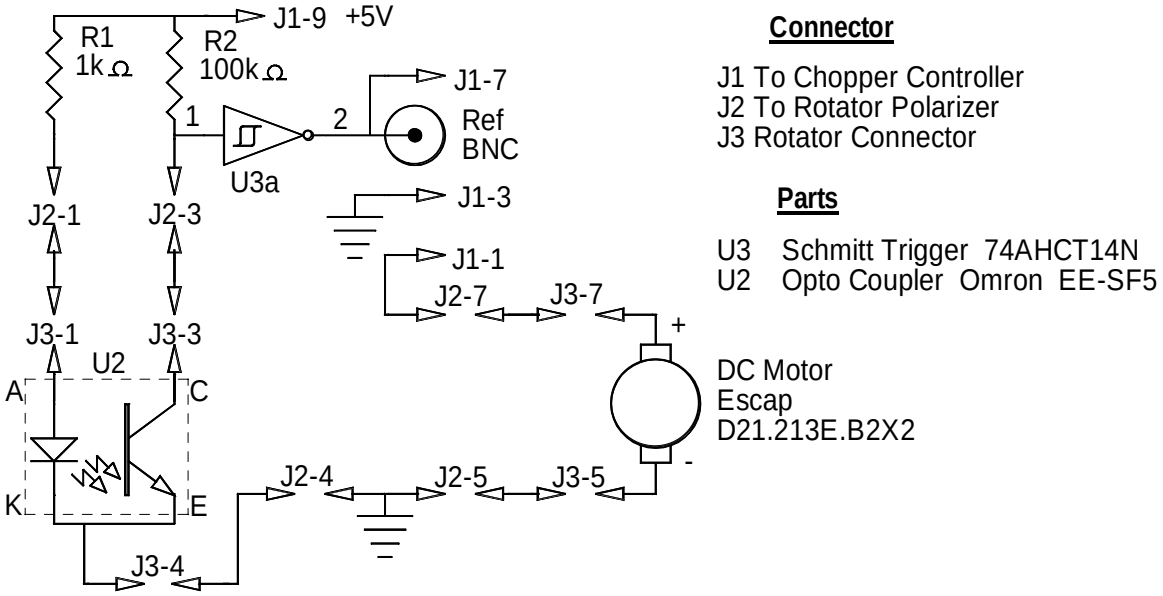

Figure 4-13: Rotating polarizer motor control circuit with reference pulse signal processing.

4.3.6 Lock-in Amplifier (LIA)

The polarization levels that are being measured will produce an ac signal in the millivolt range. A variation between measurements is in the microvolt range. Hence, it is necessary to have a measurement system accurate enough to discern between these levels. A lock-in amplifier is used to measure very small ac signals. The Standford Research Systems SR830 lock-in amplifier is capable of measuring ac signals down to a few nanovolts and is therefore ideal for this purpose. The SR830 lock-in amplifier uses a technique known as phase sensitive detection. It singles out a component of a signal based on a reference signal frequency and phase. All other signal frequencies and noise are eliminated. Basically it is a very narrow band detector that can measure a specific sinewave component of a signal even if it is obscured by excessive noise.

A phase sensitive detector is composed of a phase-locked loop and a multiplier. The lock-in amplifier has an internal oscillator that generates a sinewave that is phase locked to a reference signal. An external reference pulse for the lock-in amplifier in this setup came from the rotating analyzer. The repetitive pulse was generated by an Omron EE-SF5 reflective phototransistor and a piece of short silver tape on the rotating analyzer's cylindrical housing to reflect the light to the phototransistor. The internally generated lock-in amplifier reference signal is

$$V_L \sin\left(\omega_L t + \theta_{ref}\right) \tag{4.20}$$

where V_L is the magnitude, ω_L is the frequency that is phased locked to the frequency of the external reference and θ_{ref} is the phase difference between the external; and internal reference signals. This signal is mixed (multiplied) with the input signal

$$V_S \sin\left(\omega_S t + \theta_S\right) \tag{4.21}$$

where V_S is the magnitude of the input signal, ω_S is the frequency of the input signal and θ_S is the phase difference between the external reference and input signals. The output signal of the phase sensitive detector is simply the product of the two signals

$$V_{PSD} = V_S V_L \sin\left(\omega_S t + \theta_S\right)\sin\left(\omega_L t + \theta_{ref}\right)$$
$$= \tfrac{1}{2} V_S V_L \cos\left(\left[\omega_S - \omega_L\right]t + \theta_S - \theta_{ref}\right)$$
$$- \tfrac{1}{2} V_S V_L \cos\left(\left[\omega_S + \omega_L\right]t + \theta_S + \theta_{ref}\right)$$

which is a sum $\left(\omega_S + \omega_L\right)$ and difference $\left(\omega_S - \omega_L\right)$ of the frequencies. Only frequencies where $\omega_S = \omega_L$ produce a DC component. This phase sensitive output signal is then put through a low pass filter which removes the ac components. The result is that only input signals that are exactly the same frequency as the reference pass through. All other signal components are removed.

This is a narrow band detector because the magnitude of the undesired difference signals, $\left|\omega_{noise} - \omega_L\right|$ is small. Attenuation of the noise close to the desired signal depends on the bandwidth of the low pass filter. The resultant output of the low pass filter is

$$V_{PSD} = \tfrac{1}{2} V_S V_L \cos\left(\theta_S - \theta_{ref}\right) \tag{4.22}$$

a DC signal proportional to the desired signal amplitude. This 'bandwidth narrowing' is the primary advantage of the lock-in amplifier. Only input signals with frequencies at the reference frequency result in an output.

The SR830 has two phase sensitive detectors. The first is exactly as described above. The second phase sensitive detector mixes the input signal with the reference oscillator that is shifted by 90°

$$V_L \sin\left(\omega_L t + \theta_{ref} + 90°\right). \tag{4.23}$$

The resultant output is

$$V_{PSD_2} = \tfrac{1}{2} V_S V_L \sin\left(\theta_S - \theta_{ref}\right) \tag{4.24}$$

The two outputs are displayed by the SR830 as X and Y, where $X = V_{PSD_1} \cos\left(\theta_S - \theta_{ref}\right)$ and $Y = V_{PSD_2} \sin\left(\theta_S - \theta_{ref}\right)$. These two quantities represent the signal as a vector relative to the lock-in reference oscillator.

The SR830 is a digital lock-in amplifier and therefore the input signal is digitized by a 16 bit A/D converter. The sampling frequency is at 256 kHz and a 102 kHz anti-aliasing filter is incorporated to prevent higher frequencies from being down sampled. The frequency of interest for this research is in the order of 10 Hz, well within the sampling range of this lock-in amplifier. The time constant of the lock-in amplifier was set for 1 second. With measurements being recorded every 5 seconds and time constants for the fastest anisotropy buildup at approximately 50 seconds. A time constant of 1 second was found to provide a good signal measurement with minimal noise.

4.3.7 Data Acquisition

Data acquisition was performed using a pentium personal computer, PC, via a GPIB bus connection to a Stanford Research Systems lock-in amplifier, model number SR830. The PC used the National Instruments LabVIEW program to poll the lock-in amplifier and record the measurements via a National Instruments PCI-GPIB card mounted in the PC. The LabVIEW program was coded to record measurements from the lock-in amplifier every 5 seconds. These measurement parameters included the ac magnitude and phase along with the DC level of the probe beam, the sampled pump beam intensity as well as a date and time stamp for each measurement. As measurements were acquired they were saved to a file for later processing.

Chapter 5

Experimental Aspects

5.1 Introduction

This chapter starts with describing what unpolarized light is and the difficulties involved in producing it. Then we describe how the amount of linear photoinduced anisotropy is determined from experimentally measurable quantities, as well as how these measurements were made with the apparatus described in the previous chapter. Following this is a brief description of the process we used to measure the dark relaxation of a sample that has undergone photoinduced dichroism. The chapter ends by providing a quantitative analysis of the experimental measurement technique in order to determine the amount of anisotropy from the measured quantities.

5.2 Unpolarized Light Source

A source that has no discernable polarization direction or rather has an intensity equally distributed over a full 360° rotation of an analyzer perpendicular to the direction of propagation, is referred to as being a completely unpolarized light source. This term is actually misleading since each excited atom from a light source emits a photon with a distinct polarization. New photons are constantly being radiated from arbitrarily orientated atomic emitters and therefore the polarization direction is constantly changing in a totally random manner. Hence, a better term to use would be natural light [62]. It should be noted that completely unpolarized as well as completely polarized light represent two extremes. In general, a light source should be referred to as partially polarized. Even light from a source that one would expect to be completely unpolarized (i.e. the sun), there is nonetheless residual polarization that arises from unavoidable scattering or reflections.

The ideal probe light for this apparatus is a completely unpolarized source, as any source polarization would have to be extracted from the measurements of the photoinduced dichroism of the sample. Producing a completely unpolarized source proved to be very difficult as several sources were tried; halogen lamp, incandescent bulb with a straight tungsten filament powered from a DC source, different types of light emitting diodes, LEDs, and even producing circularly polarized light from a linearly polarized laser through a ¼ wave plate[1], all of which showed varying degrees of polarization. The best partially polarized probe source we found was produced by an array of 19 red LEDs ($\lambda \cong 666$ nm) shinning through frosted glass. This probe source has been fully described in Section 4.3.1.

5.3 Measuring Photoinduced Linear Anisotropy.

Initially the sample is isotropic as all glasses are but, after illumination with a linearly polarized strong light beam, a photoinduced anisotropy will build up as a function of time. As a result, the material becomes dichroic. Stated differently, dichroism is photoinduced by a linearly polarized pump light. In order to measure and characterize this phenomenon, the absorption of two orthogonal polarization directions must be observed as a function of the inducing irradiation intensity and time. This is achieved by means of a rotating analyzer inserted in the unpolarized probe beam line. From the definition of anisotropy, the material will have two absorption coefficients, α, which in this case corresponds to the polarization direction of the light; respectively $\alpha_{//}$ and $\alpha_{\perp}$ with // denoting the direction of polarization parallel to the inducing beam's polarization orientation. Linear dichroism is defined as

$$\Gamma = \alpha_{\perp} - \alpha_{//} \tag{5.1}$$

[1] Theoretically this should have produced the desired signal, an equal intensity beam when resolved through a full 360° rotation of an analyzer perpendicular to the direction of propagation. The problem is we are trying to produce a near perfect circularly polarized signal, which would require a perfect linearly polarized monochromatic source and a ¼ wave plate cut specifically for that wavelength. Both of these requirements are near impossible to produce or extremely expensive.

Since we are measuring the transmitted light after it has passed through the sample we have

$$I_{\perp} = I_0 e^{-\alpha_{\perp} L} \tag{5.2}$$

$$I_{//} = I_0 e^{-\alpha_{//} L} \tag{5.3}$$

where $I_{\perp}$ and $I_{//}$ are the intensities at the respective polarization directions after passing through the sample, I_0 is the intensity of the initial unpolarized probe beam, and L is the thickness of the sample.

The relative anisotropy can be defined as

$$A = \frac{2(I_{//} - I_{\perp})}{I_{//} + I_{\perp}} \tag{5.4}$$

Inserting Equations 5.2 and 5.3 into 5.4 and using the definition of dichroism (Equation 5.1). We find that $A \cong \Gamma L$ for small values of ΓL, namely << 1 [55]

$$A = \frac{I_{//} - I_{\perp}}{(I_{//} + I_{\perp})/2} = (\alpha_{\perp} - \alpha_{//})L \tag{5.5}$$

This equation relates the measured quantities $I_{\perp}$ and $I_{//}$ to the definition of dichroism. The numerator is basically an ac quantity and the denominator the average or DC quantity. Two assumptions were made for this equation to be valid: (a) that $\Gamma L << 1$. This is warranted considering the fact that a 5% photoinduced dichroism change is referred to as 'giant' with these materials. (b) The influence of reflection anisotropy is small and therefore not taken into account. It was previously determined [55] that the difference in reflection coefficients of the parallel $(r_{//})$ and perpendicular $(r_{\perp})$ beams (i.e. reflection anisotropy) were small and could be ignored.

Referring to the aerial view of the experimental setup in Figure 5-1 we see that the probe source was modulated by a rotating polarizer. Rotational modulation was

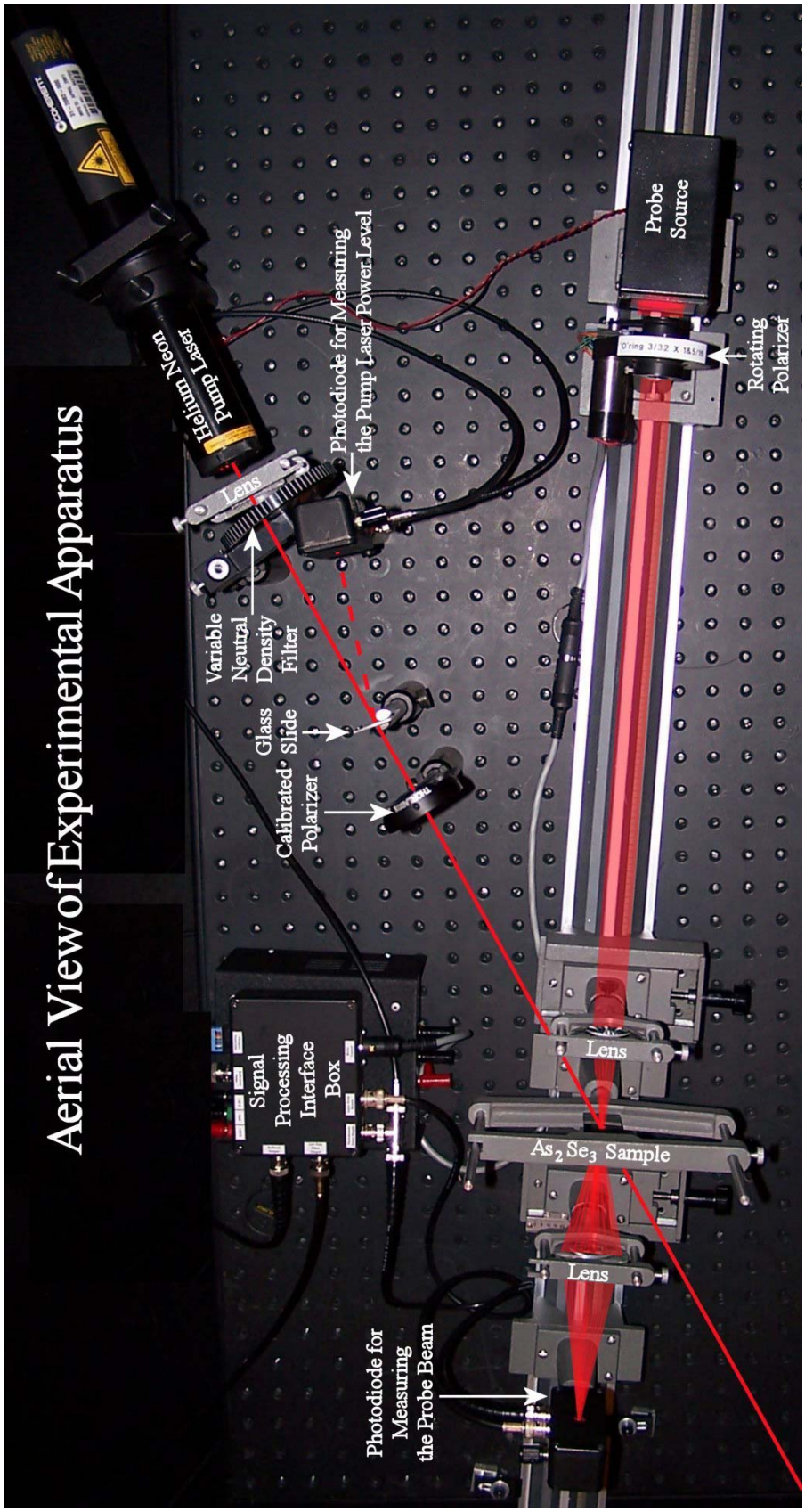

Figure 5-1: Aerial view of experimental apparatus. Beam lines (red) have been drawn for clarity.

used to facilitate the measurement of the two orthogonal directions necessary for determining anisotropy. The rotations per minute of the analyzer was set for 300 RPM or 5 Hz. The modulated probe beam was detected by a Hamamatsu number S1336-8BK photodiode. The resulting electrical signal from the probe detector was an ac signal with a DC offset. Both the ac and DC signals were measured by a Stanford Research Systems lock-in amplifier, model number SR830. To record the proper DC level the probe detector signal was first sent through a unity gain low pass filter to strip off the ac portion and then connected to the AUX #1 A/D converter on the lock-in amplifier.

The pump beam intensity was set using a variable neutral density filter (see Figure 5-1). The intensity level was monitored by reflecting a fraction of the beam off an ordinary glass slide to a second photodetector, a Hamamatsu number S1223-01 PIN photodiode. The pump intensity level was also measured via the lock-in amplifier. Polarization of the inducing beam was controlled by a calibrated polarizer. The pump beam's polarization would be orientated first in the vertical direction until saturation,

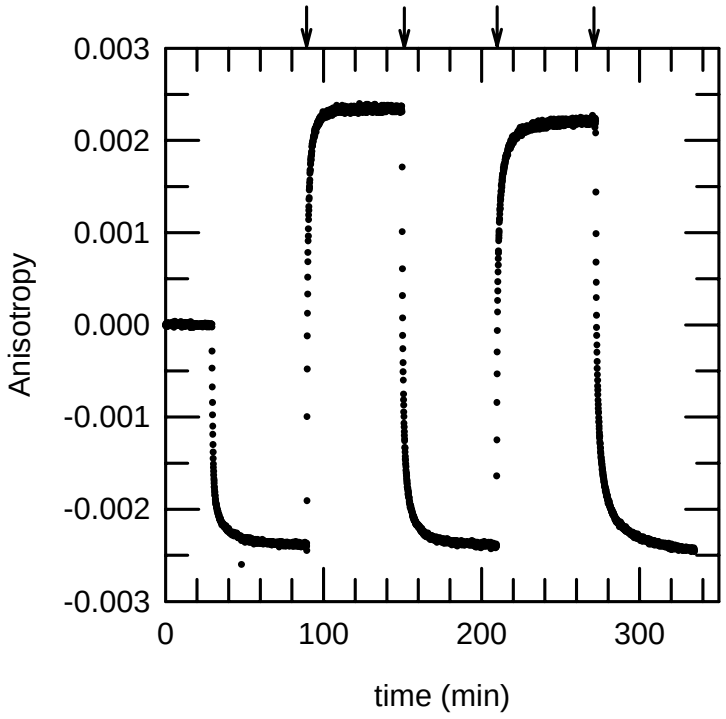

Figure 5-2: Time dependence of the dichroism in As_2Se_3. The polarized pump beam was applied at 30 minutes and the polarization was rotated by 90º at the times indicated by the arrows.

then changed to the horizontal direction until saturation, then vertical, horizontal, etc for a total of 12 polarization changes. Each polarization change represents a cycle and each cycle lasted for 30 minutes to 2 hours depending on the intensity of the pump beam. The lower the intensity, the longer the required cycle time in order to saturate the photoinduced dichroism. A typical buildup of photoinduced dichroism and repeated reorientation is shown in Figure 5-2.

Measurements were recorded every 5 seconds to accurately follow the anisotropy buildup as a function of time.

5.4 Quantitative Analysis of the Measurement Technique[2]

5.4.1 Introduction

This section explains the mathematics used to determine the lock-in amplifier's measured quantities of the probe beam as they pertain to anisotropy. To determine this, wave functions and probability are used for the probe beam as it passes through the experimental apparatus. We start with analyzing an ensemble of linearly polarized photons as they pass through a polarizer. This ensemble is then expanded into a partially polarized light source, which consists of an unpolarized fraction, f_U, and a polarized fraction, f_P. The partially polarized light is then passed through the rotating polarizer and sample. The resulting photodetected signal is then broken down into the different measured quantities, R and θ of the *2f* component and the average or DC voltage. In the last section, the measured quantities are used to determine the anisotropy namely $(\alpha_{\perp} - \alpha_{//})L$.

[2] The author acknowledges that the mathematics in this section was derived by Professor R.E. Johanson, University of Saskatchewan.

5.4.2 Photon Through a Polarizer

The wave function of a photon linearly polarized at angle γ with respect to the *x* axis can be written as

$$\left|\psi_\gamma\right\rangle = \cos\gamma\left|x\right\rangle + \sin\gamma\left|y\right\rangle \tag{5.6}$$

where $\left|x\right\rangle$ and $\left|y\right\rangle$ are the eigen functions for *x* and *y* linear polarizations respectively. An analyzer at angle φ establishes a pass axis x' and will allow through a $\left|x'\right\rangle$ photon. The probability that $\left|\psi_\gamma\right\rangle$ is in the $\left|x'\right\rangle$ state is

$$\left|\left\langle x'\middle|\psi_\gamma\right\rangle\right|^2 = \left|\cos\gamma\left\langle x'\middle|x\right\rangle + \sin\gamma\left\langle x'\middle|y\right\rangle\right|^2 \tag{5.7}$$

The amplitudes $\langle x'|x\rangle$ and $\langle x'|y\rangle$ are just two of the components of the rotation matrix that takes *x* into x'.

$$\left\langle x'\middle|x\right\rangle = \cos\varphi \quad \text{and} \quad \left\langle x'\middle|y\right\rangle = \sin\varphi$$

So as expected the probability of getting through the analyzer is

$$\left|\left\langle x'\middle|\psi_\gamma\right\rangle\right|^2 = \left(\cos\gamma\cos\varphi + \sin\gamma\sin\varphi\right)^2 = \cos^2\left(\gamma-\varphi\right) \tag{5.8}$$

The operator for the polarizer is simply

$$P = \left|x'\right\rangle\left\langle x'\right| \tag{5.9}$$

5.4.3 Arbitrary Beam Through a Polarizer

Consider an ensemble A of photons. Each photon is polarized at an angle γ

$$\left|\psi_\gamma\right\rangle = \cos\gamma\left|x\right\rangle + \sin\gamma\left|y\right\rangle \tag{5.6}$$

Let the probability density of a photon being polarized at angle γ be $P(\gamma)$

$$\int_0^{2\pi} P(\gamma)d\gamma = 1 \tag{5.10}$$

Passing the ensemble through a polarizer with a pass axis x' at angle φ. The

probability of the photon $\left|\psi_\gamma\right\rangle$ passing through the analyzer is $\cos^2(\gamma-\varphi)$. The average probability of a photon in the ensemble passing through the analyzer is

$$P_A(\varphi)=\int_0^{2\pi} P(\gamma)\cos^2(\gamma-\varphi)\,d\gamma$$

$$\begin{aligned} P_A(\varphi) &= \cos^2(\varphi)\int_0^{2\pi} P(\gamma)\cos^2(\gamma)\,d\gamma+\sin^2(\varphi)\int_0^{2\pi} P(\gamma)\sin^2(\gamma)d\gamma \\ &+\cos(\varphi)\sin(\varphi)\int_0^{2\pi} P(\gamma)\cos(\gamma)\sin(\gamma)\,d\gamma \end{aligned} \tag{5.11}$$

Defining *a*, *b* and *c* as

$$P_A(\varphi)=a\cos^2(\varphi)+b\sin^2(\varphi)+c\cos(\varphi)\sin(\varphi) \tag{5.12}$$

Consider another ensemble A' consisting of a fraction f_U of the photons with

$$P_U(\gamma)=\frac{1}{2\pi}$$

(i.e. unpolarized) and a fraction f_P with $P_P(\gamma)=\frac{1}{2}\delta(\gamma-\chi)+\frac{1}{2}\delta(\gamma+\pi-\chi)$ (i.e. linearly polarized light at angle χ). $f_U+f_P=1$ and $P(\gamma)=f_U P_U(\gamma)+f_P P_P(\gamma)$.

Notice that $\int_0^{2\pi} P(\gamma)\,d\gamma=1$. The average probability of a photon in A' passing through an analyzer with x' at angle φ is

$$\begin{aligned} P_{A'}(\varphi) &= \int_0^{2\pi}\frac{f_U}{2\pi}\cos^2(\gamma-\varphi)\,d\gamma+\int_0^{2\pi}\frac{f_P}{2}\delta(\gamma-\chi)\cos^2(\gamma-\varphi)\,d\gamma \\ &+\int_0^{2\pi}\frac{f_P}{2}\delta(\gamma+\pi-\chi)\cos^2(\gamma-\varphi)\,d\gamma \end{aligned}$$

which yields

$$P_{A'}(\varphi)=\frac{f_U}{2}+f_P\cos^2(\chi-\varphi) \tag{5.13}$$

We want to show that $P_A(\varphi)=P_{A'}(\varphi)$ and determine f_U, f_P and χ in terms of *a*, *b* and *c*.

Observe that

$$P_{A'}(\varphi)=\frac{f_U}{2}+f_P\left[\cos^2(\varphi)\cos^2(\chi)+\sin^2(\varphi)\sin^2(\chi)+\cos(\varphi)\sin(\varphi)\cos(\chi)\sin(\chi)\right] \tag{5.14}$$

Using the trigonometric identity $\sin^2(\varphi)=1-\cos^2(\varphi)$ yields

$$\begin{aligned}P_{A'}(\varphi)&=\left[\frac{f_U}{2}+f_P\sin^2(\chi)\right]+f_P\left[\cos^2(\chi)-\sin^2(\chi)\right]\cos^2(\varphi)\\&+f_P\cos(\varphi)\sin(\varphi)\cos(\chi)\sin(\chi)\end{aligned} \tag{5.15}$$

Also $P_A(\varphi)$ can be rewrote in a similar way.

$$P_A(\varphi)=b+(a-b)\cos^2(\varphi)+c\cos(\varphi)\sin(\varphi) \tag{5.16}$$

In order for $P_A(\varphi)=P_{A'}(\varphi)$ we must have

$$c=f_P\cos(\chi)\sin(\chi)=\tfrac{1}{2}f_P\sin(2\chi) \tag{5.17}$$

$$a-b=f_P\left[\cos^2(\chi)-\sin^2(\chi)\right]=f_P\cos(2\chi)=f_P\left[1-2\sin^2(\chi)\right] \tag{5.18}$$

$$b=\tfrac{1}{2}f_U+f_P\sin^2(\chi) \tag{5.19}$$

Solving for f_U, f_P, χ

$$f_U=2b-2f_P\sin^2(\chi)$$

but

$$-2f_P\sin^2(\chi)=a-b-f_P$$

so

$$f_U=2b+a-b-f_P=a+b-f_P=a+b-\left[(a-b)^2+4c^2\right]^{\frac{1}{2}} \tag{5.20}$$

and

$$f_P=\frac{a-b}{\cos(2\chi)}=\frac{a-b}{\cos\left(\tan^{-1}\left(\frac{2c}{a-b}\right)\right)}$$

since

$$\cos\left(\tan^{-1}(x)\right) = \frac{1}{\left(1+x^2\right)^{\frac{1}{2}}}$$

$$f_P = [a-b]\left[1+\left(\frac{2c}{a-b}\right)^2\right]^{\frac{1}{2}} = \left[(a-b)^2+4c^2\right]^{\frac{1}{2}} \tag{5.21}$$

and

$$\frac{c}{a-b} = \tfrac{1}{2}\tan(2\chi) \Rightarrow \chi = \tfrac{1}{2}\tan^{-1}\left(\frac{2c}{a-b}\right) \tag{5.22}$$

Notice $f_U + f_P = a+b = \int_0^{2\pi} P(\theta)\left[\cos^2(\varphi)+\sin^2(\varphi)\right]d\theta = 1$ as it should be.

In summary, if we chose

$$f_U = 1-\left[(a-b)^2+4c^2\right]^{\frac{1}{2}} \tag{5.20}$$

$$f_P = \left[(a-b)^2+4c^2\right]^{\frac{1}{2}} \tag{5.21}$$

$$\chi = \tfrac{1}{2}\tan^{-1}\left(\frac{2c}{a-b}\right) \tag{5.22}$$

then the output of the analyzer will be the same as the original ensemble *A*. i.e. $P_A(\varphi) = P_{A'}(\varphi)$. An arbitrary beam of light is equivalent to the superposition of an unpolarized beam with a linearly polarized beam.

The intensity of the light that passes through the analyzer is directly related to $P_A(\varphi)$. If the photon flux from the source is $F\left(photons/area/sec\right)$ then

$$I_A = hvFP_A(\varphi) \tag{5.23}$$

5.4.4 Light Through an Absorbing Sample

A dichroic sample has different absorption coefficients depending on the polarization of the light. Let αx be the absorption coefficient for a $|x\rangle$ photon and αy

for a $|y\rangle$ photon. The operator for the sample is

$$S_{op} = e^{-\alpha xL}|x\rangle\langle x| + e^{-\alpha yL}|y\rangle\langle y| \tag{5.24}$$

where L is the sample thickness, (reflections from boundaries are ignored).

For a photon polarized at angle γ

$$|\psi_\gamma\rangle = \cos(\gamma)|x\rangle + \sin(\gamma)|y\rangle \tag{5.6}$$

The sample produces

$$S_{op}|\psi_\gamma\rangle = e^{-\alpha xL}\cos(\gamma)|x\rangle + e^{-\alpha yL}\sin(\gamma)|y\rangle \tag{5.25}$$

The probability the photon is not absorbed is

$$e^{-2\alpha xL}\cos^2(\gamma) + e^{-2\alpha yL}\sin^2(\gamma) \tag{5.26}$$

For an ensemble of photons *A*, the average probability for a photon to pass through the sample is

$$P_A = \int_0^{2\pi} P(\gamma)\left[e^{-2\alpha xL}\cos^2(\gamma) + e^{-2\alpha yL}\sin^2(\gamma)\right]d\gamma \tag{5.27}$$

Or using the notation of the previous section

$$P_A = e^{-2\alpha xL}\int_0^{2\pi} P(\gamma)\cos^2(\gamma)\,d\gamma + e^{-2\alpha yL}\int_0^{2\pi} P(\gamma)\sin^2(\gamma)\,d\gamma \tag{5.28}$$

$$P_A = ae^{-2\alpha xL} + be^{-2\alpha yL} \tag{5.29}$$

We want to show that this result is the same if we start with the special distribution

$$P(\gamma) = \frac{f_U}{2\pi} + f_P\left[\tfrac{1}{2}\delta(\gamma-\chi) + \tfrac{1}{2}\delta(\gamma+\pi-\chi)\right] \tag{5.30}$$

(i.e. An unpolarized beam and a polarized beam.) where f_U, f_P, and χ are related to *a*, *b*, and *c* as in the previous section.

$$P_{A'} = \frac{f_U}{2\pi}\left[\int_0^{2\pi} e^{-2\alpha xL}\cos^2(\gamma)\,d\gamma + \int_0^{2\pi} e^{-2\alpha yL}\sin^2(\gamma)\,d\gamma\right] \tag{5.31}$$

$$+ f_P\left[e^{-2\alpha xL}\cos^2(\chi) + e^{-2\alpha yL}\sin^2(\chi)\right] \tag{5.32}$$

$$= \tfrac{1}{2}f_U\left[e^{-2\alpha xL} + e^{-2\alpha yL}\right] + f_P\left[e^{-2\alpha xL}\cos^2(\chi) + e^{-2\alpha yL}\sin^2(\chi)\right] \tag{5.33}$$

Recall, also from the previous section

$$f_U = 1 - \left[(a-b)^2 + 4c^2 \right]^{\frac{1}{2}} \tag{5.20}$$

$$f_P = \left[(a-b)^2 + 4c^2 \right]^{\frac{1}{2}} \tag{5.21}$$

$$\chi = \tfrac{1}{2} \tan^{-1}\left(\frac{2c}{a-b} \right) \tag{5.22}$$

and using the following identities

$$\cos\left(\tfrac{1}{2} \tan^{-1}(x) \right) = \pm \left(\frac{1}{2} \left[1 + \frac{1}{\left(1+x^2\right)^{\frac{1}{2}}} \right] \right)^{\frac{1}{2}}$$

$$\sin\left(\tfrac{1}{2} \tan^{-1}(x) \right) = \pm \left(\frac{1}{2} \left[1 - \frac{1}{\left(1+x^2\right)^{\frac{1}{2}}} \right] \right)^{\frac{1}{2}}$$

then

$$P_{A'} = \frac{1}{2}\left(1 - \left[(a-b)^2 + 4c^2 \right]^{\frac{1}{2}} \right)\left(e^{-2\alpha xL} + e^{-2\alpha yL} \right)$$

$$+ \left[(a-b)^2 + 4c^2 \right]^{\frac{1}{2}} \left[\frac{1}{2}\left(1 + \frac{a-b}{\left[(a-b)^2 + 4c^2 \right]^{\frac{1}{2}}} \right) e^{-2\alpha xL} + \frac{1}{2}\left(1 - \frac{a-b}{\left[(a-b)^2 + 4c^2 \right]^{\frac{1}{2}}} \right) e^{-2\alpha yL} \right]$$

$$= \frac{1}{2}\left(1 - \left[(a-b)^2 + 4c^2 \right]^{\frac{1}{2}} \right)\left(e^{-2\alpha xL} + e^{-2\alpha yL} \right)$$

$$+ \frac{1}{2}\left[\left(\left[(a-b)^2 + 4c^2 \right]^{\frac{1}{2}} + (a-b) \right) e^{-2\alpha xL} + \left(\left[(a-b)^2 + 4c^2 \right]^{\frac{1}{2}} - (a-b) \right) e^{-2\alpha yL} \right]$$

$$= \tfrac{1}{2}\left[(1+a-b) e^{-2\alpha xL} + (1-a+b) e^{-2\alpha yL} \right] \tag{5.34}$$

But since $a+b=1$, $1+a-b=2a$, and $1-a+b=2b$ then

$$P_{A'} = a e^{-2\alpha xL} + b e^{-2\alpha yL} = P_A \tag{5.35}$$

So again we replace an arbitrary distribution of polarizations with a randomly polarized beam plus a linearly polarized beam.

5.4.5 Experiment: Polarizer + Sample

Consider the case where the analyzer precedes the sample as in our experimental apparatus. This arrangement is a bit simpler since all photons after the analyzer are in the same state. The light source produces an ensemble of photons with a distribution of polarizations that we take to be

$$P(\gamma) = \frac{f_U}{2\pi} + \tfrac{1}{2} f_P \left[\delta(\gamma - \chi) + \delta(\gamma + \pi - \chi) \right] \tag{5.30}$$

Let the analyzer's pass axis be at angle φ. After the analyzer all photons will be in the same state namely

$$\left|\psi_\varphi\right\rangle = \cos(\varphi)\left|x\right\rangle + \sin(\varphi)\left|y\right\rangle \tag{5.36}$$

The intensity is proportional to the average probability of a photon passing through the analyzer.

$$P_A(\varphi) = \frac{f_U}{2} + f_P \cos^2(\chi - \varphi) \tag{5.37}$$

This new ensemble of photons passes through the sample with an average probability per photon of

$$P_S = e^{-2\alpha x L} \cos^2(\varphi) + e^{-2\alpha y L} \sin^2(\varphi) \tag{5.38}$$

The intensity at the detector is

$$I = h\nu F P_A P_S \tag{5.39}$$

$$I = h\nu F \left[\frac{f_U}{2} + f_P \cos^2(\chi - \varphi) \right] \left[e^{-2\alpha x L} \cos^2(\varphi) + e^{-2\alpha y L} \sin^2(\varphi) \right] \tag{5.40}$$

Rewrite the second parenthesis as

$$\left[\Delta \cos(2\varphi) + \Sigma \right]$$

where $\Delta = \tfrac{1}{2}\left[e^{-2\alpha x L} - e^{-2\alpha y L} \right]$ and $\Sigma = \tfrac{1}{2}\left[e^{-2\alpha x L} + e^{-2\alpha y L} \right]$

As well rewrite the first parenthesis as

$\tfrac{1}{2}\left[f_U + f_P + f_P \cos 2(\chi - \varphi) \right] = \tfrac{1}{2}\left[1 + f_P \cos 2(\chi - \varphi) \right]$ and since $f_U + f_P = 1$

then

$$I = \tfrac{1}{2} h\nu F \left[1 + f_P \cos 2(\chi - \varphi)\right]\left[\Delta \cos(2\varphi) + \Sigma\right] \tag{5.41}$$

Here it is convenient to switch to complex exponentials using $\cos(x) = \tfrac{1}{2}\left[e^{ix} + e^{-ix}\right]$

Therefore

$$I = \frac{h\nu F}{2}\left[1 + \tfrac{1}{2} f_P \left(e^{2i(\chi-\varphi)} + e^{-2i(\chi-\varphi)}\right)\right] \bullet \left[\Delta \tfrac{1}{2}\left(e^{2i\varphi} + e^{-2i\varphi}\right) + \Sigma\right] \tag{5.42}$$

Multiplying all this out and grouping terms gives

(DC) $$I = \frac{h\nu F}{2}[\Sigma + \tfrac{1}{2} f_P \Delta \cos(2\chi)$$

(*2f*) $$+\Delta \cos(2\varphi) + f_P \Sigma \cos 2(\chi - \varphi)$$

(*4f*) $$+\tfrac{1}{2} f_P \Delta \cos 2(\chi - 2\varphi)] \tag{5.43}$$

For a rotating analyzer $\varphi = 2\pi ft$. Then the first term above is the DC part, the second term the *2f* (2^{nd} harmonic) part and the third term the *4f* (4^{th} harmonic) part. We are mainly interested in the *2f* term.

$$I_{2f} = \frac{h\nu F}{2}\left[\Delta \cos(2\varphi) + f_P \Sigma \cos 2(\chi - \varphi)\right] \tag{5.44}$$

Once again it is more convenient to use complex notation and to make the argument of the second cosine term $\cos 2(\chi - \varphi)$.

$$I_{2f} = \frac{h\nu F}{2} \mathrm{Re}\left[\left(\Delta + f_P \Sigma e^{-2i\chi}\right) e^{2i\varphi}\right] \tag{5.45}$$

The phasors in the parenthesis determine the magnitude and phase of the *2f* signal, which is what the lock-in amplifier measures.

Magnitude $$\left|I_{2f}\right| = \frac{h\nu F}{2}\left[\left(\Delta + f_P \Sigma \cos(2\chi)\right)^2 + \left(f_P \Sigma \sin(2\chi)\right)^2\right]^{\frac{1}{2}}$$

$$\left|I_{2f}\right| = \frac{h\nu F}{2}\left[\Delta^2 + {f_P}^2 \Sigma^2 + 2\Delta\Sigma f_P \cos(2\chi)\right]^{\frac{1}{2}} \tag{5.46}$$

Phase $$\theta = \tan^{-1}\left(\frac{-f_P \Sigma \sin(2\chi)}{\Delta + f_P \Sigma \cos(2\chi)}\right) \tag{5.47}$$

Notice if $f_P = 0$ then $\left|I_{2f}\right| = \frac{h\nu F}{2}\Delta$ and $\theta = 0$.

As well with no sample $\Sigma = 1$, $\Delta = 0$

$$\left|I_{2f}\right| = \frac{h\nu F}{2} f_P \tag{5.48}$$

and

$$\theta = -2\chi \tag{5.49}$$

The DC part is also interesting

$$I_{DC} = \frac{h\nu F}{2}\left[\Sigma + \tfrac{1}{2} f_P \Delta \cos\left(2\chi\right)\right] \tag{5.50}$$

Notice if $f_P = 0$ or $\Delta = 0$ (i.e. an isotropic sample) then

$$I_{DC} = \frac{h\nu F}{2}\Sigma \tag{5.51}$$

and with no sample

$$I_{DC} = \frac{h\nu F}{2} = I_O \tag{5.52}$$

This makes the calibration of the system very simple. Before an anisotropy run was recorded, a measurement of the system was taken with no sample in place. From this no sample measurement the initial probe intensity, I_O, as well as the amount of linear polarization and angle was determined. The polarization of the probe source is crucial information as any source polarization has to be removed in order to determine the amount of induced anisotropy.

5.4.6 Determining Anisotropy from the Measured Quantities

This section shows how the amount of anisotropy was calculated using the variables, namely Δ and Σ, from the equations of what the lock-in amplifier measures. Refer to the previous Section 5.4.5 equation numbers (5.46) and (5.47).

Recall the basic anisotropy equation

$$A = \left(\alpha x - \alpha y\right) L \tag{5.5}$$

Also recall from Section 5.4.5

$$\Delta = \frac{e^{-2\alpha xL} - e^{-2\alpha yL}}{2}, \qquad \Sigma = \frac{e^{-2\alpha xL} + e^{-2\alpha yL}}{2}$$

To simplify the expressions let $x = 2\alpha xL$ and $y = 2\alpha yL$.

Therefore

$$\Delta = \frac{e^{-x} - e^{-y}}{2}, \qquad \Sigma = \frac{e^{-x} + e^{-y}}{2}$$

$$\Sigma + \Delta = \frac{e^{-x}}{2} + \frac{e^{-y}}{2} + \frac{e^{-x}}{2} - \frac{e^{-y}}{2} = e^{-x}$$

$$\Sigma - \Delta = \frac{e^{-x}}{2} + \frac{e^{-y}}{2} - \frac{e^{-x}}{2} + \frac{e^{-y}}{2} = e^{-y}$$

Hence

$$-x = \ln(\Sigma + \Delta) \quad \text{and} \quad -y = \ln(\Sigma - \Delta)$$

Replacing *x* and *y* gives

$$-2\alpha xL = \ln(\Sigma + \Delta) \quad \text{and} \quad -2\alpha yL = \ln(\Sigma - \Delta)$$

$$\Rightarrow \alpha xL = -\tfrac{1}{2}\ln(\Sigma + \Delta) \quad \text{and} \quad -\alpha yL = \tfrac{1}{2}\ln(\Sigma - \Delta)$$

Therefore the anisotropy in terms of Δ and Σ is

$$A = (\alpha x - \alpha y)L = \tfrac{1}{2}\ln(\Sigma - \Delta) - \tfrac{1}{2}\ln(\Sigma + \Delta) = \tfrac{1}{2}\ln\left(\frac{\Sigma - \Delta}{\Sigma + \Delta}\right)$$

For an isotropic sample $\Delta = 0$, $\Sigma = 1$ and $A = \tfrac{1}{2}\ln\left(\frac{1-0}{1+0}\right) = \tfrac{1}{2}\ln(1) = 0$ as it should be.

$$\boxed{A = \frac{1}{2}\ln\left(\frac{\Sigma - \Delta}{\Sigma + \Delta}\right)} \tag{5.53}$$

In order to determine the amount of photoinduced anisotropy we have to determine Σ and Δ. These variables where solved from the measured data using a MatLab program. See Appendix A, Solve_Anisotropy.m to view the MatLab program.

"Engineering without mathematics is like philosophy."
S.O. Kasap EE217 and EE317 Class Lectures

Chapter 6

Results and Discussion

6.1 Introduction

Chapter 5 presented the mathematics and experimental details of the study undertaken in this work. The experimental results and their discussion are presented in this chapter. The samples used throughout the course of this work were thin films of amorphous As_2Se_3 of thicknesses from 0.25 μm to 1.93 μm.

The chapter provides experimental data on photoinduced dichroism in amorphous As_2Se_3 thin films. The results are then compared with similar studies reported previously. The chapter starts with an explanation of the choice of inducing light wavelength, thickness of the sample and basic statistical methodologies that are introduced. Section 6.2.1 introduces experimental results for the dependence of photoinduced dichroism kinetics on the inducing light intensity, namely the time constant, $\tau(I)$, and the stretching exponent, $\beta(I)$. Reversibility of the photoinduced dichroism and the anisotropy saturation level, A_{sat}, are discussed in Section 6.2.2. Lastly, results on the dependence of the saturated anisotropy level, $A_{sat}(L)$ and the stretching exponent, $\beta(L)$, on the sample thickness, L, is evaluated in Section 6.2.3

6.2 Photoinduced Anisotropy Measurements

Measurements of photoinduced dichroism consisted of irradiating the sample with a pump or inducing linearly polarized source. In our case we used a linearly polarized helium neon laser (λ = 632.8 nm). The intensity of the pump source ranged from 77 μW/mm^2 to 1.18 mW/mm^2 and was adjusted by means of a variable neutral density filter (see Figures 4-2 and 5-1). The progress of the dichroism buildup was monitored by an unpolarized light source from an array of 19 red LEDs. The light from

the LEDs was passed through a polarizer rotating at 300 rpm and focused to a spot on the sample; the unpolarized light from the LEDs is hereafter called the *probe beam*. The probe beam was then refocused and detected by a Hamamatsu number S1336-8BK photodiode. The resulting electrical signal from the probe detector consisted of an ac signal with a DC offset. Both the ac and DC signals were measured by a Stanford Research Systems lock-in amplifier, model number SR830. To record the proper DC level the probe detector signal was first sent through a unity gain low pass filter to strip off the ac portion and then connected to the AUX #1 A/D converter on the lock-in amplifier. The intensity of the probe beam at the sample was measured to be approximately 13.6 $\mu W/mm^2$, which was more than 5 times less than the lowest inducing light intensity used. Hence, the probe beam had no measurable effect on the sample. For further information on the probe source the reader is referred to in Section 4.3.1 of the thesis.

Special attention was paid to a number of factors to ensure proper measurements were recorded, which thereby minimized errors and uncertainties (e.g. the introduction of additional experimental variables)

(1) Alignment of the pump and probe beam spots on the sample were routinely checked prior to a measurement set to guarantee that the probe beam was centralized and fully covered by the pump beam.

(2) To prevent any possible interference from scalar effects taking place during vectoral effects, the sample was initially photodarkened to saturation prior to measuring any photoinduced dichroism. This was done more as a precaution because as previous reports by Lyubin and Tikhomirov [55] as well as Fritzsche [58] indicate the two processes are independent of each other.

(3) Measurements at the different pump intensities were performed on the same spot to avoid introducing effects due to local variations in the sample structure.

(4) To prevent causing any irreversible changes in the sample, measurements were started at the lowest pump intensity and increased to the maximum pump intensity.

Measurements were then transcribed again at a few lower intensities revealing identical results to the values recorded prior to the maximum pump intensities. This was not a great concern as the pump intensities used in a study for photomelting [63] were three orders of magnitude more than what we applied. Furthermore, the intensities we had used were even less than ones employed in similar studies in other works [64, 65] where they also found no irreversible effects introduced with their high pump intensities.

A typical photoinduced dichroism measurement set at a given pump intensity is illustrated in Figure 6-1. To change the orientation of the anisotropy, the polarization direction of the inducing beam is rotated by 90°. Note that every time anisotropy 'saturation' was attained (after 30 minutes on Figure 6-1) the polarization direction of the inducing beam was rotated until 'saturation' was reached again at this new orientation (60 minutes on Figure 6-1). Each such 30 minute period is called a *cycle*. Hence, Figure 6-1 shows 12 complete cycles of 30 minute intervals which we call a *measurement set*. Due to the inverse relationship of pump intensity to saturation time

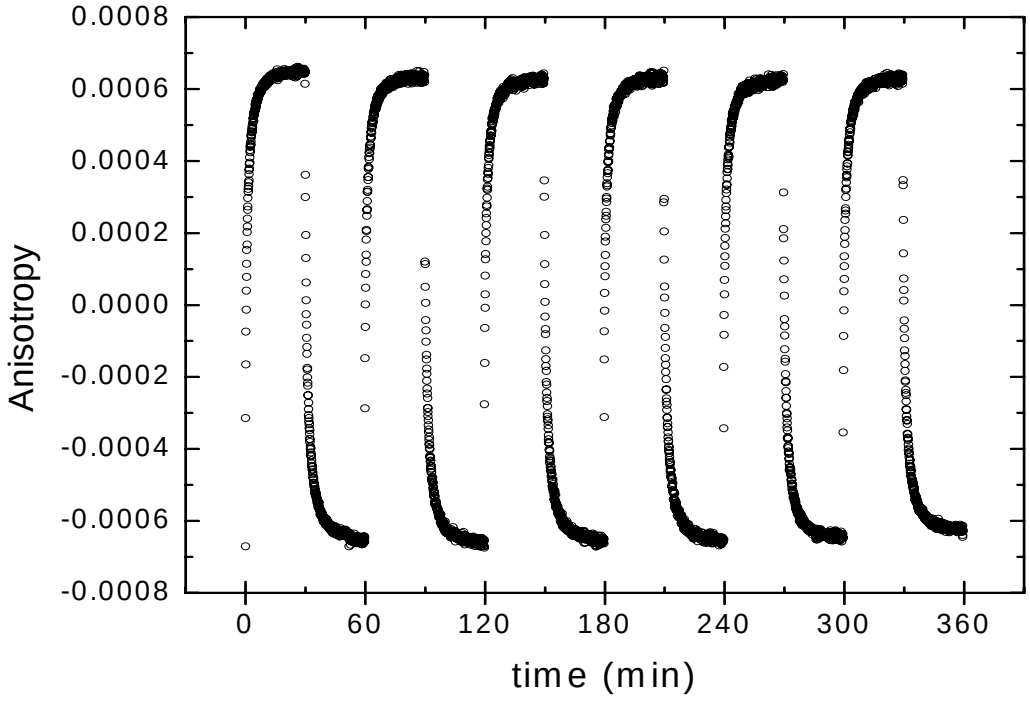

Figure 6-1: Typical Time dependence measurement set of the photoinduced dichroism in As_2Se_3. There are 12 complete cycles shown, with each cycle lasting 30 minutes for this pump intensity.

and the fact that the lowest pump intensities used were very weak, the measurement cycle times required to determine a time constant, τ, and stretched exponent, β, varied from 30 minutes to 2 hours. Compounding this measurement time length was the fact that our pump beam was at an angle to the sample. As it was shown in Section 4.3.2 the intensity of the pump beam was different for the vertical and horizontal polarization orientations. What this implies is that for any given intensity setting, as determined by the neutral density filter, yielded two intensity measurement sets, which correspond to the vertical and horizontal pump beam polarization directions. Also, in order to procure accurate data of the photoinduced dichroism kinetics, several buildup cycles of photoinduced dichroism were recorded in order to obtain a small sampling at each pump intensity level. Typically 6 complete cycles at a pump intensity and polarization direction were used; hence, the need for 12 cycles in any given measurement set.

The cycles were then separated out of the measurement set and grouped with the respective polarization, horizontal (positive anisotropy orientation) and vertical (negative anisotropy direction). Each cycle was then fitted using the previously discussed stretched exponential fitting function

$$A(t) = A_{sat} + (A_0 - A_{sat})\, e^{-\left(\frac{t}{\tau}\right)^{\beta}} \tag{6.1}$$

where A_{sat} is the anisotropy saturation value, A_0 is the initial anisotropy start value, τ is the time constant for the anisotropy to reach 63.6% of the saturation level and β is the stretch exponent. The result was a total of 6 sets of A_{sat}, τ and β fit parameters where standard sample statistics formulas were used for analysis. The mean value, was calculated from

$$\bar{x} = \frac{\sum_{i=1}^{N} x_i}{N} \tag{6.2}$$

where $\bar{x}$ is the average or mean value, x_i the i-th data value and N the number of data points.

The standard deviation was calculated from

$$s = \sqrt{\frac{\sum_{i=1}^{N} \left(x_i - \bar{x}\right)^2}{N-1}} \tag{6.3}$$

where s is the standard deviation.

The standard error from

$$s_e = \frac{s}{\sqrt{N}} \tag{6.4}$$

where s_e is the standard error of the mean. Tables 6-1 and 6-2 show the values of the fit parameters and calculated values of the measurement set depicted in Figure 6-1.

Table 6-1: Fit parameter results from Figure 6-1 for the horizontal polarization. Note only the odd numbered cycles are listed. ($N = 6$).

Horizontal Polarization			
HeNe Laser Pump Intensity = 1.164 mW/mm^2			
Cycle	A_{sat}	τ (secs)	β
1	0.001322	43.97	0.4929
3	0.001284	42.70	0.4920
5	0.001305	40.97	0.4824
7	0.001282	44.09	0.4962
9	0.001278	44.70	0.5051
11	0.001279	44.95	0.5063
Average	0.001292	43.56	0.4958
Standard Deviation	0.000018	1.494	0.0089
Error	0.000007	0.610	0.0036

Table 6-2: Fit parameter results from Figure 6-1 for the vertical polarization. Note only the even numbered cycles are listed. ($N = 6$).

Vertical Polarization			
HeNe Laser Pump Intensity = 0.970 mW/mm^2			
Cycle	A_{sat}	τ (secs)	β
2	0.001292	73.08	0.5952
4	0.001296	68.63	0.5753
6	0.001284	64.97	0.5453
8	0.001307	63.30	0.5351
10	0.00127	63.35	0.5458
12	0.001263	65.47	0.5607
Average	0.001286	66.47	0.5596
Standard Deviation	0.000016	3.779	0.0224
Error	0.00007	1.543	0.0091

Even though it is well known that the photoinduced dichroism kinetics follows a stretched exponential buildup [57, 64, 65] we also examined fitting the buildup to a simple exponential function.

$$A(t) = A_{sat} + (A_0 - A_{sat})\, e^{-\left(\frac{t}{\tau}\right)} \tag{6.5}$$

Looking at Figure 6-2 one can clearly see that a fit with the simple exponential function (blue curve) is very poor but the stretched exponential function (red curve) follows the measured data very closely. In order to determine how well the fit parameters actually fit the curve we solved the stretched exponential equation (6.1) in terms of time.

$$-\ln\left(\frac{A(t) - A_{sat}}{A_0 - A_{sat}}\right) = \left(\frac{t}{\tau}\right)^{\beta} \tag{6.6}$$

Calculating the left side of the equation using the initial anisotropy value, A_0, the measured anisotropy, $A(t)$, and the fit parameter for the saturated anisotropy value, A_{sat}. Then plotting this value against $(t/\tau)^{\beta}$ should yield a straight line if the parameters are accurate, see Figure 6-3 (a). Any curving in this plot indicates a deviation from the

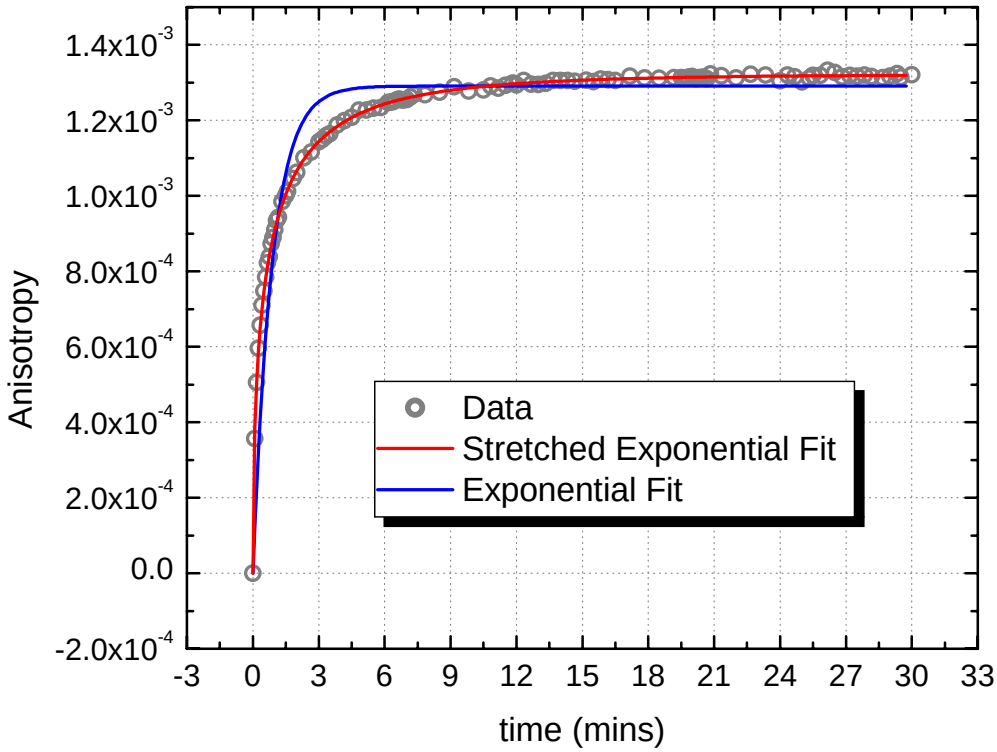

Figure 6-2: Time dependence of the dichroism after rotation of the pump beam's polarization by 90º. The blue curve is an exponential fit to the data and the red curve is a stretched exponential fit.

"true" stretched exponential behavior. For completeness, the simple exponential parameter fit plot was also carried out, see Figure 6-3 (b). As one can clearly see from Figure 6-3 (b), the plot is not a straight line, and the relationship is not a simple exponential.

Another important parameter is the anisotropy saturation. Strictly speaking, any exponential time function, whether it is simple or stretched, saturates only after infinite time. This brings up the question of how long does one need to take measurements to be satisfied that the anisotropy is sufficiently saturated. From calculating the fit parameters for different saturation times we found that if the slope of the tail end of the photoinduced anisotropy buildup (refer to the 27 to 30 min time section of Figure 6-2) was less than 3×10^{-6} min^{-1}, then the error introduced by calculating the fit parameters at this point was less than the error on the mean of the fit parameters.

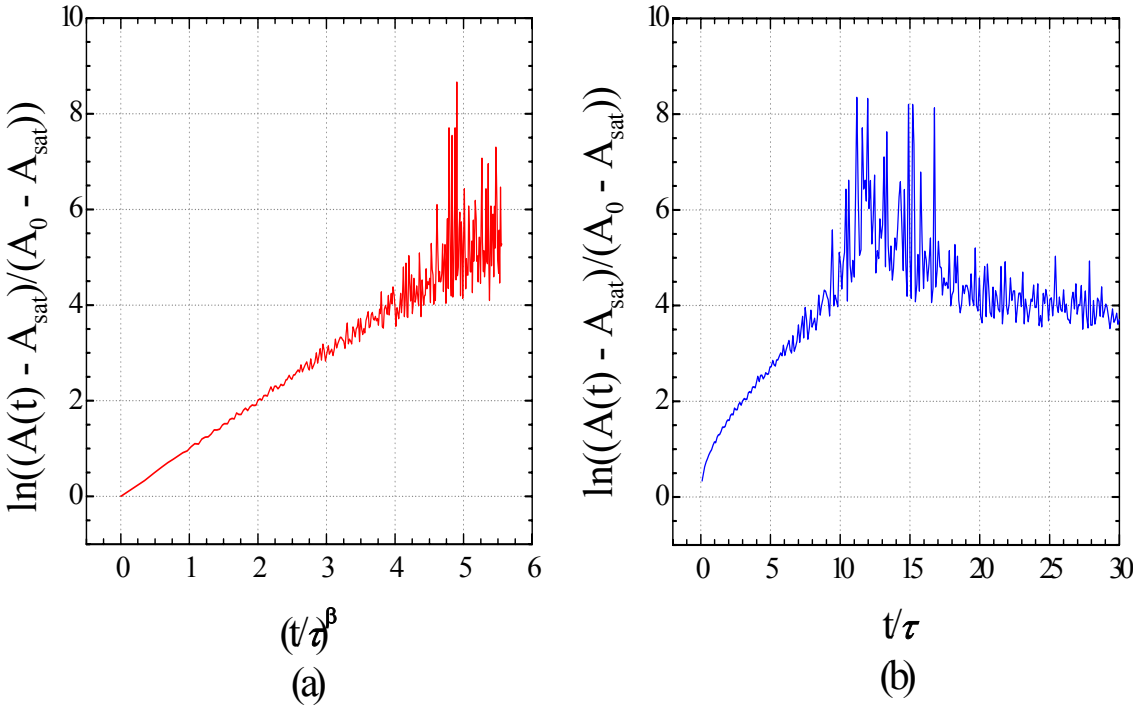

Figure 6-3: Plots showing fit of parameters for Stretched Exponential Equation (6.1) with $\beta \approx 0.587$ (a) and the Simple Exponential Equation (6.5) (b).

The sample thickness is also an important factor in the analysis of photoinduced dichroism experiments. A transmission spectrum of the sample was recorded using a PerkinElmer Lambda 900 UV/VIS/IR Spectrometer to extract the film thickness. Figure 6-4 shows the spectral response from an 8000 Å thick film, one of the samples used in our experiments. The Swanepoel method [66] is widely used to measure the refractive index and the thickness of thin optical films. It is based on reflected light from the two surfaces of the film interfering so that, as the wavelength is changed, the transmission spectrum exhibits peaks and troughs as in Figure 6-4. In the present work, the sample thickness was calculated from the application of the Swanepoel method to the oscillations in the transmission spectrum with respect to wavelength.

It is important to evaluate the effect of the sample thickness on the photoinduced dichroism measurements, and the effect on the induced dichroism kinetics deduced from such measurements. A major part of our research deals with determining the

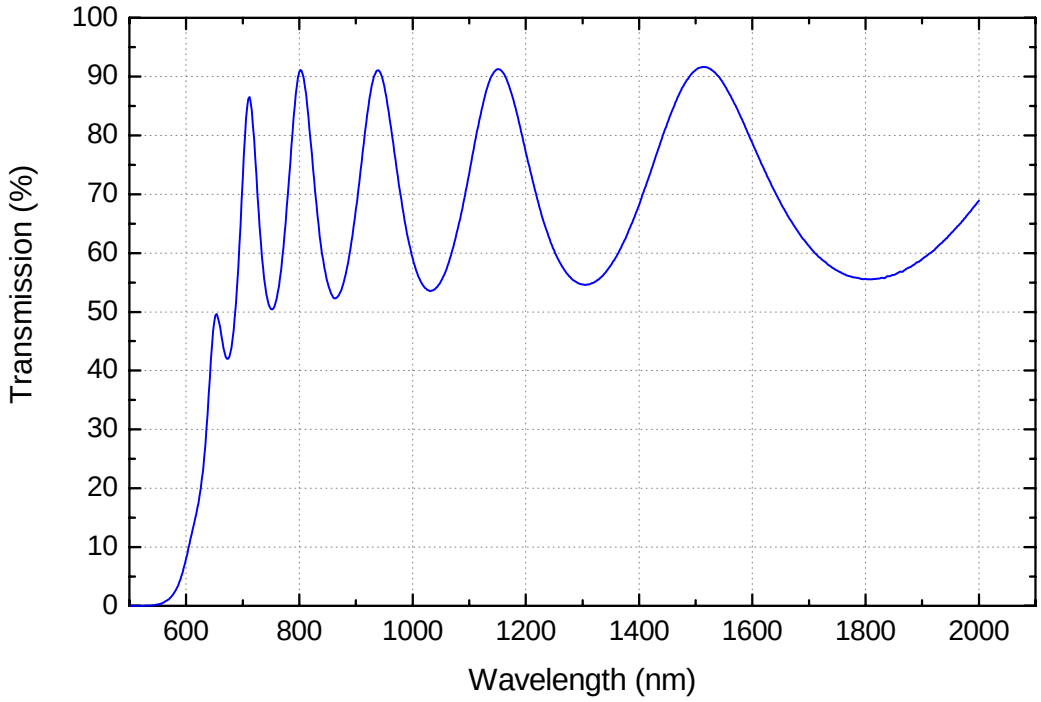

Figure 6-4: Spectral Response of an As_2Se_3 thin film sample, 0.8 μm thick.

photoinduced dichroism kinetics as a function of intensity. Obviously, if photons are being absorbed then the pump beam intensity is decreasing as it travels through the material. The intensity of a light beam, *I*, after it travels a distance *x* into a bandgap material is given as [50]

$$I(x) = I_0 e^{-\alpha x} \tag{6.7}$$

where I_0 is the intensity of the light at the surface and α is the absorption coefficient, a material property which is dependent on the photon energy, *hv*. This is known as the Beer-Lambert law and basically states that the transmitted light intensity decreases exponentially as the beam passes through the material. The distance over which 63% of the photons are absorbed is called the penetration depth, δ, which is defined as,

$$\delta = \frac{1}{\alpha} \tag{6.8}$$

The photon energy for a helium neon laser with a wavelength, λ = 632.8 nm is

$$hv = \frac{hc}{q\lambda} = \frac{\left(6.626\times10^{-34}\,\text{Js}\right)\left(2.9979\times10^{8}\,\text{m/s}\right)}{\left(1.60218\times10^{-19}\,\text{C}\right)\left(632.8\times10^{-9}\,\text{m}\right)} \cong 1.959\ \text{eV}$$

Extrapolating the $(\alpha hv)^{\frac{1}{2}}$ value from the photodarkened As_2Se_3 glass Tauc plot in Figure 6-5 at the photon energy for a helium neon laser yields

$$(\alpha hv)^{\frac{1}{2}} = 198\ \text{cm}^{-\frac{1}{2}}\text{eV}^{\frac{1}{2}} \tag{6.9}$$

By rearranging equation (6.9) the absorption coefficient, α, for photodarkened As_2Se_3 glass is

$$\alpha = \frac{\left(198\ cm^{-\frac{1}{2}}\text{eV}^{\frac{1}{2}}\right)^2}{hv} = \frac{198^2\,\text{cm}^{-1}\text{eV}}{1.959\ \text{eV}} \cong 20.01\times10^{3}\,\text{cm}^{-1} \text{ or } 2.001\times10^{6}\,\text{m}^{-1}$$

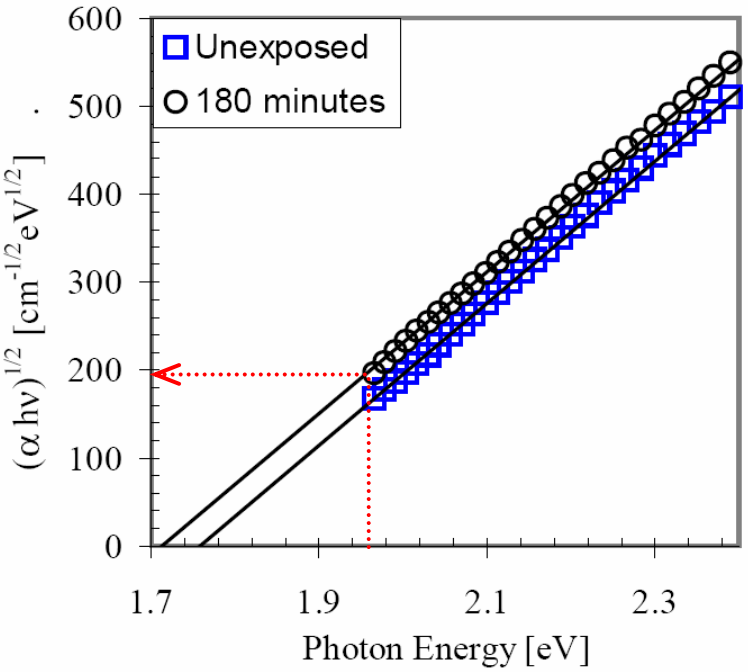

Figure 6-5: Tauc plot showing the change in absorption and photon energy for unexposed (blue box) and photodarkened (black circles) As_2Se_3 glass (From [61]).

Therefore, the penetration depth for photodarkened As_2Se_3 glass is

$$\delta = \frac{1}{\alpha} \cong \frac{1}{2\times10^{6}\,\mathrm{m}^{-1}} = 0.5\ \mu\mathrm{m}$$

The samples used in this research were thin films of amorphous As_2Se_3 of thicknesses from 0.25 μm to 1.93 μm, covering roughly $\delta/2$ to 4δ.

6.2.1 Time Constant, τ, and Stretched Exponent, β

All measurements for photoinduced dichroism were made at room temperature using a helium neon laser (λ = 632.8 nm) as the inducing light source. The intensity for the laser was adjusted by using a variable neutral density filter. Inducing light intensities ranged from 77 μW/mm^2 to 1.18 mW/mm^2. In order to circumvent any permanent structural changes to the sample, the sequence of intensity measurements were done from the lowest intensity to the highest. The repeated measurements at the lowest intensities, found the results to be the same as the measurements made prior to the higher intensity. This was done to check that the higher intensity level did not photostructurally change the sample. To avert introducing any structural differences within the sample, all the measurements for the different light intensities were performed over the same area. Care was also taken to fully photodarken the spot prior to starting the photoinduced dichroism measurements in order to prevent any scalar effects taking place during vectoral effects.

Figure 6-7 shows the time constant, τ, as a function of inducing light intensity. From this plot we see that there is a reciprocal relationship between the pump intensity and τ, in that a shorter time is required to reach saturation with a higher pump intensity. This is in agreement with Adriaenssens et al. [67], where they state that reducing the intensity by a factor of ten decreases the kinetics by a factor of ten. This is more clearly illustrated in Figure 6-6 where a plot for the rate of change, $1/\tau$, to inducing light intensity is displayed. The blue line is a linear regression fit to the data using least squares as the fit error. The value of the correlation coefficient, r^2, was greater than 0.9436 indicating a very good fit. Aside from the linear relationship shown, it

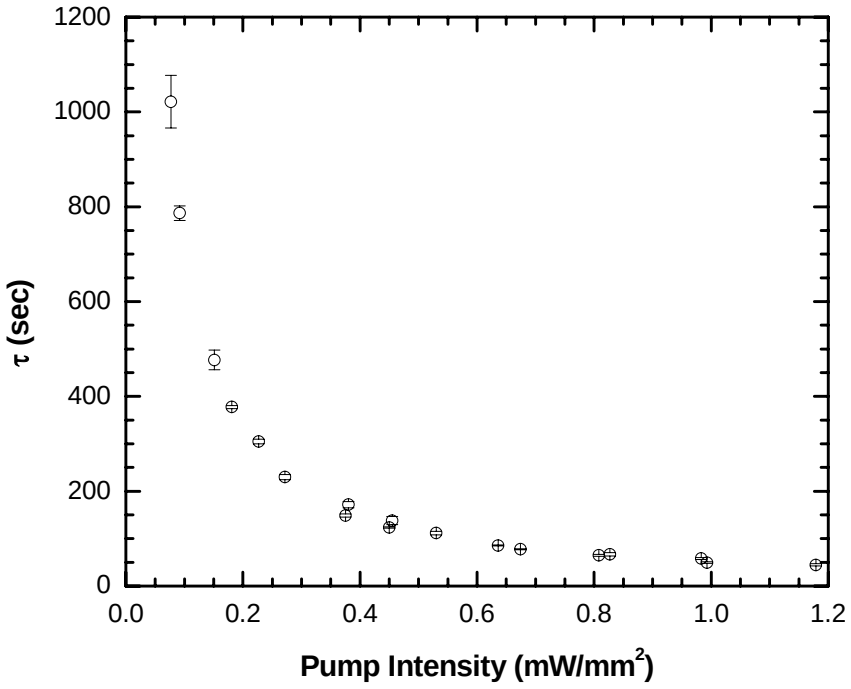

Figure 6-7: Time constant τ of the photoinduced anisotropy buildup versus pump light intensity for a 0.25 μm thick sample of As_2Se_3.

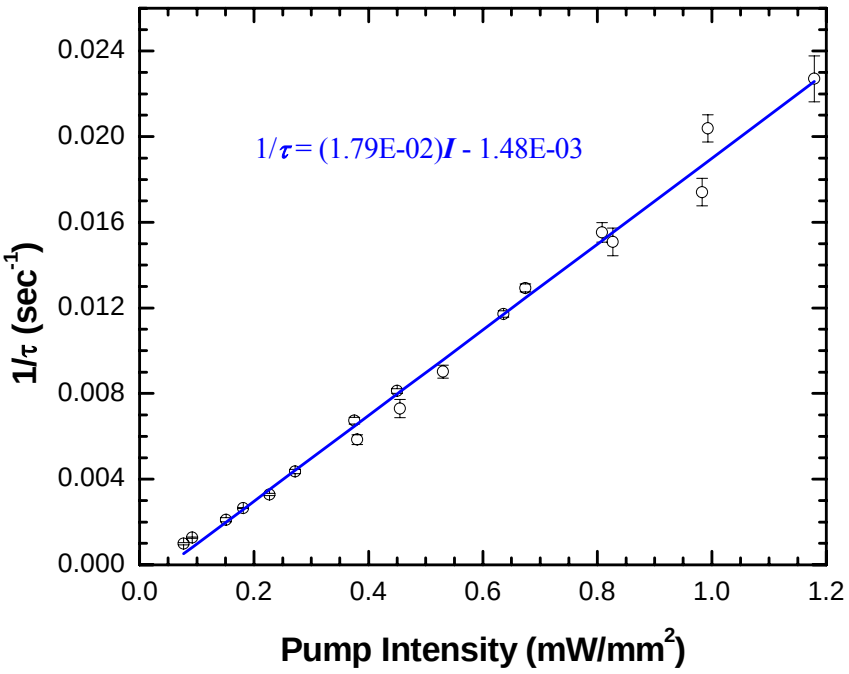

Figure 6-6: Rate of induced anisotropy, $1/\tau$, versus pump light intensity for a 0.25 μm thick sample of As_2Se_3.

should be expected that the line would pass through the origin. This only makes sense, for if there is no pump light there would be no photoinduced anisotropy buildup. The line formula for the linear regression fit is,

$$1/\tau = 1.79\times10^{-2} I - 1.48\times10^{-3} \tag{6.10}$$

where I is the pump intensity. From this we see that the $1/\tau$ intercept value has a slight offset to -0.00102 sec^{-1} from the origin. Forcing the fit through zero results in a lower correlation coefficient, $r^2 = 0.9221$, indicating a poorer fit. There are a couple of possible explanations for this offset: (a) a systematic error which has caused a shift in the data. This is the most likely explanation as the probe source is not completely unpolarized, (see Section 4.3.1 for more details). Prior to a measurement series the probe beam is measured to obtain the constants necessary to evaluate the anisotropy. A small error in this measurement would translate to a direct shift in the measured anisotropy data. (b) It is possible that the data does not fit best to a linear regression but rather some other function such as a power law or logistic dose response.

First considering a power law dependence

$$1/\tau = C(I)^n \tag{6.11}$$

where $n \approx 1.07$ is determined from the slope of a line drawn through the data points on a log log plot as shown in Figure 6-8. $C \approx 0.01677$ is a constant determined from an ideal point on the fitted line. The resulting plot of data and fitted power law curve is displayed in Figure 6-9. The correlation coefficient for this fit is $r^2 = 0.9349$. This is an improved fit from the linear relationship but as one can see from Figure 6-9 there is still a large variance between the fitted line and the data points.

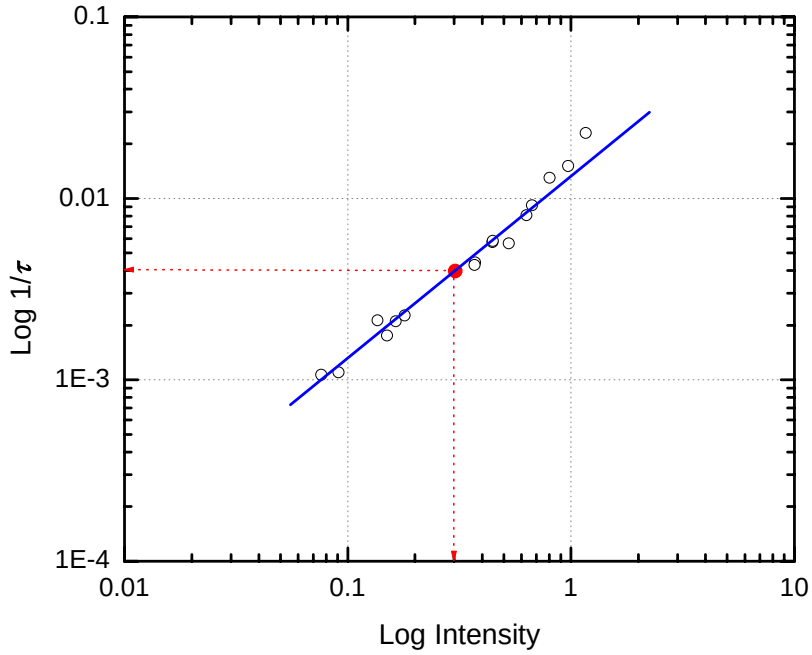

Figure 6-8: Log Log plot for rate of induced anisotropy, $1/\tau$, versus pump light intensity for a 0.25 μm thick sample of As_2Se_3.

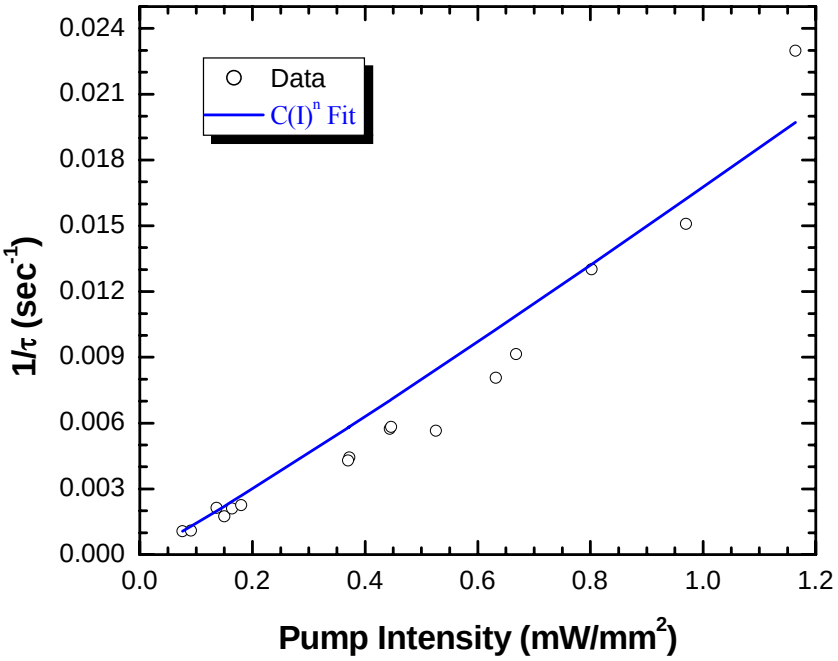

Figure 6-9: Power law curve fit to rate of induced anisotropy versus pump light intensity for a 0.25 μm thick sample of As_2Se_3.

The logistic dose response equation is

$$1/\tau = a + \frac{b}{1+\left(I/c\right)^{d}} \tag{6.12}$$

where *a*, *b*, *c* and *d* are the fit parameter constants. The correlation coefficient for this response was $r^2 = 0.9933$, indicating a much better fit to the data than the either the linear or power law relationships. Figure 6-10 shows the data fit to a logistic dose response curve (blue line) with the 95% confidence limits added (magenta lines). The fit parameter constants are listed on the graph as well. A logistic dose response curve is an asymmetric S-shaped curve that is composed of three regions: (a) the lower region starts off from the origin asymptotic to the *x* axis and then curves upward. (b) middle region is linear. (c) the upper region curves asymptotic to some saturated value. This is a statistical response [68] that has been used to characterize many chemical and photonic reactions. From this we see that the fit passes through the origin. The problem with fitting the data to this response is that we are assuming there is an upper limit to the

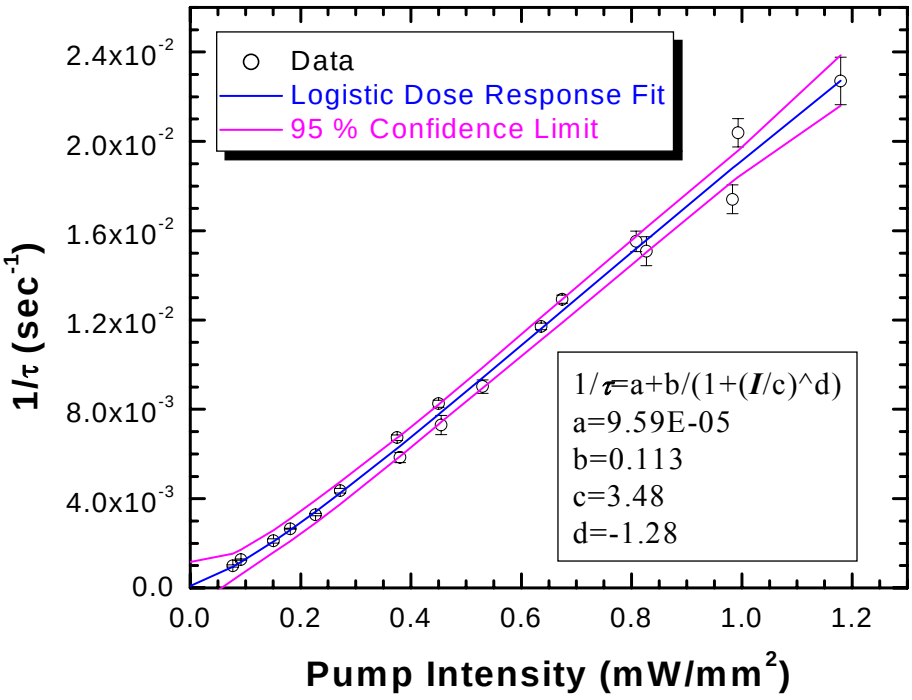

Figure 6-10: Logistic dose response curve fit to rate of induced anisotropy versus pump light intensity for a 0.25 µm thick sample of As_2Se_3.

rate that the anisotropy can be induced and that our present data has fallen into the linear region.

It should be mentioned that equation (6.12) could be expanded around the center of the data range at $I = 0.6$, we would find

$$1/\tau = 0.00062237(I - 0.6)^2 + 0.020793(I - 0.6) + 0.010678$$

On the data range from $I = 0.2$ mW/mm^2 to 1.2 mW/mm^2 the relationship is about 98% linear. This is determined by taking nonlinearity as

$$\frac{\text{Quadrative Term}}{\text{Linear Term}} = \frac{0.00062237}{0.020793}(I - 0.6)$$

which shows that it is 2% for $I = 1.2$ mW/mm^2 and 1% for $I = 0.2$ mW/mm^2. Therefore, the response is approximately linear.

Consequently, further research using higher pump intensities is required to determine which response provides the best fit.

The inverse relationship we find between the rate of induced anisotropy, $1/\tau$, and the pump intensity, I, is in partial agreement with what Hertogen [21] found. The results from Hertogen's study and ours both agree with the reciprocal relationship but where we diverge is the rate or speed that the photoinduced kinetics buildup. Namely the value for the time constant, τ, appears to be approximately 5 times faster in our measurements than his findings. Our findings show that for an inducing light intensity of approximately 1 mW/mm^2 results in a τ of about 57 seconds or 1 minute, but Hertogen's measurements show a τ of about 5 minutes. Possible reasons for this discrepancy could be related to differences in material composition, preparation conditions, and or procedures [69 − 72]. Another possible explanation is the fact that Hertogen used samples that were 2 μm thick and our sample in this example is only 0.25 μm. Referring back to Section 6.2, and the discussion on sample thickness, we found from equation (6.8) that the penetration depth was only 0.5 μm. With Hertogen using a sample that was 4 times the penetration depth means that his inducing intensity was

substantially absorbed within the sample. There is very little pump light intensity exiting Hertogen's sample, whereas in our sample there is substantial unabsorbed light intensity (see equation number (6.7)) as the pump light passed through the sample. With Hertogen's sample being four times thicker than the penetration depth, this results in a large light intensity variance as the inducing beam passes through the material. Consequently, this will draw out the anisotropy buildup time which, as stated previously in this section, is intensity dependent. To further support this theory Figure 6-11 displays the anisotropy rate change as a function of inducing intensity from a 1.93 µm film (magenta line), 0.8 µm film (red line) and the 0.25 µm film (blue line). Notice that the slope of the anisotropy rate lowers as the film thickness increases. The lower slope indicates a longer anisotropy buildup time. At a pump intensity of 1 mW/mm^2 the anisotropy buildup rate for the 1.93 µm film was approximately 3 minutes. This is closer to Hertogen's results of 5 minutes and the discrepancy between the results can be explained as differences in the material composition or preparation conditions of the samples. To further complicate these comparisons Hertogen does not mention how he had measured his inducing intensity. Therefore we can only speculate on these disagreements.

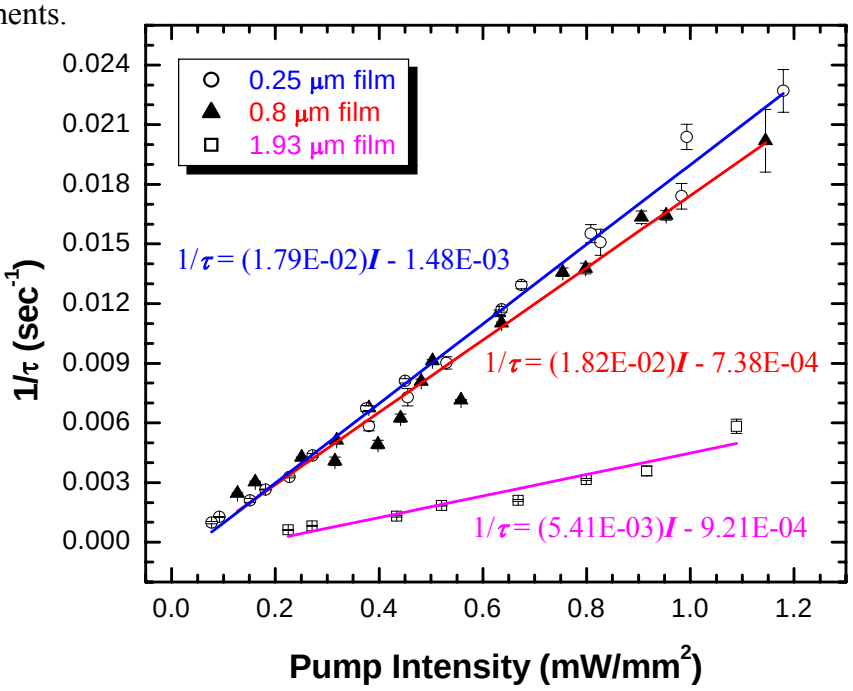

Figure 6-11: Rate of induced anisotropy, $1/\tau$, versus pump light intensity for samples of As_2Se_3 at 0.25 µm thick (open circle and blue line), 0.8 µm thick (triangles and red line) and 1.93 µm thick (open square and magenta line).

The stretched exponent, β, as a function of inducing light intensity was also studied. Figure 6-12 displays a graph of the stretched exponent, β, versus the inducing light intensity for a 0.25 μm thick As_2Se_3 sample. From this graph we see that β on average is approximately 0.6 and has a small direct dependence on the inducing beam intensity. The fact that β of equation (6.1) is far from unity, indicates that the anisotropy buildup as a function of time, $A(t)$, cannot be a standard exponential growth. The stretched exponential has been proposed to represent a summation of several exponential functions from different factors that are acting sequentially as time progresses. The mathematical description for the anisotropy buildup has been discussed by Tikhomirov [73]. In his paper, Tikhomirov sites Kolhrausch's law as a basis for this equation. He goes on to suggest that the "smallest structural elements undergo a relaxation in the early stages, and this makes it possible for the relaxation of progressively larger structural elements." This domino effect of smaller structural elements assisting progressively larger structural elements could be the basis for the sequential exponential factors. Fitting the $\beta(I)$ data in Figure 6-12 to a linear trend line reveals that there is a small positive slope to β as the intensity is increased. At lower

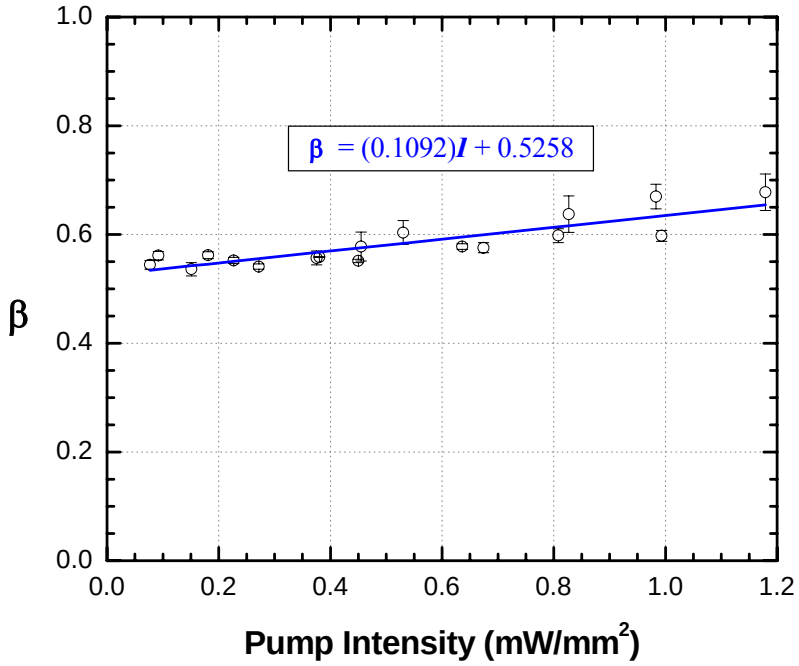

Figure 6-12: The stretching exponent, β, versus pump light intensity for a 0.25 μm thick sample of As_2Se_3.

pump intensities, the photon flux, $F\left(photons/area/sec\right)$ is smaller. Clearly this means that there are less photons to interact with the sample and as Tikhomirov pointed out in his relaxation study [73], "the relaxation kinetics of the photoinduced anisotropy in darkness depends strongly on the absolute value of the dichroism which was reached before the measurements began." If we consider that the small structural elements maybe more reactive and therefore may have a shorter lifetime in the altered structural state, which the dark relaxation kinetics suggest. Then the time between the successive exponential buildups would increase causing the β value to be even smaller, (i.e. a smaller β stretches the exponential time scale even greater) at lower pump intensities. To further support this speculation, the intercept point of $\beta = 0.5258$ as indicated by the linear regression fit line is close to the value that Tikhomirov reports [73].

The comparison of our results to a similar study by Hertogen [21] shows that the average values of β are comparable, but there are differences in the dependence of β on the intensity. Hertogen shows a negative trend to β as the intensity increases. It could be argued that the difference is due to the fact that he used higher intensities for the pump beam. As stated previously our maximum pump intensity is comparable to Hertogen's minimum intensity. Yet another reason could be due to the differences in the sample thickness. Our sample was only 0.25 μm thick, half of the penetration depth (see equation (6.8)), whereas Hertogen's sample was 2 μm thick, 4 times the penetration depth. The difference in sample thicknesses appears to be the more likely cause. Plotting the $\beta(I)$ data for our 0.8 μm thick sample as shown in Figure 6-13 supports this conjecture. As the graph shows the average β value is comparable to the other thickness measurements and the fitted trend line displays the negative slope that Hertogen found. What is disturbing is the fact that this appears to contradict the earlier speculation by Tikhomirov. Where an inference was made that the small structural elements maybe more reactive and therefore may have a shorter lifetime in the altered structural state. This could cause the time between the successive exponential buildups to increase resulting in the β value to be even smaller and therefore stretch the exponential time scale even greater at lower pump intensities. Because the light intensity exponentially decays as it passes through a material (see equation number (6.7)) one would expect that

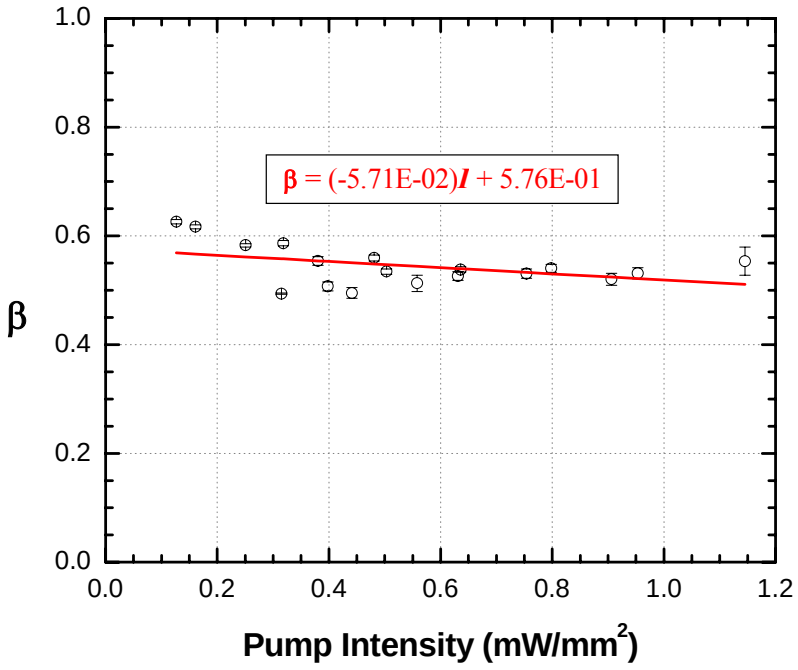

Figure 6-13: The stretching exponent, β, versus pump light intensity for a 0.8 μm thick sample of As_2Se_3.

the stretching exponent value to decrease as the sample thickness increases. Clearly more research is needed to clarify what mechanisms are involved in these photoinduced phenomena.

6.2.2 Reversibility and Saturation Level, A_{sat}

We have studied the reversibility of linear dichroic buildup and subsequent annihilation and reorientation in the orthogonal direction of an As_2Se_3 thin film. Figure 6-14 clearly illustrates this reorientation phenomenon. On this plot the arrows indicate the polarization orientation for each cycle shown. The first few cycles (left side) are from the lowest pump intensity, where the buildup time was slowest. This required the pump polarization orientation to be present for a 2 hour interval before changing to the orthogonal polarization direction. The last 3 cycles (right side) are from the highest pump intensity measurements, where only a half hour buildup time interval was needed. Note the split in the horizontal scale axis, which denotes the exposure time of the film from the beginning of this pump intensity dependence measurement series.

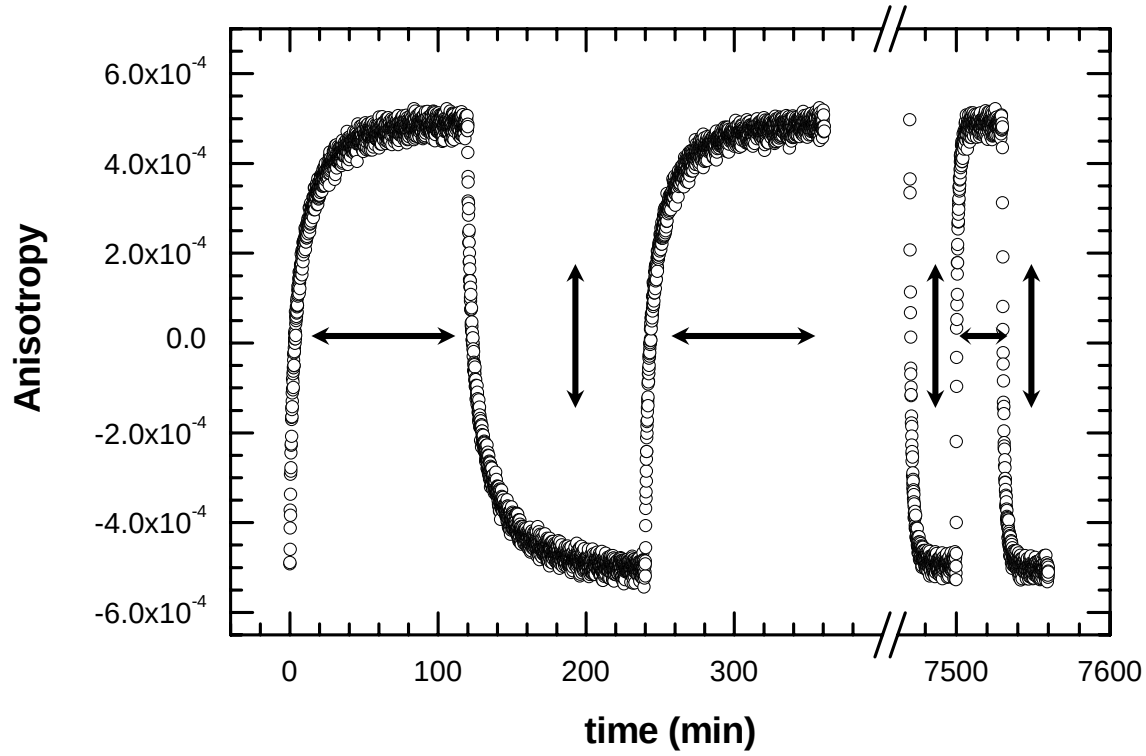

Figure 6-14: Reversibility of the photoinduced linear dichroism in a 0.25 μm thick film of As_2Se_3. The arrows indicate the direction of the pump beams polarization. The first 3 cycles are from the lowest inducing intensity (i.e. long exposure time). Note the split in the horizontal axis. This is because the last few cycles are after 100 orientation changes. Also they are at the highest pump intensity used and therefore require shorter cycle times.

Consequently, these last 3 cycles are after 85 inducing cycles or orthogonal polarization rotations. The interesting aspect to observe is the fact that the photoinduced anisotropy levels are virtually identical from the start to the end of the measurement series. This is in agreement with previous reports [51, 55] where hundreds of cycles were measured and showed no signs of fatiguing in the photoinduced anisotropy level.

Plotting a comparison of anisotropy saturation, A_{sat}, to inducing light intensity for the 0.25 μm thick sample, as shown in Figure 6-15, we see that the saturation level of anisotropy is basically independent of the inducing light intensity. Fitting the data to

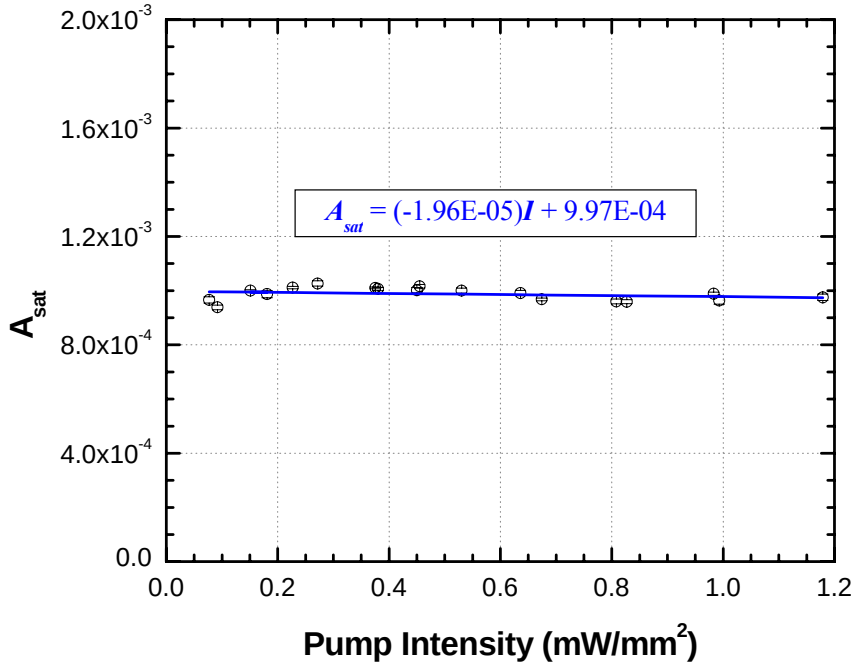

Figure 6-15: Photoinduced anisotropy saturation level versus inducing light intensity for a 0.25 μm thick As_2Se_3 sample.

linear regression shows that there could be a very weak dependence of anisotropy saturation on the inducing light intensity. This is indicated by a very small negative slope to the linear regression line. These results are in direct agreement with the findings of Hajtó et al. [74] and Kimura et al. [45], but contrary to the report from Hertogen [21]. Hertogen found a 53% decrease in anisotropy saturation over an intensity range of 1 – 15 mW/mm^2 for As_2Se_3. In Hertogen's defense it should be noted that his minimum inducing light intensity was the same as our maximum intensity level. Also the sample thickness in his research was 2 μm as compared to our 0.25 μm. The result of these two differences maybe factors for the cause of the disagreement. To fully understand this discrepancy more definitive research will have to be done.

6.2.3 Effect of Film Thickness

Film thickness plays an important role in the research of light absorption in materials due to the fact that the light intensity decreases exponentially with distance

into the sample following the Beer-Lambert law [50]

$$I_{(x)} = I_0 e^{-\alpha x} \tag{6.7}$$

where I_0 is the intensity of the light at the surface of the material and α is the absorption coefficient, a material property which is dependent on the photon energy, hv. The effective depth of the propagating beam is the distance into the material which reduces the intensity by 63%. This is known as the penetration depth, δ, which is defined as,

$$\delta = \frac{1}{\alpha} \tag{6.8}$$

Since α is dependent on the photon energy, means that it is wavelength dependent. The penetration depth for the helium neon inducing laser (λ = 632.8 nm) used in this research is,

$$\delta = \frac{1}{\alpha} \cong \frac{1}{2\times 10^6\,\mathrm{m}^{-1}} = 0.5\ \mu\mathrm{m}$$

In Chapter 5, Section 5.3 a relationship for relative anisotropy, A, was explained between the definition of dichroism, $(\alpha_\perp - \alpha_{//})L$ and the measured quantities, $I_\perp$ and $I_{//}$. Where L is the thickness, α is the absorption coefficient of the sample, I the transmitted probe intensity and the subscripts, $\perp$ and //, respectively denoting the direction of polarization perpendicular and parallel to the inducing beam's polarization orientation. The result was the following equation,

$$A = \frac{I_{//} - I_\perp}{(I_{//} + I_\perp)/2} = (\alpha_\perp - \alpha_{//})L$$

This equation states that the amount of anisotropy is proportional to the sample thickness. It should be mentioned that the above equation assumes that the incident probe beam as no polarization. In practice, the incident beam will have some inevitable polarization whose effects on the measurements of anisotropy were discussed in Section 5.4. Figure 6-16 shows the saturated anisotropy level, A_{sat}, for samples from

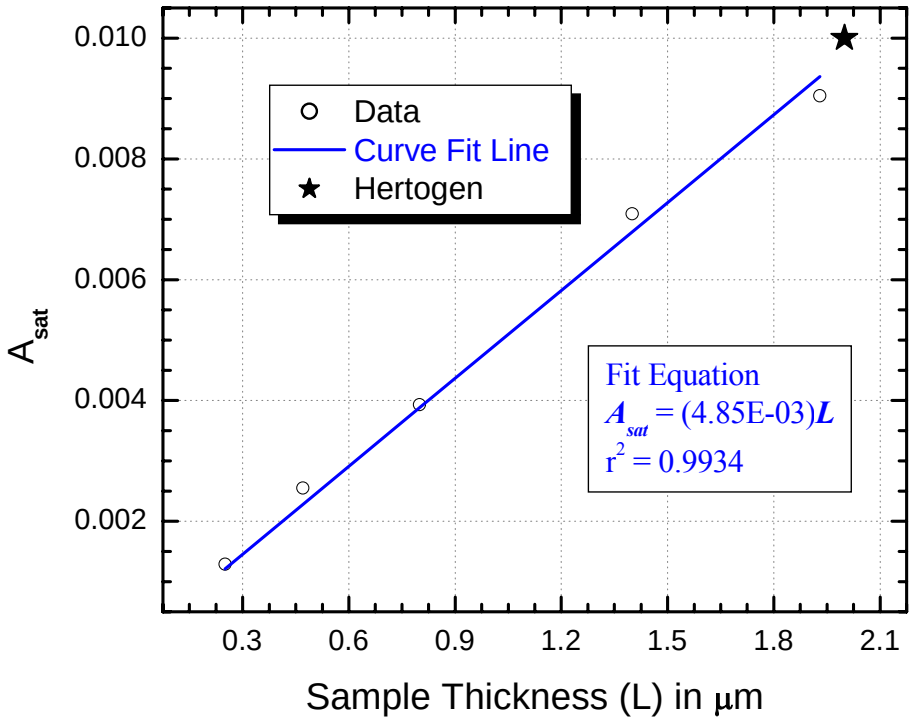

Figure 6-16: Anisotropy saturation versus sample thickness, L. The blue line is the $A_{sat}(L)$ data fit to a line equation (lower right corner of graph). The star point is from Hertogen's data [21].

0.25 to 1.93 μm thickness. The line fit to the $A_{sat}(L)$ data suggests that the relationship could be linear as the anisotropy equation implies. The correlation coefficient for this fit was close to 1 at $r^2 = 0.9934$, indicating a very good fit. The five pointed star indicates the data from Hertogen's report [21]. As one can see it is right in line with the linear fit to our data.

The correlation of the stretching exponent, β, to sample thickness, L, was also studied and found to have a few interesting results. First referring to Figure 6-17 we find that for samples thinner than the penetration depth of 0.5 μm β has a direct relationship with thickness, which appears to peak at around 0.5 μm. Whereas at thicknesses greater than 0.5 μm β has an inverse relationship. The decrease in β as the sample thickness increases stands to reason because of the Beer-Lambert law (equation number (6.7)). This law tells us that the light intensity is decreasing exponentially as the

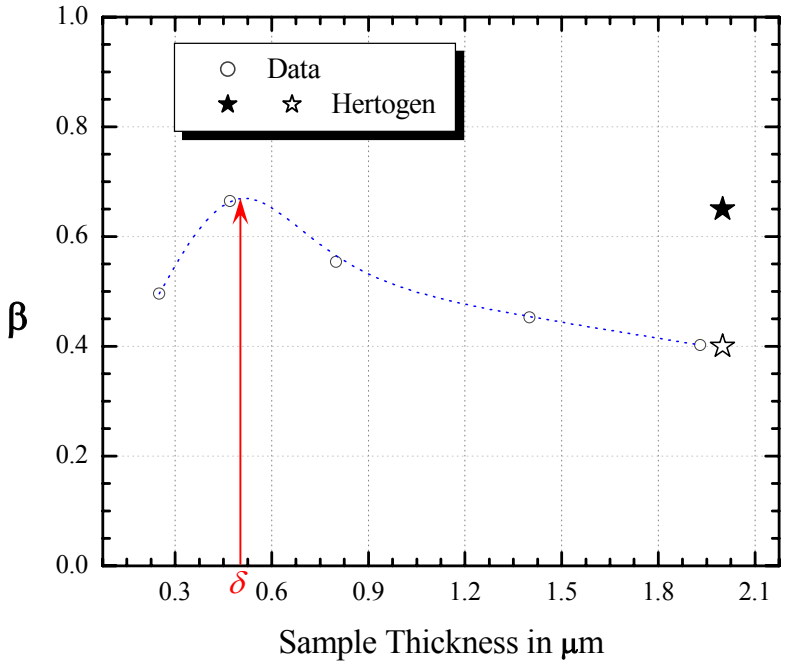

Figure 6-17: The stretching exponent, β, versus sample thickness, L, for As_2Se_3. The star points are derived from Hertogen's data [21]. The solid star is raw data and the hollow star is modified for intensity.

beam propagates through the sample. As previously shown in Section 6.2.1, the time required to buildup the photoinduced dichroism to saturation increased as the intensity of the inducing source decreased. Bearing in mind, that the stretched exponential function is basically a summation of several exponential functions acting sequentially as time progresses. Then applying the conjecture made in Section 6.2.1, which basically states that smaller structural elements could be assisting progressively larger structural elements form the different exponential factors that are acting successively as time advances. As well considering that these small structural elements maybe more reactive and therefore may have a shorter lifetime in the altered structural state than the time between photon stimulation. Then the period amid the successive exponential buildups would increase causing the β value to be even smaller, (i.e. a smaller β stretches the exponential time scale even greater) as the sample thickness increases, which causes a decrease in the intensity of the inducing beam propagating into the material.

As for the direct relationship for samples thinner than the penetration depth it is speculated that there is not enough material for the inducing beam to react with and hence very few photons become absorbed. With fewer photons being absorbed then the efficiency is reducing and consequently the change in structural units do not occur as rapidly.

The two star points indicate data derived from Hertogen's thesis [21]. The solid star is the β value from reading off of Hertogen's graph at the same intensity we used to plot Figure 6-17. The fact that Hertogen does not mention how he has measured his intensity and that we found many discrepancies for intensity dependent values made me scrutinize his intensity dependent graphs. From this an estimation of how he determined his intensity was made that fit to not only these reports but other studies as well. Then the second β point, hollow star, was plotted using an estimation of how Hertogen determined his intensity. This point is more consistent with our measurements.

6.3 Summary

The photoinduced anisotropy kinetics were measured in as-deposited amorphous As_2Se_3 thin films with thicknesses from 0.25 to 1.93 μm at various inducing light intensities. The experimental results were analyzed and compared to previous reports. It was shown that the experimental appartus can accurately measure a small induced dichroism and follow its evolution over time. As well, various mathematical relationships were presented as an introductory means of describing some aspects of the photoinduced kinetics.

As with other studies [51, 55], we found that the orientation of photoinduced dichroism for an As_2Se_3 thin film sample is totally reversible without any measurable fatiguing in the anisotropy level, and could possibly continue indefinitely. From these results, we confirmed the findings of Hajtó et al. [74] and Kimura et al. [45] that the saturation level of anisotropy, A_{sat}, is independent of the inducing light intensity. The experiments show that both the photoinduced dichroism and the kinetics depend on the thickness of the film.

The anisotropy buildup kinetics was also studied and confirmed the findings of other reports [21, 57, 73], which showed the evolution of photoinduced dichroism follows a stretched exponential curve as opposed to a simple exponential. The time required to achieve saturation was shown to be inversely proportional to the pump intensity, which is in agreement with previous studies [21, 67]. We also found that the dependence of the rate of photoinduced dichroism buildup, $1/\tau$, and inducing light intensity more closely obeys a logistic dose response (see Figure 6-10) than a simple straight line. This was assuming of course that the time for inducing the anisotropy has a finite limit and that our results were falling into the linear region of this response. In addition, it was demonstrated that an inverse relationship exists between $1/\tau$ and the sample thickness. This was explained to be due to an exponential decrease in the transmitted pump light intensity as per the Beer-Lambert law more pump light photons are absorbed in thicker samples.

The stretched exponent, β, was displayed to have only a relatively small dependence on the inducing light intensity as other reports [21] have also found. In addition, we showed that β also has a small dependence on sample thickness. Both of these dependencies could be explained using the ideas of Tikhomirov [73] and the Beer-Lambert law.

Chapter 7

Conclusions and Recommendations

7.1 Introduction

The purpose of this research was not only to set-up a photoinduced anisotropy apparatus but to use the latter to investigate the nature of photoinduced dichroism in thin amorphous As_2Se_3 films.

The photoinduced anisotropy kinetics were measured in as-deposited amorphous As_2Se_3 thin films with thicknesses from 0.25 μm to 1.93 μm at various inducing light intensities. Several aspects from these measurements were analyzed for comparison with other work;

- Time constant, $\tau(I)$, as a function of inducing light intensity.
- Stretching exponent, $\beta(I)$, as a function of inducing light intensity.
- Anisotropy saturation, $A_{sat}(I)$, as a function of inducing light intensity.
- And dichroism reversibility

In addition to these comparisons, results were presented with regards to anisotropy saturation, $A_{sat}(L)$, as a function of sample thickness, as well as the stretching exponent, $\beta(L)$, as a function of sample thickness.

7.2 Photoinduced Dichroism Study

The photoinduced anisotropy kinetics were measured in as-deposited amorphous As_2Se_3 thin films with thicknesses from 0.25 μm to 1.93 μm at various inducing light intensities. The experimental results were analyzed and compared to previously published papers to obtain a better characterization of the nature of photoinduced

dichroism in As_2Se_3. The data showed that this experimental apparatus can accurately measure a small induced dichroism and follow the progressive buildup over time.

As with other studies [21, 64, 73] we found that the anisotropy buildup kinetics followed a stretched exponential behavior and that there exists an inverse relationship between the pump intensity and the time constant, τ. This is in agreement with Adriaenssens et al. [67], where they state that reducing the intensity by a factor of ten increases the anisotropy buildup time by a factor of ten. It was also shown that the $\tau(I)$ relationship more closely followed a logistic dose response (Figure 6-10) than a simple straight line or power law relationship. This was assuming of course that the induced anisotropy has a finite time limit and that our results were falling into the approximately linear region of this asymmetric S-curved response.

A comparison of our photoinduced kinetic results was also made to Hertogen's Ph. D. thesis [21]. Hertogen's study and ours both agree with the reciprocal relationship between the time constant, τ, and pump intensity, I, but we differ on the value of the time constant. Our findings indicated a time constant that was approximately 5 times faster than Hertogen's value. Some possible reasons for this discrepancy could be related to differences in the material composition, preparation conditions, and or procedures [69 – 72]. However, the most likely explanation was the fact that Hertogen used samples that were 2 μm thick and ours for this measurement was only 0.25 μm. The Beer-Lambert law states the light intensity in a material will exponentially decay as it passes through the sample. The latter leads to a large light intensity variation in the sample as the inducing beam passes through the material and consequently will draw out the anisotropy buildup time. This was better displayed when we plotted the rate of anisotropy build up as a function of inducing light intensity (Figure 6-11), where it was shown, that as the sample thickness increases, the slope of the photoinduced dichroism kinetics decreases, indicating a longer buildup time for a given intensity.

The stretched exponent, β, was found to be approximately 0.6, which is a comparable value to those reported in other papers [21, 73]. It was also found that β has a slight dependence on the inducing light intensity. If the sample thickness was less

than the penetration depth this relationship was proportional but with a sample thickness greater than the penetration depth this resulted in an inverse relationship. The cause of this was explained using the Beer-Lambert law and Tikhomirov's speculation that smaller structural elements assist larger structural elements in the anisotropy process.

Our findings demonstrated that the anisotropy orientation could be changed indefinitely as we found that even after 100 orientation changes the anisotropy saturation had no measurable fatiguing. This was in complete agreement with the studies by Lyubin [55] and Kósa [51]. The anisotropy saturation was also found to be independent of the inducing light intensity, which is in direct agreement with the findings of Hajtó et al. [74] and Kimura et al. [45], but in contrast to the report from Hertogen [21]. This disagreement with Hertogen could be explained by the fact that his minimum inducing light intensity was the same as our maximum intensity level and also the sample thickness in his research was 2 μm as compared to our 0.25 μm.

7.3 Effect of Film Thickness

The definition of dichroism $A = (\alpha_{\perp} - \alpha_{//})L$, suggests that the amount of dichroism is linearly proportional to the sample thickness. The data that we have collected and analyzed strongly agrees with the linear relationship between sample thickness and the amount of induced anisotropy. Fitting our data for a range of thicknesses from 0.25 μm to 1.93 μm to a line had a correlation coefficient of r^2 = 0.9934. This is very close to a perfect fit which has an $r^2 = 1$.

The correlation of the stretching exponent, β, to sample thickness, L, was found to have an inverse relationship, that is β decreases as the sample thickness increases. This stands to reason once again because of the Beer-Lambert law, which causes a decrease in the intensity of the inducing beam propagating into the material. As previously discussed, the time required to buildup the photoinduced dichroism to saturation was found to increase as the intensity of the inducing source was decreased. The stretched exponential has been proposed to represent a summation of several exponential functions from different factors that are acting sequentially as time progresses. The mathematical description for the anisotropy buildup has been discussed

by Tikhomirov [73]. In his paper, Tikhomirov sites Kolhrausch's law as a basis for this equation. He goes on to suggest that the "smallest structural elements undergo a relaxation in the early stages, and this makes it possible for the relaxation of progressively larger structural elements." If we consider that these small structural elements maybe more reactive and therefore have a shorter lifetime in the altered structural state than the time between photon stimulation. We would find that the period amid the successive exponential buildups would increase causing the β value to be even smaller, (i.e. a smaller β stretches the exponential time scale even greater) as the sample thickness increases.

In previous work, Hertogen had only used one sample thickness that was substantially thicker than the absorption depth. This work was able to extend the previous data to a wide range of sample thicknesses.

7.4 Suggestions for Future Work

Studies have been conducted [21, 65] where a DC as well as an ac electric field was applied to a chalcogenide glass transverse to the inducing beam propagation. The results of these studies [21, 65] showed no detectable influence of a transverse electrical field on the level or rate of photoinduced dichroism. Interestingly, it has recently been found that the time required to induce the photodarkening effect can be accelerated with the application of a longitudinal DC electric field [75]. It would be intriguing to see if a longitudinal electric field has any effect on the photoinduced dichroism.

Fully researching the effects of applying an electric field to chalcogenide glasses can only lead to a better understanding of this unique characteristic of chalcogenide glasses.

Another area of research is in the combined influence of temperature, pump intensity and sample thicknesses on photoinduced anisotropy. The problem with the study is the time requirement. A complete measurement run for the intensities used in this report required 14 days for a 0.25 μm sample. For a 2 μm thick sample this time length would increase to about 56 days. Using 5 different thicknesses ranging from 0.25

μm to 2 μm and considering an average of 21 days for a complete measurement run. Then at any given temperature about 105 days or just over 3 months of continuous measurement time is needed. Obviously adding in the temperature variation increases this measurement time to years. Consequently this research undertaking would be suitable for a Ph. D.

From the diverse opinions that researchers have about the microscopic processes responsible for these photoinduced changes, there is much more work to be done in order to gain a full understanding of this phenomena. To the end of developing a model that can fully explain the microscopic mechanisms involved with these unique photoinduced characteristic of chalcogenide glasses.

References

[1] N.A. Goryunova and B.T. Kolomiets, Journal of Technical Physics (USSR), Vol. 25, pg. 984, 1955.

[2] http://www.xerox.com/innovation/Storyofxerography.pdf

[3] S.O. Kasap and J.A. Rowlands, "Direct-conversion Flat-panel X-ray Image Sensors for Digital Radiography", Proceedings of the IEEE, Vol. 90, pp 591 – 604, 2002.

[4] L.C. Kimerling, "Silicon Microphotonics," Applied Surface Science, Vol. 159 – 160, pp 8 – 13, 2000.

[5] R.G. DeCorby, M.M. Pai, H.T. Nguyen, P.K. Dwivedi, T.J. Clement, C.J. Haugen, J.N. McMullin and S.O. Kasap, "High Index Contrast Waveguides in Chalcogenide Glass and Polymer," IEEE Journal of Selected Topics in Quantum Electronics, Vol. 11, no. 2, pp 539 – 546, 2005.

[6] A. Mori, Y. Ohishi, T. Kanamori, and S, Sudo, "Optical Amplification With Neodymium–doped Chalcogenide Glass Fiber," Applied Physics Letter, Vol. 70, pp 1230 – 1232, 1997.

[7] N.F. Mott and E.A. Davis, "Electronic Processes in Non-crystalline Materials 2nd Edition," Oxford University Press, Copyright 1979.

[8] J.P. De Neufville, S.C. Moss and S.R. Ovshinsky, "Photostructural Transformations in Amorphous As_2Se_3 and As_2S_3 Films," Journal of Non-Crystalline Solids, Vol. 13, no. 2, pp 191 – 223, 1974.

[9] J.F. Viens, C. Meneghini, A. Villeneuve, T.V. Galstian, E.J. Knystautas, M.A. Duguay, K.A. Richardson and T. Cardinal, "Fabrication and Characterization of Integrated Optical Waveguides in Sulfide Chalcogenide Glasses," Journal of Lightwave Technology, Vol. 17, no. 7, pp 1184 – 1191, 1999.

[10] H. Hisakuni, K. Shiramine and K. Tanaka, "Photoinduced Bragg Reflector in As_2S_3 Glass," Applied Physics Letter, Vol. 64, no. 14, pp 1771 – 1773, 1994.

[11] V. Lyubin, M. Kelbanov, A. Feigel and B. Sfez, "Films of chalcogenide glassy Semiconductors: New Phenomena and New Applications," Thin Films, Vol. 459, pp 183 – 186, 2004.

[12] V.G. Zhdanov, B.T. Kolomiets, V.M. Lyubin and V.K. Malinovbskii, "Photoinduced Optical Anisotropy in Chalcogenide Vitreous Semiconducting Films," Physica Status Solidi A, Vol. 52, pp 621 – 626, 1979.

[13] D. DeForrest, R.E. Johanson and S.O. Kasap, "Photoinduced Dichroism in Thin Films of Amorphous As_2Se_3," IEEE CCECE 2005, pp 1493 – 1495, 2005.

[14] M. Asobe, H. Kobayashi, H. Itoh and T. Kanamori, "Laser-diode-driven Ultrafast All-optical Switching by Using Highly Nonlinear Chalcogenide Glass Fiber," Optics Letter, Vol. 18, pp 1056 – 1058, 1993.

[15] E.M. Vogel, M.J. Weber and D.M. Krol, "Nonlinear Optical Phenomena in Glass," Physics and Chemistry of Glasses, Vol. 32, no. 6, pp 231 – 254, 1991.

[16] A.V. Kolobov, "Photo-Induced Metastability in Amorphous Semiconductors" Wiley-VCH GmbH & Co. KGaA, Weinheim, Copyright 2003.

[17] V. Lyubin, M. Klebanov and V.K. Tikhomirov, "Photoinduced Anisotropy of Photoconductivity in Amorphous $As_{50}Se_{50}$ Films," Physical Review Letters, Vol. 87, no. 21, pp 216806-1 – 216806-3, 2001.

[18] P. Krecmer, A.M. Moulin, R.J. Stephenson, T. Rayment, M.E. Welland and S.R. Elliott, "Reversible Nanocontraction and Dilatation in a Solid Induced by Polarized Light," Science, Vol. 277, pp 1799 – 1802, 1997.

[19] S.O. Kasap, Optoelectronics chapter in "The Encyclopedia of Optics" Wiley-VCH, 2003.

[20] S. Ramachandran and S.G. Bishop, "Low Loss Photoinduced Waveguides on Rapid Thermally Annealed Films of Chalcogenide Glasses," Applied Physics Letter, Vol. 74, no. 1, pp 13 – 15, 1999.

[21] P. Hertogen, "Photoinduced Anisotropies in Chalcogenide Semiconductors," Ph. D. Thesis, Katholieke Universiteit Leuven, Copyright 2000.

[22] K. Tanaka, E. Maruyama, T. Shimada and H. Okamoto, "Amorphous Silicon," John Wily & Sons Ltd. Copyright 1999.

[23] A. Madan and M.P. Shaw, "The Physics and Applications of Amorphous Semiconductors," Academic Press, Inc. Copyright 1988.

[24] N.F. Mott, "Electrons in Disordered Structures," Advances in Physics, Vol. 16, pp 49 – 145, 1967.

[25] R. Zallen, "The Physics of Amorphous Solids," Wiley-Interscience Publication, John Wiley & Sons Copyright 1983.

[26] W.H. Zachariasen, "The Atomic Arrangement in Glass," Journal of the American Chemistry Society, Vol. 54, pp 3841 − 3851, 1932.

[27] S.O. Kasap, "Principles of Electronic Materials and Devices, 2nd Edition," McGraw-Hill, Copyright 2002.

[28] P.W. Anderson, "Absence of Diffusion in Certain Random Lattices," Physical Review, Vol. 109, pp 1492 – 1505, 1958.

[29] M.H Cohen, H. Fritzsche and S.R. Ovshinski, "Simple Band Model for Amorphous Semiconductor Alloys", Physical Review Letters, Vol. 22, no. 20, pp 1065 – 1068, 1969.

[30] J.M. Marshall and A.E. Owen, "Drift Mobility Studies in Vitreous Arsenic Triselenide," Philosophical Magazine, Vol. 24, pp 1281 – 1290, 1971.

[31] J. Tauc, "Amorphous and Liquid Semiconductors," Plenum Press, Copyright 1974.

[32] N.F. Mott, "Conduction in Non-crystalline Materials III. Localized States in a Pseudogap and Near Extremities of Conduction and Valence Bands," Philosophical Magazine, Vol.19, Series 5, pp 835 – 852, 1969.

[33] Z.U. Borisova, "Glassy Semiconductors," Plenum Press, Copyright 1981.

[34] M. Kastner, "Bonding Bands, Lone-Pair Bands, and Impurity States in Chalcogenide Semiconductors," Physical Review Letters, Vol. 28, no. 6, pp 355 – 357, 1972.

[35] P.W. Anderson, "Model for the Electronic Structure of Amorphous Semiconductors," Physical Review Letters, Vol. 34, no. 15, pp 953 – 955, 1975.

[36] R.A. Street and N.F Mott, "States in the Gap in Glassy Semiconductors," Physical Review Letters, Vol. 35, no. 19, pp 1293 – 1295, 1975.

[37] S.R. Elliott, "Physics of Amorphous Materials," Longman Scientific & Technical, Copublished in the US with John Wiley & Sons, Copyright 1983.

[38] M. Kastner, D. Adler and H. Fritzsche, "Valence-Alternation Model for Localized Gap States in Lone-Pair Semiconductors," Physical Review Letters, Vol. 37, no. 22, pp 1504 – 1507, 1976.

[39] A.V. Kolobov, M. Kondo, H. Oyanagi, R. Durny, A. Matsuda and K. Tanaka, "Experimental Evidence For Negative Correlation Energy and Valence Alternation in Amorphous Selenium," Physical Review B, Vol. 56, no. 2, pp R485 – R488, 1997.

[40] K. Shimakawa, A. Kolobov and S.R. Elliott, "Photoinduced Effects and Metastability in Amorphous Semiconductors and Insulators," Advances in Physics, Vol. 44, no. 6, pp 475 – 588, 1995.

[41] C.Y. Yang, M.A. Paesler and D.E. Sayers, "Measurement of Local Structural Configurations Associated with Reversible Photostructural Changes in Arsenic Trisulfide Films," Physical Review B, Vol. 36, pp 9160 – 9167, 1987.

[42] V. M. Lyubin and V. K. Tikhomirov, "Photodarkening and Photoinduced Anisotropy in Chalcogenide Vitreous Semiconductor Films," Journal of Non-Crystalline Solids, Vol. 114, pp 133 − 135, 1989.

[43] V.K. Tikhomirov and S.R. Elliot, "Model for Photoinduced Anisotropy and Its Dark Relaxation in Chalcogenide Glasses," Physical Review B, Vol. 51, no. 8, pp 5539 – 5541, 1995.

[44] V.M. Lyubin and V.K. Tikhomirov, "Spectra of Natural and Photoinduced Linear Dichroism in Chalcogenide Glasses," Journal of Non-Crystalline Solids, Vol. 171, pp 87 – 93, 1994.

[45] K. Kimura, K. Murayama and T. Ninomiya, "Change in Optical Anisotropy of Localized States Associated with Reversible Photostructural Change in a-As_2S_3 Films," Journal of Non-Crystalline Solids, Vol. 77 & 78, pp 1203 – 1206, 1985.

[46] J.S. Berkes, S.W. Ing, Jr. and W. J. Hillegas, "Photodecomposition of Amorphous As_2Se_3 and As_2S_3," Journal of Applied Physics, Vol. 42, no. 12, pp 4908 – 4916, 1971.

[47] R.A. Street, J. Kakalios, C.C. Tsai and T.M. Hayes, "Thermal-equilibrium Processes in Amorphous Silicon," Physical Review B, Vol. 35, pp 1316 – 1333, 1987.

[48] K. Tanaka, "Mechanisms of Photodarkening in Amorphous Chalcogenides," Journal of Non-Crystalline Solids, Vol. 59 & 60, pp 925 – 928, 1983.

[49] A.V. Kolobov, Yu.P. Kostikov, S.S.Lantratova, and V.M. Lyubin, "Photoelectron Spectroscopic Investigation of Photostructural Transformations in Glassy Chalcogenide Semiconductor Films," Soviet Physics - Solid State, Vol. 33, no. 3, pp 444 – 447, 1991.

[50] S.O. Kasap, "Optoelectronics and Photonics Principles and Practices," Prentice-Hall, Copyright 2001.

[51] T. Kósa and I. Jánossy, "Kinetics of Optical Reorientation in Amorphous $GeSe_2$ Films," Philosophical Magazine B, Vol. 64, no. 3, pp 355 – 366, 1991.

[52] V.M. Lyubin and V.K. Tikhomirov, "Photoinduced Gyrotropy and Photoinduced Light Scattering in the Chalcogenide Glass As_2S_3," JETP Letters, Vol. 52, no. 2, pp 78 – 81, 1990.

[53] H. Fritzsche, "The Origin of Reversible and Irreversible Photostructural Changes in Chalcogenide Glasses," Philosophical Magazine B, Vol. 68, no. 4, pp 561 – 572, 1993.

[54] V.K. Tikhomirov and S.R. Elliott, "Metastable Optical Anisotropy in Chalcogenide Glasses Induced by Unpolarized Light," Physical Review B, Vol. 49, no. 24, pp 17476 – 17479, 1994.

[55] V.M. Lyubin and V.K. Tikhomirov, "Photoinduced Dichroism in Glassy Chalcogenide Semiconductor Films," Soviet Physics Solid State, Vol. 32, no. 6, pp 1069 – 1074, 1990.

[56] S.R. Elliott and V.K. Tikhomirov, "Vectoral and Scalar Photoinduced Effects in Chalcogenide Glasses," Journal of Non-Crystalline Solids, Vol. 198 – 200, pp 669 − 674, 1996.

[57] V. K. Tikhomirov, G. J. Adriaenssens and S. R. Elliott, "Temperature Dependence of the Photoinduced Anisotropy in Chalcogenide Glasses: Activation Energies and Their Interpretation," Physical Review B, Vol. 55, no. 2, pp R660 − R663, 1997.

[58] H. Fritzsche, "The Origin of Photo-Induced Optical Anisotropies in Chalcogenide Glasses," Journal of Non-Crystalline Solids, Vol. 164 – 166, pp 1169 – 1172, 1993.

[59] H. Fritzsche, "Optical Anisotropies in Chalcogenide Glasses Induced by Band-Gap Light," Physical Review B, Vol. 52, no. 22, pp 15845 – 15861, 1995.

[60] Reza Tanha, "Electron and Hole Transport in Stabilized a-Se for X-Ray Imaging," Master of Science Thesis University of Saskatchewan, 1998.

[61] A.C. van Popta, R.G. DeCorby, C.J. Haugen, T. Robinson, J.N. McMullin, D. Tonchev, and S.O. Kasap, "Photoinduced Refractive Index Change in As_2Se_3 by 633nm Illumination," Optics Express, Vol. 10, no. 15, pp. 639 – 644, 2002.

[62] Eugene Hecht, "Optics Second Edition," Addison Wesley Publishing Company, Copyright 1990

[63] V. V. Poborchii, A. V. Kolobov and K. Tanaka, "Photomelting of Selenium at Low Temperature," Applied Physics Letters, Vol. 74, no. 2, pp 215 – 217, 1999.

[64] P. Hertogen, V.K. Tikhomirov and G.J. Adriaenssens, "Photoinduced Dichroism in Chalcogenides: Influence of Temperature and Light Intensity," Journal of Non-Crystalline Solids, Vol. 256 & 257, pp 343 – 347, 1999.

[65] P. Hertogen and G.J. Adriaenssens, "Influence of Temperature, Light Intensity and Electrical Field on the Photoinduced Dichroism in Chalcogenide Thin Films," Journal of Non-Crystalline Solids, Vol. 266 – 269, pp 948 – 953, 2000.

[66] R. Swanepoel, "Determination of the Thickness and Optical Constants of Amorphous Silicon," Journal of Physics E, Vol. 16, no.12, pp. 1214 – 1222, 1983.

[67] G. J. Adriaenssens, V. K. Tikhomirov, and S. R. Elliott, "Mechanism and Kinetics of Photoinduced Anisotropy in Chalcogenide Glasses," Journal of Non-Crystalline Solids, Vol. 227 – 230, pp 688 – 693, 1998.

[68] D.F. Phipps, "The Logistic Curve: A Fitting Technique," The Statistician, Vol. 24, no. 2, pp 129 – 136, 1975.

[69] V. M. Lyubin, V. K. Tikhomirov and V. I. Zemel'ko, "Natural and Photoinduced Optical Activity of Chalcogenide Glasses," Soviet Journal of Glass Physics and Chemistry, Vol. 17, no. 6, pp 563 – 568, 1991.

[70] V. M. Lyubin and V. K. Tikhomirov, "Photoinduced Anisotropy and Gyrotropy in Bulk Chalcogenide Glasses Under Sub-band Excitation," Revue Roumaine de Physique, Vol. 36, no.10, pp 725 – 734, 1991.

[71] V. Mikla, V. Fedelesh, V. Stefanovich, and V. Slivka, "Influence of Preparation Conditions on Photo- and Thermo-Structural Changes of As_xS_{1-x} Films," Materials Science & Engineering B, Vol. B38, no. 1 – 2, pp 122 – 126, 1996.

[72] V. Lyubin and M. Kelbanov, "Photoinduced Generation and Reorientation of Linear Dichroism in As Se Glassy Films," Physical Review B, Vol. 53, no. 18, pp R11924 – R11926, 1996.

[73] V. K. Tikhomirov, "Relaxation of a Photoinduced Anisotropy in Chalcogenide Glasses," JETP Letter, Vol. 57, no.12, pp 821 – 825, 1993.

[74] J. Hajtó, I. Jánossy and G. Forgás, "Laser-induced Optical Anisotropy in Self-supporting Amorphous $GeSe_2$ Films," Journal of Physics C: Solid State Physics, Vol. 15, pp 6293 – 6303, 1982.

[75] K. Shimakawa, T. Kato, T. Hamagishi, "Acceleration of Photodarkening Under DC Electric Field in Amorphous As_2Se_3 Films," Journal of Non-Crystalline Solids, Vol. 338 – 230, pp 548 – 551, 2004.

Appendix A

MatLab Programs

Solve_Anisotropy.m

```
%*********************************************************************%
% File Name: Solve_Anisotropy.m                                       %
% Date: January 29, 2005                                              %
%                                                                     %
% Program Description:                                                %
%        This program takes the RMS readings that the Lock-In Amp     %
% measures and converts them to a peak voltage. It then iteratively   %
% determines the intermediate absorption values                       %
% Delta (0.5*[exp(-2*Alpha(x)L) - exp(-2*Alpha(y)L)] and              %
% Sigma (0.5*[exp(-2*Alpha(x)L) + exp(-2*Alpha(y)L)].                 %
% Then the amount of anisotropy is calculated.                        %
%*********************************************************************%

    % Clear workspace of all previous data values.
    clear all;

    % Constants derived from just the probe beam through a fresh spot
      on sample.
    % i.e. Has not been photodarkened (or with Ge in sample
      photobleached).
    Chi = 22.41105037*pi/180;
    fp = 8.082861878e-3;
    Io = 3.276604338;
    Sigma_1 = 1;
    % While Loop count variable.
    Count_w = 0;

% Load Files
% load filename.ext reads ASCII files that contain rows of space-
  separated values.
% The resulting data is placed into a variable with the same name as
  the file (without the extension).
% The text file must be organized as a rectangular table of numbers,
% separated by blanks, with one row per line, and an equal number of
  elements in each row.
% An error occurs if the number of values differs between any two rows.

% S = load(...) returns the contents of a MAT-file in the variable S
% When the file contains ASCII data, S is a double-precision array.
```

```
    % Load data file.
    data = load('E:\Chalcogenide\Experiment Results\Testing\As2Se3 Run
                212\Analysis Center\Anisotropy\05_03_03.txt','-ascii');

% Open Files
% FID = FOPEN(FILENAME,PERMISSION) opens the file FILENAME in the mode
       specified by PERMISSION.
% PERMISSION  - r = read only.
%             - w = write (create if necessary)

    % Open results file for writing the results.
    results = fopen('E:\Chalcogenide\Experiment Results\Testing\As2Se3
     Run 212\Analysis Center\Anisotropy\1_0 Results_05_03_03.csv','w');

    % Print Header for results file.
    fprintf(results,'%s \r','R, Theta, DC, Eta, Delta, Sigma,
            Anisotropy');

    % Zeros matrix to store results for graphing points.
    g = zeros(length(data), 1);
    h = zeros(length(data), 1);

        % First point solution.

            r = data(1,1)*(2)^(1/2); % Want Peak Value. Lock-In Amp
                measures RMS.
            I = data(1,3);

        % Solve delta for first sample point.
            Sigma_1 = I/Io; % Sample is Photodarkened (if Ge then
       Photobleached). This initiates Sigma closer to proper level.
            a = 1;
            b = 2*Sigma_1*fp*cos(Chi);
            c = (Sigma_1*fp)^2-(r/Io)^2;
            Delta = (-b+(b^2-4*a*c)^(1/2))/(2*a);

        % Check value of Sigma_1

            Sigma = I/Io - 0.5*fp*Delta*cos(Chi);
            Check_a = abs(Sigma_1 - Sigma);

       % Reduce error of calculation.

        while Check_a > 1e-20   % Want less than 1e-20 change in Sigma
                                  from one calculation to next.

            % Count loops.
            Count_w = Count_w + 1;

            Sigma_1 = Sigma;
            a = 1;
            b = 2*Sigma*fp*cos(Chi);
            c = (Sigma*fp)^2-(r/Io)^2;

            % Calculate new Delta.
            Delta = (-b+(b^2-4*a*c)^(1/2))/(2*a);
```

```
            % Check value of Sigma
            Sigma = I/Io - 0.5*fp*Delta*cos(Chi);
            Check_a = abs(Sigma_1 - Sigma);

        end


% Solve for all points using the previous Sigma value as initial
  guess value.
    for i = 1:length(data)

            % Get data for evaluation.
            r = data(i,1)*(2)^(1/2); % Want Peak Value. Lock-In Amp
                                       measures RMS.
            I = data(i,3);

        % Initialization of while loop.
        Check_a = 1;

        while Check_a > 1e-20   % Want less than 1e-20 change in Sigma
                                  from one calculation to next.

            % Count loops.
            Count_w = Count_w + 1;  % Can be used if interested how
                                      many calculation loops had to be
                                      performed per Delta value.

            Sigma_1 = Sigma;
            a = 1;
            b = 2*Sigma*fp*cos(Chi);
            c = (Sigma*fp)^2-(r/Io)^2;

            % Calculate new Delta.
            Delta = (-b+(b^2-4*a*c)^(1/2))/(2*a);

            % Check value of Sigma
            Sigma = I/Io - 0.5*fp*Delta*cos(Chi);
            Check_a = abs(Sigma_1 - Sigma);

        end

        % Calculate Eta (Check). Can be used as a comparison to Lock-In
          Amp measured Theta value.
        Eta = (atan((-fp*Sigma*sin(Chi))/(Delta +
               fp*Sigma*cos(Chi))))*180/pi;

        % Calculate anisotropy. Anisotropy = [Alpha(x) - Alpha(y)]*L.
        ani = (-log((Sigma - Delta)/(Sigma + Delta)))/2;

        fprintf(results,'%+14.9E %s %+14.9E %s %+14.9E %s %+14.9E %s
                %+14.9E %s %+14.9E %s %+14.9E \r',data(i,1),', ',
                data(i,2),', ',data(i,3),', ',Eta,', ',Delta,', ',
                Sigma,', ',ani);

        % Put results into the matrix for plotting.
        g(i,1) = ani;
        h(i,1) = -ani;
```

```
        t(i,1) = i;

    end

    % Plot Results.
    % See LineSpec for color, line and marker specifiers.
    figure(1);
    plot (t, h, 'r-'), axis ([0 length(data)+50 -0.0015 -0.0003]), grid
    title('Anisotropy Results.');
    xlabel('Time Axis (Each point equates to 5 seconds).');
    ylabel('A = 2*(Ix - Iy)/(Ix + Iy)');

    figure(2);
    plot (t, g, 'r-'), axis ([0 length(data)+50 0.0003 0.0015]), grid
    title('Anisotropy Results.');
    xlabel('Time Axis (Each point equates to 5 seconds).');
    ylabel('A = 2*(Ix - Iy)/(Ix + Iy)');

    % Close all files.
    fclose all;

% *END PROGRAM*
```

Fit_Curve.m

```
%*********************************************************************%
% File Name: Fit_Curve.m                                              %
% Date: March 12, 2005                                                %
%                                                                     %
% Program Description:                                                %
%       Used to fit anisotropy data using the least-squares           %
% minimization function to the theoretical stretched exponential      %
% function, which is commonly used for this phenomenon.               %
%*********************************************************************%

    % Clear workspace of all previous data values.
    clear all;

    % Load the data file for reading.
    data = load('D:\Chalcogenide\Experiment Results\Testing\As2Se3 Run
                212\Analysis Center\Curve Fitting\Seconds\H3s.txt',
               '-ascii');

    % Open the results file for writing the results.
    results = fopen('D:\Chalcogenide\Experiment Results\Testing\As2Se3
                    Run 212\Analysis Center\Curve Fitting\Seconds\
                    Curve_Fitting_Results_H3.csv','w');

    % Data to be fitted.
    x = data(:,1);      % Time Data.
    y = data(:,2);      % Anisotropy Data.
    init = data(1,2);   % Initial start value of stretched exponential
                          growth of anisotropy.

    % Stretched Exponential Equation with initial start value.
    TimeC = fittype('a0 + (init - a0)*(exp(-(x/a1)^a2))');
    % Assign opts as the fitoptions for TimeC (Time Constant).
    opts = fitoptions(TimeC);
    % Assign Guess Values, Lower and Upper Limits.
     set(opts,'normalize','off','start',[0.0014044673 383.869805
     0.554568846],'lower',[-1 0 -1],'upper',[1 1500 2]);
    [fit_parameters, error_fn_gof] = fit(x,y,TimeC,opts);
    fit_parameters.a0 % Display Solved Fit Parameters on Workspace.
    fit_parameters.a1
    fit_parameters.a2

    % Store Fit Parameters.
    Saturation = fit_parameters.a0;
    tau = fit_parameters.a1;
    Gamma = fit_parameters.a2;

    % Print Stretched Exponential Fitted Parameter Results to file.
    fprintf(results,'%s \r','Saturated Level,Time Constant,Stretched
    Exponent');
    fprintf(results,'%+14.9E %s %+14.9E %s %+14.9E \r',
            fit_parameters.a0,',',fit_parameters.a1,',',
            fit_parameters.a2);
```

```
% Determine Fitted Data using the derived Stretched Exponential fit
  parameters.
% Zeros matrix to store results of points using the stretched
  exponential fitted parameters.
yfit = zeros(length(data), 1);
for i = 1:length(data)  % For loop length is the length of the data
                          file.

    % Calculate fitted data using the derived Stretched Exponential
      fit parameters.
    yfit(i) = fit_parameters.a0 + (init - fit_parameters.a0)*(exp(-
              (x(i)/fit_parameters.a1)^fit_parameters.a2));

end

TimexpC = fittype('b0 + (init - b0)*(exp(-(x/b1)))'); % Straight
          Exponential Equation with initial start value.
opts = fitoptions(TimexpC); % Assign opts as the fitoptions for
       TimexpC (Time Constant).
set(opts,'normalize','off','start',[0.0013690665 406.35],'lower',
[-1 0],'upper',[1 1500]); % Assign Guess Values, Lower and Upper
Limits.
[fit_parameters, error_fn_gof] = fit(x,y,TimexpC,opts);
[fit_parameters, error_fn_gof] = fit(x,y,TimexpC,opts);
fit_parameters.b0 % Display Solved Fit Parameters on Workspace.
fit_parameters.b1

% Print Exponential Fitted Parameter Results to file.
fprintf(results,'%s \r','Saturated Level,Time Constant');
fprintf(results,'%+14.9E %s %+14.9E \r',fit_parameters.b0,',',
        fit_parameters.b1);

% Print Header for results file.
fprintf(results,'%s \r','Time in Seconds, Measured Data, Stretched
        Fit, Exponential Fit');

% Determine Fitted Data using the derived Exponential fitted
  parameters.
yexpfit = zeros(length(data), 1); % Zeros matrix to store results
of points using the straight exponential fitted parameters.

for i = 1:length(data)  % For loop length is the length of the data
file.

    % Calculate fitted data using the derived fit parameters.
    yexpfit(i) = fit_parameters.b0 + (init - fit_parameters.b0)
                 *(exp(-(x(i)/fit_parameters.b1)));

    % Print Stretched Exponential and Exponential fit results to
      file.
    fprintf(results,'%+14.9E %s %+14.9E %s %+14.9E %s %+14.9E
             \r',x(i),',',y(i),',',yfit(i),',',yexpfit(i));

end
```

```
% Set Figure Number.
figure(1);

% Plot Results.
% See LineSpec for color, line and marker specifiers.

% Plot Original Data.
plot (x, y, 'r-'), grid  % Red circle marker.

% Hold Figure 1 to plot curve using the Time Constant Fitted
  Parameters.
hold

% Plot Curve using the Stretched Exponential Fitted Parameters.
plot (x, yfit, 'k-')    % Black Line.

% Label Figure.
title('Time Constant Stretched Exponential Curve Fitting
       Results.');
xlabel('Time Axis (Seconds)');
ylabel('A = 2*(Ix - Iy)/(Ix + Iy)');
legend('Data','Stretched Exponential Fit',4);

% Remove hold on plot.
hold


xfit = zeros(length(data), 1); % Zeros matrix to store results.
t = zeros(length(data), 1); % Zeros matrix to store Gamma compressed
    time results.

for i = 1:length(data)  % For loop length is the length of the data
                          file.

    t(i) = x(i)^Gamma;

    xfit(i) = log((y(i) - Saturation)/(init - Saturation));

end

figure(2);
% Plot Curve using the Time Constant Fitted Parameters.
plot (t, xfit, 'k-'), grid    % Black Line.

% Label Figure.
title('Parameter Fit Plot.');
xlabel('Compressed Time Axis (t^G^a^m^m^a)');
ylabel('ln((A - A_s_a_t)/(A_i - A_s_a_t))');

% Set Figure Number.
figure(3);

% Plot Results.
% See LineSpec for color, line and marker specifiers.

% Plot Original Data.
plot (x, y, 'r-'), grid  % Red circle marker.
```

```
    % Hold Figure 3 to plot curve using the Time Constant Fitted
      Parameters.
    hold

    % Plot Curve using the Stretched Exponential Fitted Parameters.
    plot (x, yfit, 'k-')    % Black Line.

    % Plot Curve using the Straight Exponential Fitted Parameters.
    plot (x, yexpfit, 'b-')    % Blue Line.

    % Label Figure.
    title('Time Constant Curve Fitting Results.');
    xlabel('Time Axis (Seconds)');
    ylabel('A = 2*(Ix - Iy)/(Ix + Iy)');
    legend('Data','Stretched Exponential Fit','Exponential Fit',4);

    % Remove hold on plot.
    hold

    % Close all files.
    fclose all;

% *END PROGRAM*
```

Gaussian_Fit.m

```
%*********************************************************************%
% File Name: Gaussian_Fit.m                                           %
% Date: April 18, 2005                                                %
%                                                                     %
% Program Description:                                                %
%       Used to fit a beam profile data to a Gaussian curve using the%
% least-squares minimization function.                                %
%*********************************************************************%

    % Clear workspace of all previous data values.
    clear all;

    % Load the data file for reading.
    data = load('D:\Chalcogenide\Experiment Information\Math Analysis
                  \Beam Profile\MatLab\HP_H_Profile_05_13_04.txt','
                  -ascii');

    % Open the results file for writing the results.
    results = fopen('D:\Chalcogenide\Experiment Information\Math
                    Analysis\Beam Profile\MatLab
                    \Test_Profile.csv','w');

    % Data to be fitted.
    x = data(:,1);      % Position Data.
    y = data(:,2);      % Measured Voltage Data.

    % Gaussian Equation.
    Profile = fittype('a0*(exp(-(((x-a1)^2)/(2*(a2^2)))))');
    opts = fitoptions(Profile); % Assign opts as the fitoptions for
           Profile (Beam Profile Constant).
    % Assign Guess Values, Lower and Upper Limits.
    set(opts,'normalize','off','start',[2.08490131 -0.01391836351
        0.5108894708],'lower',[0 -1 0],'upper',[4 1 2]);
    [fit_parameters, error_fn_gof] = fit(x,y,Profile,opts);
    fit_parameters.a0 % Display Solved Fit Parameters on Workspace.
    fit_parameters.a1
    fit_parameters.a2

    % Store Fit Parameters.
    Peak = fit_parameters.a0;
    Offset = fit_parameters.a1;
    Sigma = fit_parameters.a2;

    % Print Gaussian Fit Parameter Results to file.
    fprintf(results,'%s \r','Peak Level,Axis Offset,Sigma');
    fprintf(results,'%+14.9E %s %+14.9E %s %+14.9E  \r',
            fit_parameters.a0,',',fit_parameters.a1,',',
            fit_parameters.a2);

    % Determine Fitted Data using the derived Gaussian curve fit
      parameters.
    yfit = zeros(length(data), 1); % Zeros matrix to store results of
           points using the Gaussian curve fit parameters.
```

```
    % Print Header for results file.
    fprintf(results,'%s \r','Position, Measured Data, Gaussian Fit');

    for i = 1:length(data)  % For loop length is the length of the data
                              file.

        % Calculate fitted data using the derived Gaussian curve fit
          parameters.
        yfit(i) = fit_parameters.a0*(exp(-(((x(i)-fit_parameters.a1)^2)
                  /(2*(fit_parameters.a2)^2))));

        % Print Gaussian fit results to file.
        fprintf(results,'%+14.9E %s %+14.9E %s %+14.9E  \r',x(i),',',
                y(i),',',yfit(i));

    end


    % Set Figure Number.
    figure(1);

    % Plot Results.
    % See LineSpec for color, line and marker specifiers.

    % Plot Original Data.
     plot (x, y, 'r-','linewidth',2)  % Red line.

    % Hold Figure 1 to plot curve using the Gaussian Fit Parameters.
    hold

    % Plot Curve using the Gaussian Fit Parameters.
    plot (x, yfit, 'b:','linewidth',2)    % Blue Dotted Line.

    % Label Figure.
    title('Beam Profile using a Gaussian Curve Fit.');
    xlabel('Position in millimeters');
    ylabel('Beam Intensity Level in Voltage');
    legend('Data','Gaussian Fit',2);

    % Remove hold on plot.
    hold

    % Close all files.
    fclose all;

% *END PROGRAM*
```